12-2012

Assessment of Fidelity to Data and Robustness to Uncertainty to Assure Credible Predictions in the Modeling of Wind Turbine Blades

Kendra Van buren
Clemson University, klvan@clemson.edu

ASSESSMENT OF FIDELITY TO DATA AND ROBUSTNESS TO UNCERTAINTY TO ASSURE CREDIBLE PREDICTIONS IN THE MODELING OF WIND TURBINE BLADES

A Dissertation
Presented to
the Graduate School of
Clemson University

In Partial Fulfillment
of the Requirements for the Degree
Doctor of Philosophy
Civil Engineering

---

by
Kendra L. Van Buren
December 2012

Accepted by:
Dr. Sezer Atamturktur, Committee Chair
Dr. Hsein Juang
Dr. Abdul Khan
Dr. Nadarajah Ravichandran
Dr. John Wagner

ABSTRACT

In the field of wind energy, modeling and simulation techniques provide an efficient and economical alternative to experimentation for studying the behavior of wind turbines. Numerical models however are approximations of reality, thusly making it crucial to evaluate various sources of uncertainties that influence the model predictions. Credibility of a numerical model rests on the model's ability to replicate existing experimental data, widely known as fidelity-to-data. This dissertation advocates that fidelity-to-data, while necessary, is insufficient to claim credibility of a numerical model. Herein, the objective is to develop numerical models that not only provide agreement to experimental data, but also remain consistent (robust) as *unavoidable* uncertainties are considered.

The focus in this dissertation is on the development of models that are simplified yet consistent with experiments, which offer the possibility of large scale simulations for rapid prototyping and prognostics. This dissertation presents a completely integrated Verification and Validation (V&V) procedure that includes the solution and code verification, sensitivity analysis, calibration, validation, and uncertainty quantification in the development of a finite element (FE) model of the CX-100 wind turbine blade that is simplified yet consistent with experiments. This integrated V&V procedure implements a comprehensive evaluation of uncertainties, including experimental, numerical, and parametric uncertainties, to evaluate the effect of assumptions encountered in the model development process. Mesh refinement studies are performed to ensure that mesh size is chosen such that the effect of numerical uncertainty does not exceed experimental uncertainty. A main effect screening is performed to determine and eliminate the model parameters that are least sensitive to model output, reducing demands on computational resources to only calibrate parameters that significantly influence model predictions. Model calibration is performed in a two-step procedure to de-couple boundary condition effects from the

material properties: first against the natural frequencies of the free-free experimental data, and second against the natural frequencies of the fixed-free experimental data. The predictive capability of the calibrated model is successfully validated by comparing model predictions against an independent dataset. Through the V&V activities, this dissertation demonstrates the development of a FE model that is simplified yet consistent with experiments to simulate the low-order vibrations of wind turbine blades.

Confidence in model predictions increases when the model has been validated against experimental evidence. However, numerical models that provide excellent fidelity to data after calibration and validation exercises may run the risk of generalizing poorly to other, non-tested settings. Such issues with generalization typically occur if the model is overly complex with many uncertain calibration parameters. As a result, small perturbations in the calibrated input parameter values may result in significant variability in model predictions. Therefore, this dissertation posits that credible model predictions should simultaneously provide fidelity-to-data and robustness-to-uncertainty. This concept that relies on the trade-off between fidelity and robustness is demonstrated in the selection of a model from among a suite of models developed with varying complexity for CX-100 wind turbine blade in a configuration with added masses. The robustness to uncertainty is evaluated through info-gap decision theory (IGDT), while the fidelity to data is determined with respect to the experimentally obtained natural frequencies of the CX-100 blade.

Finally, as fidelity and robustness are conflicting objectives, model calibration can result in multiple plausible solutions with comparable fidelity to data and robustness to uncertainty, raising concerns about non-uniqueness. This dissertation states that to mitigate such non-uniqueness concerns, self-consistency of model predictions must also be evaluated. This concept is demonstrated in the development of a one dimensional simplified beam model to replace the

three dimensional finite element model of CX-100 wind turbine blade. The findings demonstrate that all three objectives, fidelity-to-data, robustness-to-uncertainty and self-consistency are conflicting objectives and thus, must be considered simultaneously. When all three objectives are considered during calibration it is observed that the fidelity optimal model remains both least robust and self-consistent, suggesting that robustness and self-consistency are necessary attributes to consider during model calibration.

ACKNOWLEDGEMENTS

I would like to thank my committee chair, Dr. Atamturktur, for her guidance during my graduate education. I would also like to thank Dr. Juang, Dr. Khan, Dr. Ravichandran, and Dr. Wagner for their input as my committee members. Furthermore, much of the work presented in this dissertation is in conjunction with the Laboratory Directed Research and Development project "Intelligent Wind Turbines," (IWT) conducted at Los Alamos National Laboratory (LANL). I am grateful to Curtt Ammerman, project leader of the IWT project for his support, and Francois Hemez and D.J. Luscher for their mentorship. I am also grateful to Mark Mollineaux, Ph.D student at Stanford University, for his collaboration while at LANL.

TABLE OF CONTENTS

Page

Table of Contents (Continued)

Page

Table of Contents (Continued)

Page

LIST OF TABLES

Page

LIST OF FIGURES

Page

List of Figures (continued)

Page

List of Figures (continued)

Page

CHAPTER ONE

INTRODUCTION

1.1 Motivation

In the United States, wind energy has been considered as a potential source to supply 20% of power needs by the year 2030 (U.S. Department of Energy 2008). Wind plants, and consequently wind turbines, are being produced at a larger scale to capture and produce more energy to meet the growing demands of the wind energy industry (Veers et al. 2003). To efficiently design for next generation turbines, it is crucial to understand the dynamics of wind turbine blades, which capture all of the energy produced from wind turbines. The blades are responsible for only 10-15% of the cost of the wind turbine system (Veers et al. 2003), however, damage to the blades can result in rotor instability that can lead to damage of the entire wind turbine (Ciang, Lee, and Bang 2008; Liu, Tang, and Jiang 2010). Costs associated with operation and maintenance, which are perhaps the most cost prohibitive for wind energy to be a viable energy source in the United States (Larsen and Sørensen 2003), can be remedied with condition-based blade maintenance schemes (Adams et al. 2011). Such maintenance schemes are only possible through a better understanding of wind turbine blade dynamics and such understanding can be gained through advanced modeling and simulation (M&S) techniques that incorporate realistic loading conditions in the plant scale.

M&S has gained acceptance as an economical approach to study the design of next generation of wind turbines, as demonstrated by their inclusion in wind turbine design standards. The wind energy industry can benefit from M&S as an efficient means to evaluate the structural design of wind turbine blades due to the increasing costs of full-scale testing as blades are produced at larger scales (Veers et al. 2003; Overgaard, Lund, and Thomsen 2010). Experimental

evidence is important to evaluate the ability of numerical models to replicate reality; however, such techniques are limited to idealized loading scenarios that can be implemented in laboratory conditions (Freebury and Musial 2000). Numerical models that have undergone rigorous calibration and validation exercises are useful for studying the complex loading scenarios that arise during in-service conditions of wind turbines (Jensen et al. 2006). To enhance our understanding of operational blade dynamics, future studies in M&S will need to account for complex wind turbine loading due to varying inflow conditions by coupling the finite element structural response of wind turbines with computational fluid dynamics models of the surrounding airflow (Hansen et al. 2006). Although high fidelity, three-dimensional models of wind turbine blades are pursued in the established literature, available computing resources prevents the implementation of high fidelity finite element (FE) models to be coupled with computational fluid dynamics (CFD) models for studying the behavior of wind blades at a wind plant scale. These limitations of computational capabilities necessitate the development of *simplified yet credible* FE models.

1.2 Overview of Dissertation

The objective herein is to develop a simplified model for the CX-100 wind turbine blade to simulate the low order vibration dynamics with sufficient credibility. Earlier studies emphasize the use of experimental data to assess the credibility of numerical models of wind turbine blades through test analysis correlation exercises. This dissertation, however, goes beyond mere test-analysis correlation and instead advocates an integrated verification and validation (V&V) scheme.

Herein, a FE model of the CX-100 wind turbine blade is developed beginning with code and solution verification activities to demonstrate that the code behaves as expected with

predictions within the regime of asymptotic convergence, with the predictive capability of the model confirmed through the application of calibration and validation exercises. By providing the complete story of the V&V exercises used to develop the FE model, it is ensured that the model is behaving as expected to provide accurate predictions.

Although it is important to demonstrate fidelity of model predictions to data, robustness-to-uncertainty is also a desirable (yet antagonistic) attribute of any family of models (Hemez and Ben-Haim 2011). Model input parameters (also known as knobs) are often *imprecise* resulting in uncertainties in model predictions. Furthermore, the fundamental inability to accurately reproduce truth even with the precise input parameters is due to the *inexactness* of the physics model resulting in bias in model predictions. *Robustness to model imprecision and inexactness*, henceforth referred to as *robustness-to-uncertainty*, is described as the *immunity* of the model to exceed a critical performance level even in the presence of uncertainty in the input parameters or model form. Herein, robustness to uncertainty is evaluated in the context of info-gap decision theory (IGDT). The departure of IGDT from conventional probability theory is useful for decision making under severe uncertainty, where sufficient data may not be available to defensibly formulate prior distributions. IGDT has been presented as a convenient alternative to methodologies that employ probability theory since *a priori* assumptions are not needed to describe uncertainties.

The problem of *over-fitting of numerical models to data* demonstrates the conflicting attributes of fidelity to data and robustness to uncertainty. Over-fitting typically occurs in overly-complex models that can produce accurate predictions for configurations to which it was calibrated, but generalize poorly when used to simulate other configurations not included in the training. Due to this poor generalization, the predictions of such models may severely deteriorate as model parameters are allowed to deviate from their nominal settings to account for parameter

uncertainty. Therefore, it is necessary to strike a balance between fidelity to data and robustness to uncertainty in the selection of model forms. The role of model complexity in determine the credibility of predictions is demonstrated in a model selection problem, where the FE model of the CX-100 wind turbine is modified to simulate an experimental configuration in which large masses are added to load the blade in bending.

Similarly, *non-uniqueness issues can arise in the model calibration process*, where multiple sets of calibration parameters may be capable of replicating experimental data with similar fidelity to data and robustness to uncertainty. In this dissertation, to address the concerns regarding non-uniqueness, self-consistency of model predictions is considered in the development of a one-dimensional beam model to replace the three dimensional FE model of the CX-100.

1.3 Main Dissertation Contributions

This dissertation takes a step toward understanding the limitations of M&S by evaluating the trade-offs of fidelity-to-data and robustness-to-uncertainties. The explicit use of V&V exercises combined with IGDT as developed in this dissertation provides a holistic analysis of the predictive capabilities of numerical models. Specifically, this dissertation contributes to modeling and simulation efforts for wind energy applications.

The first contribution of this dissertation relies on providing a completely integrated approach for the V&V activities utilized in the development of the simplified FE model used to simulate the CX-100 wind turbine blade. Instead of choosing the mesh size that produces the smallest numerical uncertainty, it is selected such that the overall numerical uncertainty caused by truncation effects is similar to, or smaller than, experimental variability. This rationale guarantees that predictions are sufficiently accurate relative to the level of uncertainty, with which physical tests can be replicated. The application of V&V activities include performing forward

propagation of uncertainty in a design of computer experiments, developing a Phenomenon Identification and Ranking Table to identify the statistically significant parameters for calibration, and performing calibration in a Bayesian context rather than producing a best-fit to experimental data to reduce the lack-of-knowledge of material properties and boundary springs. To demonstrate the predictive capability of the numerical model, the overall validation assessment is grounded in the test-analysis correlation of data that has not been used during sensitivity analysis and quantification. The successful validation exercises demonstrate un-equivocally the ability of simplified models to remain consistent with experimental data when simulating the structural response of wind turbine blades.

Next, this dissertation demonstrates the use of IGDT to address the effect of complexity in model selection. Two working numerical simulations of experimental tests performed at the National Renewable Energy Laboratory are developed, each based on their own modeling assumptions and involving different sources of uncertainty. IGDT is then applied to explore the trade-offs between, on one hand, the ability of each model to reproduce the experimental measurements and, on the other hand, the robustness of their predictions to parametric and modeling uncertainty to provide a systematic and rigorous approach to model selection.

IGDT is then used to address non-uniqueness concerns that arise during model calibration exercises, where different parameter sets are capable of providing similar fidelity to data and robustness to uncertainty. The development of parameters is addressed by evaluating both the fidelity to data and self consistency of predictions used in model development through single-objective global optimization. Through the use of IGDT, a novel quantification of robustness is proposed for use in the objective function. It is demonstrated that there is a *trade off* in the development of fidelity to data, robustness-to-uncertainty and self consistency of predictions, and

that the model that offers the best evaluation for one of the criteria will not necessarily offer the best performance for the other two criteria.

1.4 Dissertation Organization

The wind turbine blade used as a case study application is the CX-100, developed as part of the Blade Systems Design Study at Sandia National Laboratories. The CX-100 is nine-meters long, developed in a research effort to pursue alternative designs through relatively affordable blades created at a modest scale (Berry 2007). When first developed in 2002, the full-length carbon-spar cap implemented in the blade was an innovative concept (Paquette and Veers 2007).

This dissertation[1] begins with the development of a three dimensional FE model of the blade, using the NuMAD preprocessor developed at SNL, and imported into ANSYS v.12.1, commercially available FE software. Code verification is performed to demonstrate that the software behaves as expected, and solution verification is performed to choose the appropriate mesh size. Experimental modal data, collected from laboratory experiments at the Los Alamos National Laboratory (LANL), is used in a Bayesian calibration of the model. While calibration is performed using natural frequencies, model validation is performed using mode shape vectors, demonstrating that the FE model is capable of performing in a predictive capacity. The integrated

[1] Chapters 2-6 in this dissertation serve as stand-alone publications, thus, some level of conceptual overlap is encountered.

V&V approach is discussed in Chapters 2 and 3, both of which are published in Elsevier's Wind Energy journal as two-part companion manuscripts.

Chapter 4 discusses the use of IGDT to choose between different model forms in simulating experimental modal data of the CX-100 collected at the National Renewable Energy Laboratory (NREL). The NREL experimental modal analysis is performed with masses attached to the blade, due to their use in fatigue testing. The FE model developed in Chapters 2 and 3 is utilized to simulate the experimental configuration, with large masses added onto the blade utilizing different modeling strategies: (i) solid elements, and (ii) with point masses and stiffening springs. Through IGDT, it is found that the model utilizing solid elements is not only more accurate, but also more robust. The model selection approach along with the findings presented in Chapter 4 is submitted to Elsevier's Journal of Mechanical Systems and Signal Processing and is currently under review.

In Chapter 5, the three-dimensional model developed in Chapters 2 and 3 is used to derive initial values for the material properties of a one-dimensional beam model representation of the CX-100 blade. IGDT is used to assess the robustness-to-uncertainty of model parameter sets of the CX-100 developed for use in *NLBeam*, a LANL developed FE code used to model wind turbine blades as beam elements. Calibration is performed by simultaneously considering the fidelity to data and robustness-to-uncertainty of model predictions. In a separate step, self-consistency of model predictions is then used to assess the consistency of predictions of tip deflection due to a fictitious load. It is found that while all three criteria are not satisfied at the same time, a trade-off can be established. The concept of investigating the trade-off between fidelity and robustness as discussed in Chapter 5 is submitted to Elsevier's Journal of Finite Element Analysis and Design and is currently under review.

Chapter 6 provides a discussion of the limitations and assumptions, and a summary of the major findings of the work presented herein. The work presented herein can be extended to future numerical studies, and a brief discussion of avenues for future work is discussed.

References

Adams, D., White, J., Rumsey, M., Farrar, C., "Structural health monitoring of wind turbines: method and application to a HAWT," Wind Energy, Vol. 14, No. 4, pp 603-623, 2011.

Berry, D., "Design of 9-Meter Carbon-Fiberglass Prototype Blades: CX-100 and TX-100," Sandia Report, SAND2007-0201, Sandia National Laboratories, Albuquerque, NM, 2007.

Ciang, C.C., Lee, J.R., Bang, H.J., "Structural health monitoring for a wind turbine system: a review of damage detection methods," Measurement Science and Technology, Vol. 19. No. 12, pp. 122001, 2008.

Freebury, G., Musial, W., "Determining equivalent damage loading for full-scale wind turbine blade fatigue tests," 19th ASME Wind Energy Symposium, Reno, NV, 2000.

Hansen, M.O.L., Sørensen, J.N., Voutsinas, S., Sørensen, N., Madsen, H.Aa., "State of the art in wind turbine aerodynamics and aeroelasticity," Progress in Aerospace Sciences, Vol. 42, pp. 285-330, 2006.

Hemez, F.M., Ben-Haim, Y., "The Good, the Bad, and the Ugly of Predictive Science," 4th International Conference on Sensitivity Analysis of Model Output, Santa Fe, NM, March 2004.

Jensen, F.M., Falzon, B.G., Ankersen, J., Stang, H., "Structural testing and numerical simulation of a 34 m composite wind turbine blade," Composite Structures, Vol. 76 No. 1-2, pp. 52-61, 2006.

Larsen, F.M., Sørensen, T., "New lightning qualification teest procedure for large wind turbine blades," Proceedings of International Conference on Lightning and Static Electricity, Blackpool, U.K., 2003.

Liu, W., Tang, B., Jiang, Y, "Status and problems of wind turbine structural health monitoring techniques in China," Renewable Energy, Vol 35, No. 7, pp. 1414-1418, 2010.

Overgaard, L.C.T., Lund, E., Thomsen, O.T., "Structural collapse of a wind turbine blade. Part A: Static test and equivalent single layered models," Composite Part A: Applied Science and Manufacturing, Vol. 41, No. 2, pp. 257-270, 2010.

Paquette, J.A., Veers, P.S., "Increased Strength in Wind Turbine Blades through Innovative Structural Design," European Wind Energy Conference Proceedings, Milan, Italy, 2007.

U.S Department of Energy. "20% Wind Energy by 2030." July 2008.

Veers, P.S., Ashwill, T.D., Sutherland, H.J., Laird, D.L., Lobitz, D.W., Griffin, D.A., Mandell, J.F., Musial, W.D., Jackson, K., Zuteck, M., Miravete, A., Tsai, S.W., Richmond, J.L., "Trends in the Design, Manufacture, and Evaluation of Wind Turbine Blades," Wind Energy, Vol. 6, No. 3, pp. 245-259, 2003.

CHAPTER TWO

SIMULATING THE DYNAMICS OF WIND TURBINE BLADES: PART I, MODEL DEVELOPMENT AND VERIFICATION

2.1. Introduction

Wind power in the United States has the potential to supply a major amount of electricity. This objective is outlined by the *"20% by 2030"* initiative of the U.S. Department of Energy (DOE), whereby DOE identifies wind energy as a viable source to contribute to 20% of installed energy, assuming a 39% increase in demand for electricity.[1] This ambitious objective has enormous implications for the wind power market that supplied only 2% of electrical energy in the U.S. by the end of 2009.

For the increased use of wind energy to be realized the cost of energy needs to decrease significantly. This can be facilitated by understanding wind turbine failures so that they can be better prevented. It has been shown that damage to wind turbine components, such as the generator, drive train, hub, gearbox, and blades, can result in periods of downtime, in which the wind turbine is temporarily taken out of service.[2] The combination of repair and loss in energy production during downtime can negatively impact the sales, and profitability model of an entire wind plant.[3] This study focuses on wind turbine blades because they are first in line to capture the kinetic energy of the wind, and also produce all of the loads for the entire system.[4] Furthermore, even minor damage to blades can progress to serious secondary damage to the entire wind turbine system.[5]

Modeling and Simulation (M&S) will play an indispensable role in the development of future wind turbine blades, whether it is to understand blade vibrations, simulate the loading environment that vibrations generate on the main shaft assembly, or predict the occurrence and

severity of structural damage. It is also forecasted that M&S will be essential to filter a wide variety of plausible design concepts down to the most effective ones.[6]

The current state-of-the-practice of M&S and availability of computing resources for engineering applications necessitate a certain tradeoff between the implementation of large-scale, high fidelity models, and the use of simplified models that are much less computationally expensive. It is desirable to assess, for example, the potential consequences of structural damage on blade performance, but large-scale models are too demanding of computational resources to be implemented for rapid prototyping and diagnostics. For this reason, the study presented in this paper and companion publication[7] proposes to develop a finite element model that, while simplified as much as possible, still captures the main dynamics of interest. Importantly, this trade-off is quantified, allowing the process to run along methodical, and not arbitrary, grounds. V&V activities discussed in these two manuscripts are essential steps of the model development process to guarantee that the simplifications introduced are justified for the intended purpose.

In this study, V&V activities are applied in the development of a Finite Element (FE) model of the CX-100 wind turbine blade using NuMAD[8], preprocessing software developed at the Sandia National Laboratories (SNL) and imported to ANSYS version 12.1. The CX-100 wind turbine blade is a nine-meter research blade developed at the Sandia National Laboratories (SNL) in 2002 as a part of ongoing research efforts to improve the performance of wind turbine blades.[6] The CX-100 was developed for the purpose of studying the performance, and reducing the energy production costs, of wind turbine blade designs that utilize light-weight carbon fiber material to reinforce the spar cap.[9] Our main goals are to develop a validated simulation of the low-frequency dynamics and quantify the uncertainty that arises, both from the potential lack-of-resolution in calculations and from uncertainty relating to parameter estimation. The dynamics of interest for this study are the first three flap-wise bending modes. The model developed herein relies on a

strong simplification: the cross-sectional areas of the blade are smeared, using isotropic material properties, instead of modeling the multiple composite layers embedded in an epoxy matrix. Credibility of the simulation rests on our ability to quantify various sources of numerical, modeling and experimental uncertainties.

The manuscript is organized as follows. Section 2 briefly discusses pertinent literature from the discipline of wind turbine blade modeling and testing. An upper bound of solution uncertainty is derived in section 3 to guide the selection of an appropriate level of mesh discretization. Code verification activities are presented in section 4. Section 5 discusses the experimental setup and measurements collected from vibration testing. Finally, the upper bound of solution uncertainty (derived in section 3) is combined to the experimental variability (estimated in section 5) to arrive at a rational and scientifically defendable selection of mesh resolution in section 6.

2.2. Review of Pertinent Literature

An issue relating to the development of FE models was revealed in 2005, when a code verification study of shell elements was performed to explore whether the implementation of shell elements in FEA software (which have since been modified) were appropriate to model the torsional response of wind turbine blades.[10] The study found that shell elements modeled with nodes at the exterior surface for a hollow cylinder deviated significantly from the closed-form solution for torsional stress. This error was especially unfortunate in that the results for the shell elements diverged from the exact solution as the mesh was refined. This formulation, in which the nodes of the shell element are at the exterior surface (as opposed to the middle), is common in wind turbine blade modeling. This deficiency of earlier shell elements shows that a simple code verification study is necessary to establish credibility of numerical simulations, because it brings

into question the dependability of FE predictions and M&S efforts performed prior to this finding.

Additionally, verification campaigns frequently execute mesh refinement by less-than-rigorous methods, in which a mesh is ultimately selected at an arbitrary density. A common practice is to select the resolution of a mesh discretization by completely qualitative methods, or simply to obey the constraints defined by the computational resource available. To effect truly credible predictions, verification activities should include quantitative methods of determining the uncertainty of numerical simulations.[11] Selecting a proper mesh discretization can be achieved by several helpful metrics for extrapolation and quantification of truncation error, which are well understood.[12]

Experimental Modal Analysis (EMA) has been used to study the vibration response of wind turbine blades. There are two typical testing configurations in EMA: free-free, in which the testing specimen is suspended in the air (using straps or cushions) such that the response is as though there is no imposed boundary condition; and fixed-free, in which movement is constrained at the support of the testing specimen. Previous studies discuss that the use of a free-free boundary condition, though less applicable to reality, is common because it is easy to implement under laboratory conditions.[13,14] In comparison, it is significantly more difficult to achieve an idealized fixed-end condition in experimental testing of wind turbine blades. Furthermore, methods have been proposed to quantify uncertainty to account for variability in modal testing of the SNL research blades.[15,16,17] In one instance, for a free-free analysis, the variability of test results are quantified to account for the support conditions, mass loading of the accelerometers, cable effects on the free-free condition, and temperature of the ambient environment. In addition, natural variability is considered to investigate the repeatability of measured natural frequencies from one test specimen to another. The results from these studies help to quantify sources of

uncertainty (relative to each other) and provide important considerations for the free-free modal testing of wind turbine blades.

It is important to propose a robust methodology to develop FE models, because as previously observed, there can be variability during experimental testing of wind turbine blades that will result in slightly different responses.[15] In addition to variation among the blades, further variation will result due to the experimental campaigns (calibration errors, test-to-test variability, etc.), hence, requiring even more robustness in the analysis. This publication and its companion second part propose such methodology that accounts for the experimental variability, numerical uncertainty, and modeling uncertainty introduced, for example, by the lack-of-knowledge in constitutive material properties.

2.3. Derivation of an Upper Bound of Solution Uncertainty

Because numerical uncertainty is an essential part of our quantification effort for V&V, we start by proposing an upper bound of solution uncertainty based on the concept of asymptotic convergence. The upper bound arrived at is compared to the well-known Grid Convergence Index (GCI) of Reference 18 and used in Section 6 to select an appropriate mesh size.

2.3.1 Derivation on an Upper Bound of Solution Uncertainty

The partial differential equations solved by a numerical method, such as a FE software, always provide an approximation of the "exact-but-unknown" solution of the continuous equations. Such an approximation comes in two steps, according to the formalism established by the Lax equivalence theorem.[19] Convergence states that the code **self-converges** to a solution denoted by the symbol y*, or "$y(\Delta x) \rightarrow y^*$," as the level of resolution in the calculation increases. Consistency of the numerical method, on the other hand, provides "$y^* \rightarrow y^{Exact}$." For simple test problems, the unknown solution y* can be obtained from Modified Equation Analysis (MEA), as

explained in References 20 and 21. The distinction between solutions y* and y^{Exact} emphasizes that a code could potentially self-converge to a solution that is different from the exact solution.

For practical applications that involve complicated geometries, boundary conditions, or forcing functions, the exact solution y^{Exact} cannot be derived in closed form. Likewise MEA becomes intractable, which prevents the derivation of the solution y*. Our purpose, therefore, is to bound the difference $|y^* - y(\Delta x)|$. For a consistent numerical method, and in the limit of asymptotic convergence, the discrete solutions $y(\Delta x)$ converge to the solution y* of the modified equation which, in turn, reduces to the exact-but-unknown solution y^{Exact} as $\Delta x \rightarrow 0$. Because these solutions are "equal" only in the asymptotic limit, we seek an upper bound of solution error defined as:

$$|y^* - y(\Delta x)| \leq U(\Delta x) \cdot |y(\Delta x)|. \quad (1)$$

In the application of section 5, y* denotes the best-possible estimation of an "exact-but-unknown" natural frequency while $y(\Delta x)$ is the approximation obtained by running the calculation at mesh size Δx.

A solution for the upper bound $U(\Delta x)$ can be derived by examining the relationships between the discrete solutions resulting from a coarse-mesh (Δx_C) and a fine-mesh (Δx_F) discretization. If the resolutions Δx_C and Δx_F provide discrete solutions within the regime of asymptotic convergence, the following (approximate) equations can be postulated:

$$y^* \approx y(\Delta x_F) + \beta \cdot \Delta x_F^{\,p} \quad \text{and} \quad y^* \approx y(\Delta x_C) + \beta \cdot \Delta x_C^{\,p}, \quad (2)$$

where β is a pre-factor coefficient and the exponent p denotes the rate of convergence. This formalism derives from MEA, as mentioned previously.[21] MEA defines a Taylor series-like expansion that is usually infinite and whose sophistication depends on the combination of partial differential equations solved and properties of the numerical method implemented.

Equations (2) are simple approximations of the MEA where the higher-order terms are ignored, the pre-factor β is assumed to be constant (which is generally not the case), convergence is monotonic as $\Delta x \rightarrow 0$, and analysis is restricted to scalar-valued quantities (Reference 22 offers a generalization to 1D curves or multi-dimensional fields). These assumptions translate the fact that truncation effects (caused by mesh discretization) dominate the overall production of numerical error within the regime of asymptotic convergence. It can be observed that, if expressed on a logarithmic scale, equations (2) define a linear relationship between the errors and mesh sizes. The slope of this linear relationship (or exponent p) provides the order of accuracy of the numerical method.

An elementary rearrangement of the well-known triangular inequality $|a| + |b| \geq |a + b|$ produces the form $|c - d| \geq |c| - |d|$. (Simply substitute $c = a + b$, $d = b$.) From this, using the quantities:

$$c = y(\Delta x_C) - y^* \quad \text{and} \quad d = y(\Delta x_F) - y^*, \tag{3}$$

combined with equations (2), and incorporating the assumption that convergence is monotonic (such that the sign of the pre-factor coefficient β can be kept constant), results in:

$$|y(\Delta x_C) - y(\Delta x_F)| \geq |y^* - y(\Delta x_C)| - |y^* - y(\Delta x_F)| \approx \beta \cdot \Delta x_C{}^p - \beta \cdot \Delta x_F{}^p. \tag{4}$$

Using the mesh refinement ratio defined as $R = \Delta x_C / \Delta x_F > 1$, equation (4) becomes:

$$|y(\Delta x_C) - y(\Delta x_F)| \geq \beta \cdot \Delta x_F{}^p \cdot (R^p - 1). \tag{5}$$

Inserting the first one of equations (2) to replace the term $\beta \cdot \Delta x_F{}^p$ in equation (5), we arrive at:

$$|y(\Delta x_C) - y(\Delta x_F)| \,/\, (R^p - 1) \geq |y^* - y(\Delta x_F)|. \tag{6}$$

This final equation is the upper bound sought. When the exact solution y^{Exact} of the continuous equations is unknown, which is generally the case of a general-purpose FE calculation, one can no longer talk of an "error." The difference $|y^* - y(\Delta x)|$ in the right-hand side of equation (6)

becomes an **uncertainty** due to truncation effects. The best that one can achieve is to bound this uncertainty at any given level of mesh resolution Δx.

2.3.2 Analogy to the Grid Convergence Index

Our proposal for an upper bound U(Δx) of solution uncertainty at mesh resolution Δx is:

$$U(\Delta x) = \frac{|y(R \cdot \Delta x) - y(\Delta x)|}{(R^p - 1)}, \tag{7}$$

where Δx is a characteristic mesh size of the calculation and R denotes the refinement ratio (where, by definition, R > 1). It is emphasized that definition (7) only requires two calculations at the coarse and fine levels of mesh resolutions $\Delta x_C = R \cdot \Delta x$ and $\Delta x_F = \Delta x$, respectively.

This definition is analogous to the GCI of References 12 and 18, defined as:

$$GCI(\Delta x) = \frac{F_S}{(R^p - 1)} \left| \frac{y(R \cdot \Delta x) - y(\Delta x)}{y(\Delta x)} \right|, \tag{8}$$

where F_S denotes the so-called "safety factor" added to provide conservatism, and generally chosen within the range $1 \leq F_S \leq 3$. Clearly the upper bound (7) of solution uncertainty is related to the GCI by the following equation where $F_S = 1$:

$$U(\Delta x) = GCI(\Delta x) \cdot |y(\Delta x)|. \tag{9}$$

Even though the definitions are similar, modulo $F_S = 1$, it is emphasized that the motivation put forth by P.J. Roache is different. The GCI is explained by its author in Reference 18 as:

> *"The idea behind the proposed GCI is to approximately relate the ε […] obtained by whatever grid convergence study is performed (whatever p and r) to the ε that would be expected from a grid convergence study of the same problem with the same fine grid using p = 2 and r = 2, i.e., a grid doubling with a second-order method."*

This explanation justifies the choice of a safety factor $F_S = 3$ to cancel out the $(R^p - 1)$ term in equation (8). This renders the GCI of an arbitrary mesh refinement study comparable to a value obtained with R = 2 (grid doubling) and p = 2 (second-order accurate method).

To the best of the authors' understanding, the GCI was not proposed initially as an attempt to define an upper bound of solution uncertainty. Equation (9) sheds new light on an index that can be used to estimate where the "exact-but-unknown" solution y* may be located relative to a discrete solution obtained by analyzing the problem with a level of mesh resolution Δx. This is analogous to statistics obtained from physical observations, such as a mean value, that come with an uncertainty that estimates the unknown value of the experimental setup. The upper bounds of solution uncertainty presented in section 5 are based on equations (8-9) with $F_S = 3$.

2.4. Code Verification Activities

Code verification is the first step of the V&V study. "Spot check" verification is performed to assure that the FE software is running properly, without any significant programming mistake that would negatively impact the results sought. One specific area of concern is that, in the past, shell elements have been found to have shortcomings in torsion.[10] Because the first torsion of the wind turbine blade is of interest, this potential issue warrants careful investigation.

To verify the correctness of implementation of shell elements in ANSYS, together with their numerical performance, a simple hollow cylinder with known analytical solution is modeled. (This, by design, hews closely to the modeling performed in Reference 10.) ANSYS version-12.1 is used to model and analyze this code verification test problem for which three scenarios are explored: 1) a bending load is applied to a fixed-free cylinder, 2) a torsion load is applied to the same fixed-free cylinder, and 3) the modal analysis of a fixed-fixed cylinder is carried out. These three scenarios feature the same geometry with different cases of loading and boundary condition.

The varying boundary conditions are explored to assess the ability of the code to predict more than one configuration. In addition to the fixed-free boundary, a fixed-fixed setup is exercised because implementing a fixed boundary is somewhat more complicated and, therefore, prone to potential mistakes in the analysis software.

2.4.1 Verification of the Bending Stress

The bending stress is verified by reporting results from the shell elements at mid-section where there is no membrane-bending coupling. The closed-form solution for the bending stress is:

$$\sigma = \frac{M \cdot c}{I}, \tag{10}$$

where σ denotes the maximum normal stress due to bending, M is the bending moment, c is the greatest distance from the neutral axis, and I represents the cross-sectional moment of inertia.

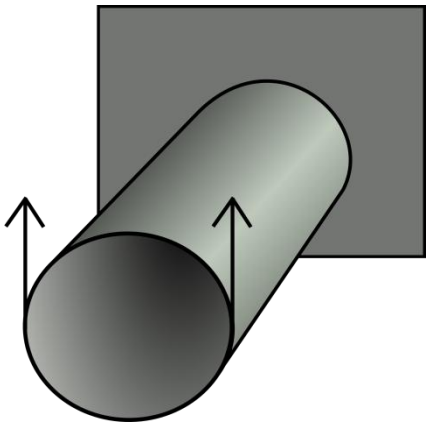

Figure 2.1: Definition of the hollow cylinder-in-bending test problem.

Figure 2.1 illustrates one of the meshes analyzed where the bending load is applied. The vertical, upward-pointing arrows indicate the location and direction of the applied load. The analysis of the same test problem is repeated with increasing levels of mesh resolution. Figure 2.2 shows the solution error as a function of mesh size. The percentages of solution error are depicted on the left and the asymptotic convergence of numerical solutions is illustrated on the right.

It can be observed from Figure 2.2 that, as expected, the solution error decreases as a function of mesh resolution. A model with fewer than 1,000 elements produces less than 1% error between the predicted bending stress and analytical solution of equation (10). In addition, the log-log representation indicates that solution error converges with a rate-of-convergence of p = 2.17. This observation matches expectation because quadratic shell elements, which are expected to produce an accuracy of $p^{Theory} = 2$, are used for discretization. It is concluded that the element is implemented correctly and performs according to expectation to model the response under bending load.

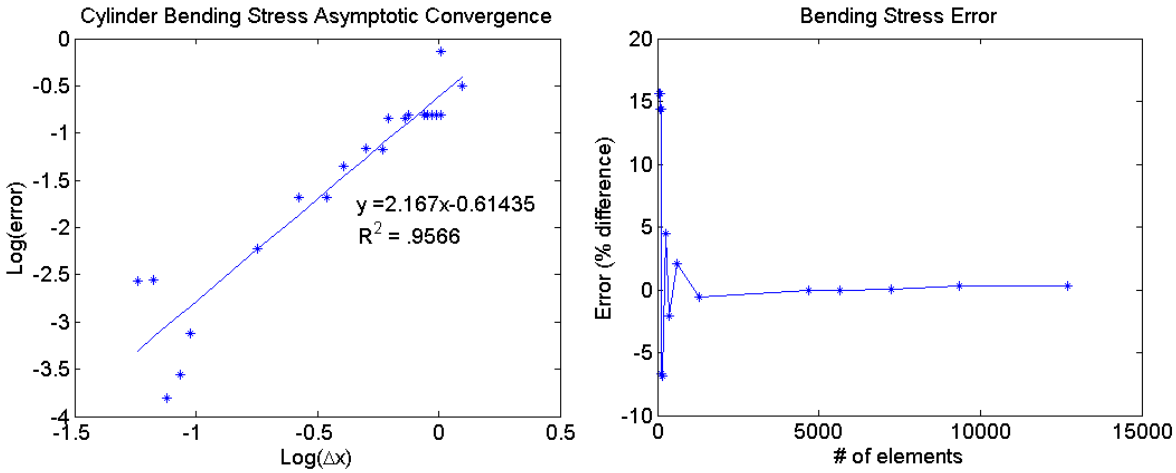

Figure 2.2: Solution error (left) and asymptotic convergence (right) of the bending problem.

An inspection of asymptotic convergence in Figure 2.2 (right) reveals that the convergence is not quite monotonic. Solutions produced by the two finest meshes actually have greater errors than any of the next three solutions obtained with coarser meshes. The reasons for these oscillations are not apparent, though it is suspected that such effects owe either to round-off errors or to finite elements demonstrating uncharacteristic behavior at sufficiently small sizes. Because our analysis searches for overall trends using simple power-laws, such as the best-fitted

model $\log(|\sigma^* - \sigma(\Delta x)|) = 2.17 \cdot \log(\Delta x) - 0.61$ illustrated in Figure 2.2 (right), we believe that our conclusions are not adversely affected by this erratic behavior.

2.4.2 Verification of the Shear Stress

A similar analysis is performed for the case of a torsion load. The closed-form solution is:

$$\tau = \frac{T \cdot r}{J}, \tag{11}$$

where τ denotes the maximum shear stress due to torsion, T is the torque applied, r is the outer radius of the cylinder, and J represents the polar moment of inertia.

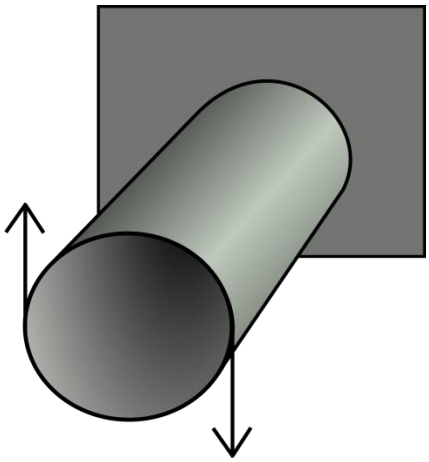

Figure 2.3: Definition of the hollow cylinder-in-torsion test problem.

Figure 2.3 illustrates the test problem where the applied load is indicated by opposite-pointing arrows that define the torsion. The overall evolution of solution error as a function of mesh resolution is depicted in Figure 2.4.

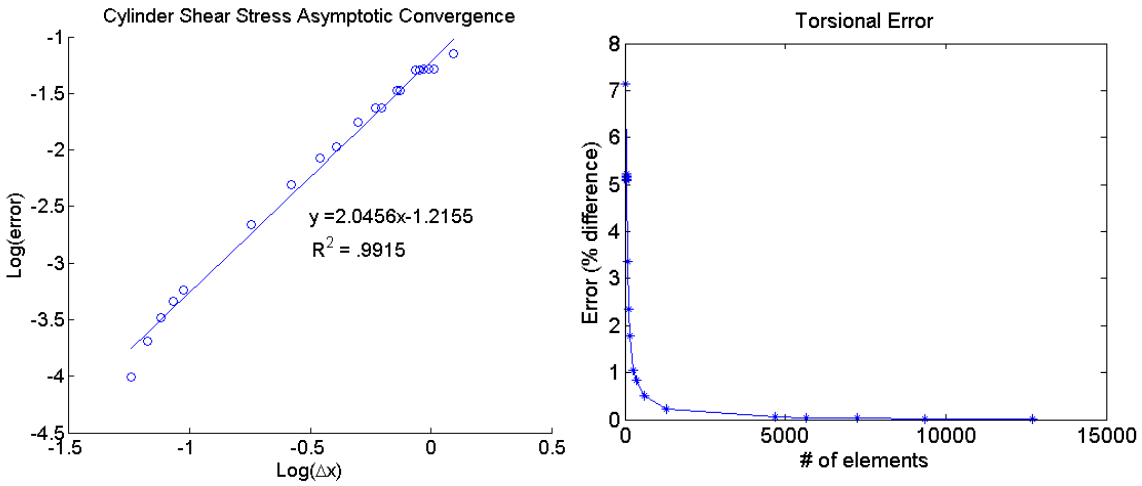

Figure 2.4: Solution error (left) and asymptotic convergence (right) of the torsion problem.

As noted previously, it can be observed from Figure 2.4 that fewer than 1,000 finite elements are needed to reach less that 1% error between the predicted shear stress and analytical solution of equation (11). The log-log representation leads to an observed rate-of-convergence of p = 2.05. Also noticeable is the stable behavior of the shell element in torsion, as indicated by a solution error that is more predictable than the error in bending (Figure 2.3, right) as the mesh resolution is refined. These observations are strong evidence that the shell element implemented in ANSYS performs according the expectation of second-order accuracy to model the response under both bending and torsion loads.

2.4.3 Verification of the Modal Solution

`Because the FE model is ultimately used to simulate the vibration response of a wind turbine blade, the ability of the ANSYS shell element to reach an accurate modal solution also needs to be verified.

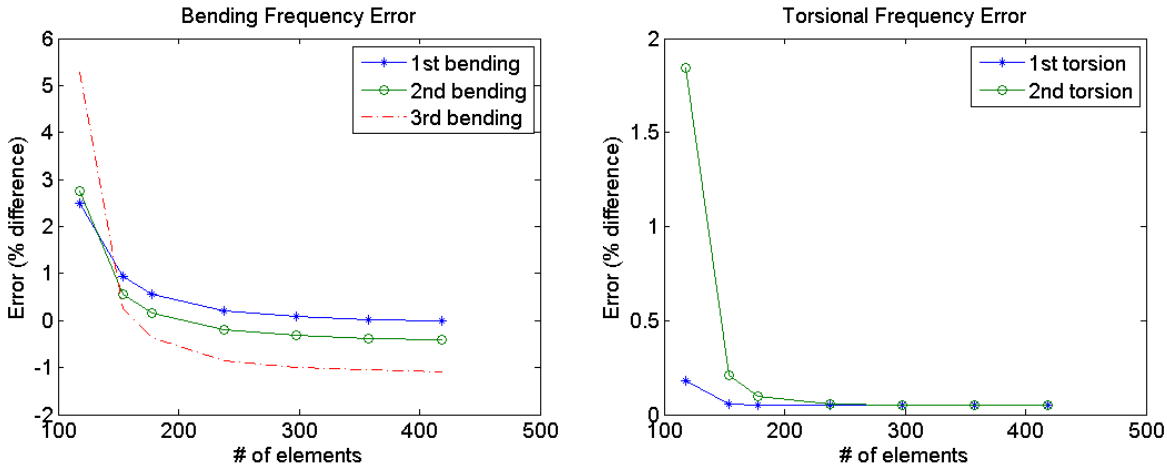

Figure 2.5: Solution errors for bending (left) and torsion (right) natural frequencies.

A third test problem is analyzed to simulate the vibration of a simply supported, hollow cylinder without axial constraint. High-accuracy approximations of the natural frequencies of vibration are obtained from Reference 23, and used as substitutes to the "exact-but-unknown" solutions. Figure 5 plots the relative frequency errors in bending and torsion as a function of Δx.

Figure 2.5 (left) indicates that fewer than 100 elements suffice to predict the first three bending frequencies of the hollow cylinder to within 1% error, or less. Figure 2.5 (right) shows that a finer mesh with 250 elements converges to less than 0.1% error, confirming the ability of the shell elements to predict the torsion frequency.

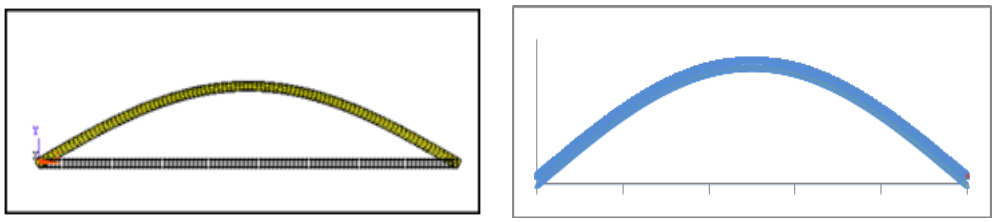

2.6-a) Simulation (left) and closed-form solution (right) for the first bending mode.

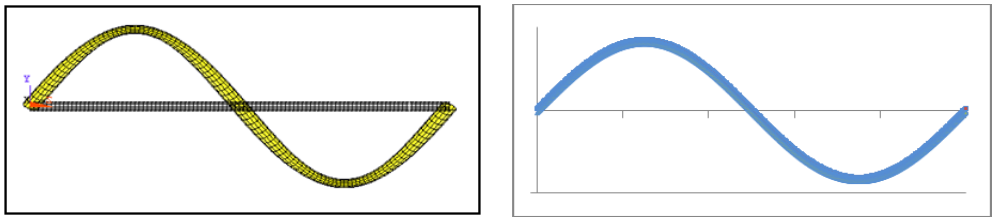

2.6-b) Simulation (left) and closed-form solution (right) for the second bending mode.

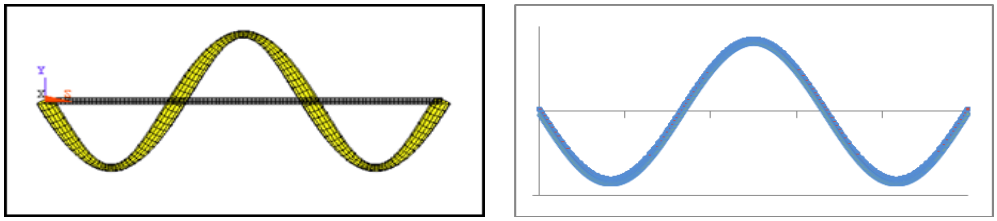

2.6-c) Simulation (left) and closed-form solution (right) for the third bending mode.

Figure 2.6: Comparison of simulation and closed-form mode shape deflections.

Figure 2.6 shows the agreement between simulated (left) and closed-form (right) mode shapes for the first three bending modes. The figure illustrates the excellent level of correlation with which mode shape deflections are predicted. This observation increases confidence in the ability of the FE model to accurately capture the bending of the main spar cap of the wind turbine blade.

2.4.4 Verification of the Pre-processing Software NuMAD

After satisfactorily checking the quality of the ANSYS software, it is next desired to perform accompanying code verification studies of the NuMAD pre-processor, developed by SNL to ease the production of FE models of wind turbine blades. This software receives information of cross-sectional geometry at each station and material properties for each section comprising the structure. It produces a text file (written in ANSYS parametric design language) that defines an ANSYS model corresponding to these characteristics.

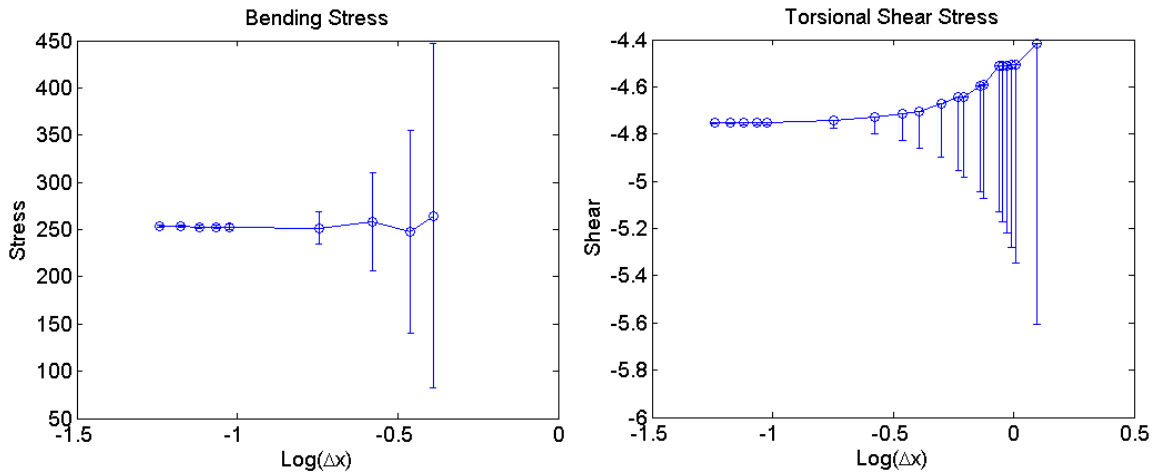

Figure 2.7: Solutions for bending (left) and torsion (right) stress, with uncertainty bound.

To verify the suitability of a NuMAD-generated model, the cylinders created in sections 4.1 and 4.2 are recreated with NuMAD. The main difference is that constraint equations are imposed for all nodes at the tip, or free, end of the blade so that the shape cannot be deformed. However, the material properties are stiff enough in the unconstrained, ANSYS-based setup that effects of this change never become apparent. Mesh refinement is performed to assess the performance of the NuMAD-generated model for bending and shear stresses.

The results are similar to those obtained above. As an alternative illustration of the convergence upon the true solution, Figure 2.7 shows the bending and torsional stress solutions when solved by ANSYS using the NuMAD pre-processor. The analysis uses the GCI to describe the bounds of solution uncertainty due to truncation error (see equations (8-9) of section 3). Stress values and uncertainty bounds are shown in Figure 2.7 as a function of element size. The upper bounds function as expected: the exact solutions of equations (10) for bending and (11) for torsion, are converged upon as the element size is refined. Even though not indicated by Figure 2.7, it is also verified that, for larger element sizes, the upper bounds always contain the exact solutions.

Figure 2.7 indicates that one significant difference between bending (left) and torsion (right) is that asymptotic convergence is monotonic in the latter case, hence, producing one-sided bounds of solution uncertainty. On the other hand, convergence of the bending stress is oscillatory, which leads to two-sided bounds of uncertainty since the two cases "$y(\Delta x) \geq y^*$" and "$y^* \geq y(\Delta x)$" are possible as $\Delta x \rightarrow 0$. Based upon the agreement between the exact and discrete solutions for the NuMAD-created cylinder test problem, it is deemed satisfactory that the pre-processing software accomplishes the basic function it purports to do.

2.5. Experimental Modal Analysis of the Wind Turbine Blade

At this point of the study, the ANSYS code for FE modeling, and its pre-processor software NuMAD, have undergone sufficient code verification activities for the purpose intended. A model of the CX-100 wind turbine blade is generated, as described in section 6 below. One lingering question in the development of the FE model is the selection of an appropriate mesh size for the calculations. This question refers to the level of discretization needed to support sensitivity analysis and uncertainty quantification.[7]

Modal testing of the CX-100 blade is performed under free-free and fixed-free boundary conditions at Los Alamos National Laboratory (LANL). These measurements are used, not only to calibrate parameters of the simplified model as explained in Reference 7, but also to guide the choice of an appropriate level of mesh resolution. This is a significant departure from the common V&V paradigm that tends to promote a strict separation between code verification activities and comparison between predictions and measurements. It is emphasized that only the experimental **variability**, and not the measured response, is used.

Testing includes exploring the overall levels of experimental variability that result from using different setups where excitation locations, excitation types and support conditions are varied to quantify their potential effects on system identification. Roving impact hammer test are

performed to collect modal data with uniaxial accelerometers at three locations on the blade. A linear average with five repeats and a 150-Hertz sampling frequency is used. The acceleration response is measured for eleven seconds. No window function is applied due to the relatively long sampling period. Figure 2.8 depicts one of the setups tested (left) and shows a close-up of the grid used to record locations used for excitation and sensing (right). Reference 7 discuses the effect that varying these configurations has on the identification of resonant mode shapes and natural frequencies, in comparison to corresponding predictions of the FE model.

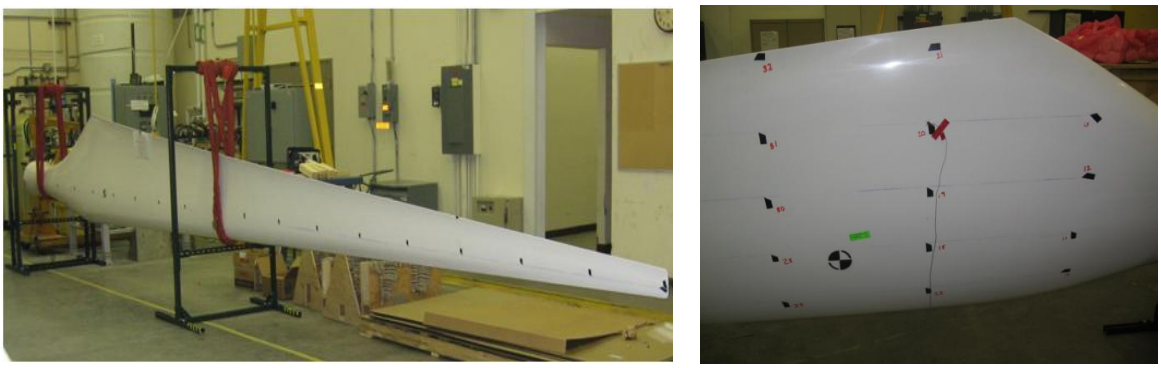

Figure 2.8: Free-free modal testing configuration (left) and close-up on sensing (right).

The experimental investigation also includes performing linearity and reciprocity checks to verify the quality of datasets collected. A linearity check consists of testing the CX-100 blade with increasing levels of force excitation. A structure that responds linearly, which is a fundamental assumption of the system identification method used to extract the resonant modes, should yield similar Frequency Response Function (FRF) curves regardless of the applied force. A reciprocity check consists of swapping pairs of excitation and sensing locations to compare FRF curves. Another assumption of linear structural dynamics is that the load path from Point-A to Point-B is identical to the reverse path. Establishing that the FRF curves are, again, similar verifies the assumption of reciprocity.

Figure 2.9 illustrates that, for these series of modal tests, the CX-100 blade behaves as a linear structure and exhibits reciprocity. The FRF curves compared on the left originate from modal tests performed with different levels of force excitation. It is observed that their agreement is excellent. Likewise, the curves compared on the right of Figure 2.9 originate from a reciprocity test at two locations, and the same conclusion is reached. The reader is referred to Reference 24 to learn further details about the experimental setup and results of these vibration tests.

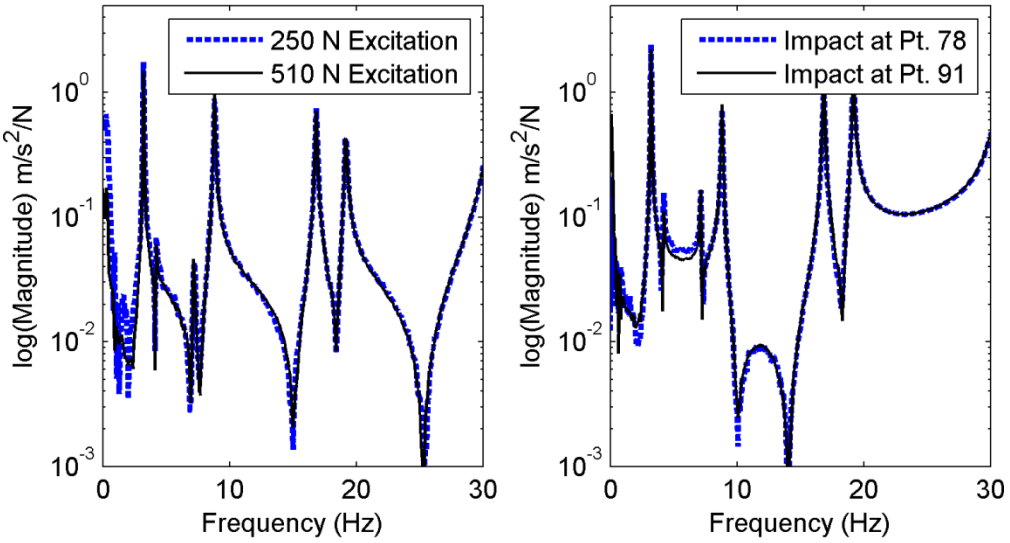

Figure 2.9: Verification of linearity (left) and reciprocity (right) during modal testing.

The levels of variability observed are quantified and listed in Table 2.1, summarizing results for testing the blade with free-free boundary conditions. Overall, very low levels of variability are obtained, which are due to replicated modal tests on the same wind turbine blade. This quantification of experimental variability does not account for specimen-to-specimen variability, experimenter variability, or test setup repeatability. These results are also used in the companion publication as "baseline" for inference of the idealized material properties of the FE model.[7]

Table 2.1: Statistics of system identification obtained for the CX-100 blade.

Type of Mode	Mean Statistic	Standard Deviation	Variability[(1)]
First flap-wise bending	7.617 Hertz	0.004 Hertz	0.06%
Second flap-wise bending	20.167 Hertz	0.055 Hertz	0.27%
Third flap-wise bending	32.256 Hertz	0.051 Hertz	0.16%

Legend: [(1)] The coefficient of variance listed in the last column is defined as the standard deviation (3rd column) divided by the mean (2nd column). These statistics are based on 27 replicates for the free-free vibration tests.

Besides providing important information for test-analysis correlation, the statistics of Table 2.1 are also used to guide the selection of a mesh size Δx at which the subsequent parametric studies (sensitivity analysis, inference uncertainty quantification, etc.) are conducted. The maximum level of experimental variability observed is 0.27% for the second free-free bending mode.

Since this value corresponds to one standard deviation σ, the $\pm 3\sigma$ (two-sided) bounds are equal to 1.62% variability. These $\pm 3\sigma$ bounds are adopted to characterize the experimental variability since they account for 98% of the total probability mass, assuming a Gaussian probability law. This choice yields a fair comparison with the bounds of total solution uncertainty quantified in section 6.2, where the mesh size is chosen such that the numerical uncertainty is similar to this 1.62% variability for predictions of the resonant frequencies.

2.6. Solution Verification and Quantification of Numerical Uncertainty

This section starts by describing attributes of the FE model developed to simulate bending deformation shapes of the CX-100 wind turbine blade. The main assumption that enables fast-running calculations, namely, the use of homogenized material properties, is proposed. Solution verification is carried out, first, to assess the numerical performance of the model and, second, to choose a mesh resolution that results in an appropriate level of numerical uncertainty.

Finally, the behavior of the NuMAD pre-processing software is revisited to assure that its mesh sensitivities do not produce adverse consequences for the FE model developed.

2.6.1 Development of a Simplified Model of the CX-100 Blade

The model of the CX-100 blade is developed with the NuMAD pre-processor and imported into the ANSYS software. The blade is nine-meters long and its geometry is represented in the model using design specifications with as few simplifications as possible. Figure 2.10 provides a comparison of the simplified FE model used in this study to a high-fidelity FE model, which can more accurately capture the taper of materials used to define the root section.

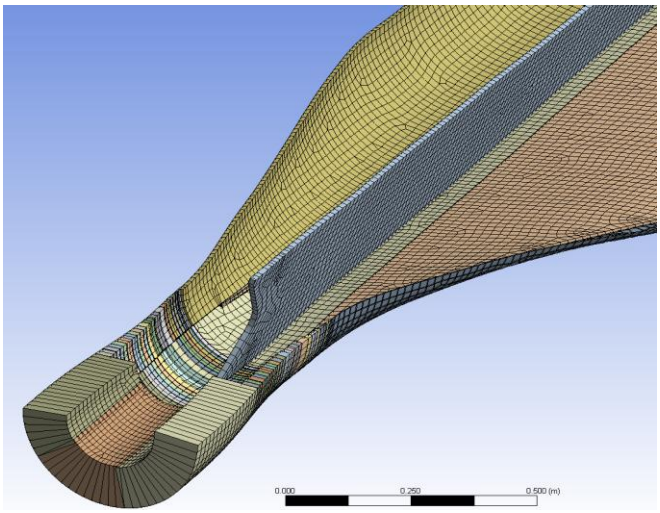

Figure 2.10: High-fidelity CX-100 ANSYS model with detailed cross-sectional modeling.

The model used in this study is achieved by segmenting the geometry of the blade into a small number of sections and defining smeared properties for each section. This is done, in contrast to the type of modeling provided in Figure 2.10, because a high-fidelity model is computationally too expensive to lend itself to the parametric studies that we wish to pursue. It is emphasized that the number and definition of smeared sections is considered to be a model-form choice, as opposed to a discretization, which implies that the "convergence" of the vibration

response as a function of the number of sections is not currently studied. The ability of the simplified model to predict the bending modes of vibration with reasonable accuracy is discussed in Reference 7.

Six sections are defined: the shear web, root, spar cap, trailing edge, leading edge with balsa, and leading edge without balsa. Figure 2.11 represents five of these sections, while the interior shear web is illustrated in Figure 2.12. To reflect the tapering of the edges in the real-life structure, the trailing edge and leading edge of the blade are further subdivided into three sub-sections of differing stiffness coefficients.

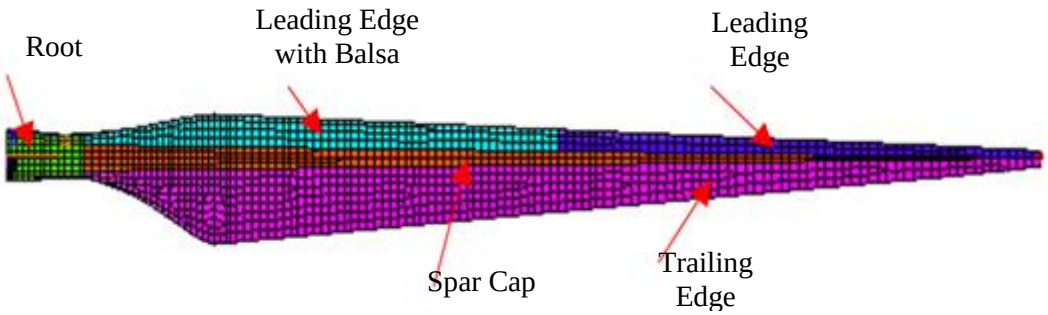

Figure 2.11: Illustration of the ANSYS model showing different sections of the blade.

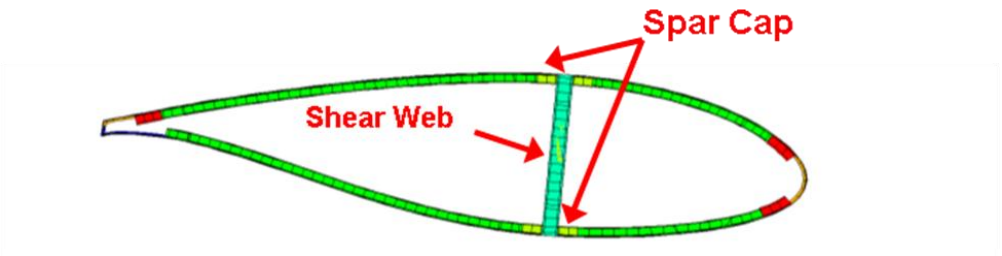

Figure 2.12: Illustration of the ANSYS model's shear web located inside the blade.

Within each section, an isotropic material is defined by assuming smeared cross-sectional properties. The validity of this simplification is explored in Reference 7 by performing sensitivity

analysis, uncertainty quantification, and comparisons between model predictions and physical measurements. The rule of mixtures is utilized to homogenize the composite cross sections.[25] Based upon the structure of composites, the rule of mixtures blends together the differing material properties and estimates the material property of an equivalent isotropic material.

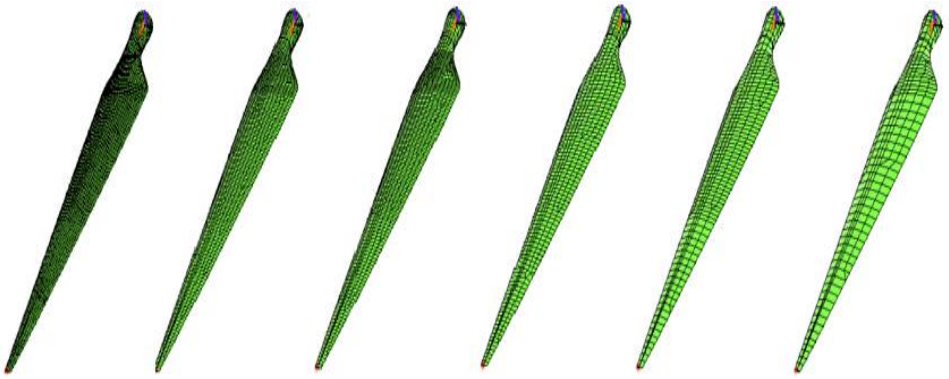

Figure 2.13: Six meshes used to assess the asymptotic convergence of vibration modes.

One important aspect of performing numerical simulations is to assess if the equations of motion, or conservation laws, are discretized with enough resolution to produce "good-quality" numerical solutions. A mesh convergence study is performed to verify the performance of the ANSYS software, as applied to the CX-100 blade model, and determine an appropriate level of mesh resolution for the calculations. Our decision criteria are to, first, reach a level of numerical uncertainty that is comparable to, or smaller than, the overall experimental variability, while also being capable to run a linear, modal extraction on a PC platform in fewer than 60 seconds.

2.6.2 Mesh Refinement and Quantification of Truncation Error

After having scripted and automated the execution of the FE model, over twenty meshes are analyzed to predict the low-order resonant modes. Figure 2.13 illustrates six of these calculations, where the figures from left to right show progressively lower levels of mesh resolution. Figure 2.14 reports the values of predicted resonant frequencies as a function of mesh

size. The three natural frequencies shown are the three modes targeted: the first flap-wise bending (mode 1), second flap-wise bending (mode 3), and third flap-wise bending (mode 4). It is clear from the figure that these resonant frequencies exhibit a satisfactory degree of convergence as the number of elements of the discretization increases.

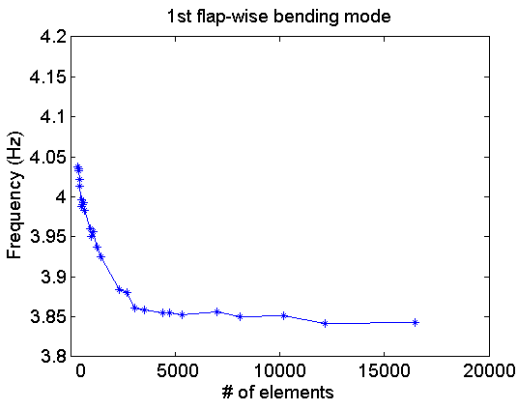

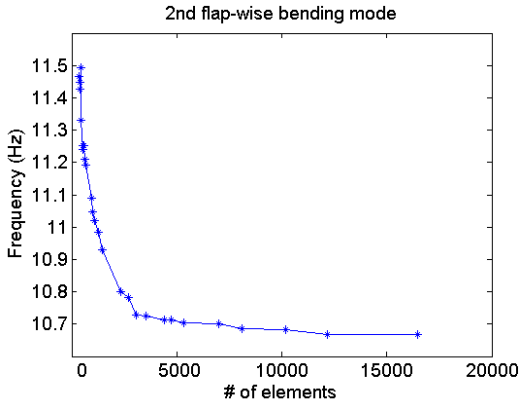

2.14-a) First flap-wise bending frequency. **2.14-b) Second flap-wise bending frequency.**

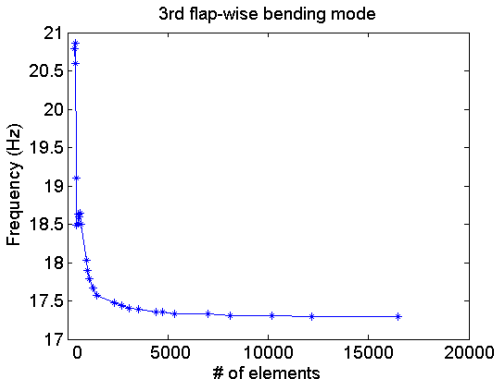

2.14-c) Third flap-wise bending frequency.

Figure 2.14: Convergence of resonant frequencies as a function of mesh resolution.

The numerical uncertainty due to truncation error, that is, lack of resolution in the calculation, is bounded as explained in section 3 for the three bending frequencies of interest. These upper bounds are defined as:

$$\left|\frac{\omega^{*}-\omega(\Delta x)}{\omega(\Delta x)}\right| \le U(\Delta x), \tag{12}$$

where ω* is the best-possible estimation of the "exact-but-unknown" frequency while ω(Δx) is the approximation obtained by running the calculation at mesh resolution Δx. The uncertainty bound U(Δx) is related to the GCI through the introduction of a safety factor F_S, as illustrated in equations (8-9). When the solution ω* is estimated, for example, through the method of Richardson's extrapolation, it is possible to examine the solution error and assess asymptotic convergence.[12] This extrapolation scheme leads to an approximation obtained simply as:

$$\omega^{*} \approx \omega(\Delta x) + \frac{\omega(\Delta x) - \omega(R \cdot \Delta x)}{R^{p} - 1}. \tag{13}$$

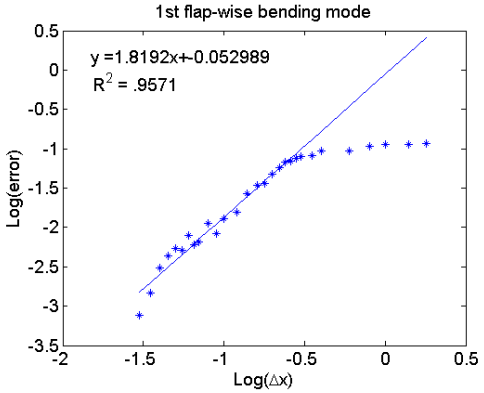

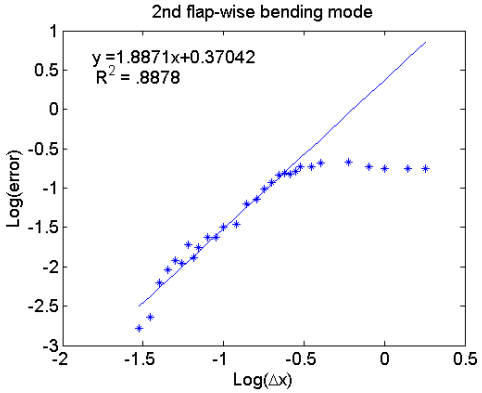

2.15-a) First flap-wise bending frequency. **2.15-b) Second flap-wise bending frequency.**

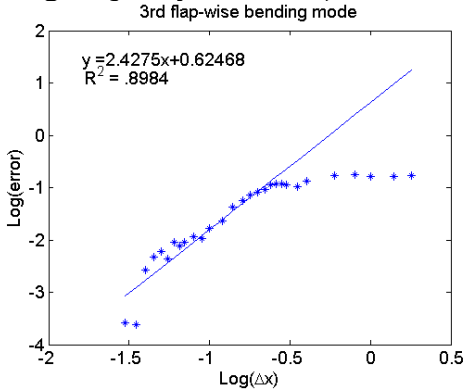

2.15-c) Third flap-wise bending frequency.

Figure 2.15: Asymptotic convergence of frequencies as a function of mesh resolution.

Figure 2.15 illustrates the behavior of solution error $|\omega^* - \omega(\Delta x)|$ as a function of mesh size Δx for the same three modal frequencies as those of Figure 2.14, and where the exact solution is approximated by applying equation (13) to the two finest levels of mesh resolution.

Convergence is observed even though five to seven models analyzed with the coarsest levels of resolution are located in a non-asymptotic region where refining the mesh does not necessarily decrease the truncation error. These under-resolved calculations are disregarded for the purpose of best-fitting the model of truncation error $|\omega^* - \omega(\Delta x)| = \beta \cdot \Delta x^p$, whose definition applies only within the asymptotic regime of convergence. The log-log scale of Figure 2.15 indicates that convergence is nearly second-order for the models located in the asymptotic regime. This is confirmed by a quantitative analysis that best-fits the two unknowns (β; p) of simple power-law equations $|\omega^* - \omega(\Delta x)| = \beta \cdot \Delta x^p$ to the error data of Figure 2.15. The observed rates-of-convergence are equal to p = 1.82 for the first flap-wise bending mode, p = 1.89 for the second flap-wise bending mode, and p = 2.43 for the third flap-wise bending mode. It implies that second-order accuracy is achieved for the modal analysis.

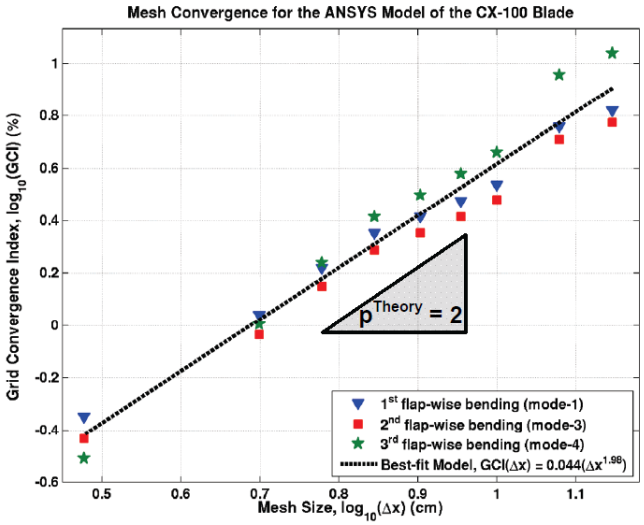

Figure 2.16: Values of the GCI for the first three flap-wise bending modes.

Figure 2.16 shows the GCI obtained with a safety factor of $F_S = 3$. Three bending frequencies are denoted by different symbols. The dashed line illustrates the goodness-of-fit obtained with a simple power-law equation $GCI(\Delta x) = \beta \cdot \Delta x^p$ for the average GCI. Best-fitted coefficients equal to $\beta = 0.044$ and $p = 1.98$ lead to, again, strong evidence of second-order accuracy. Based on these observations, the hypothesis that the finest levels of mesh resolution provide solutions within the regime of asymptotic convergence cannot be rejected.

So far, the mesh refinement results have been analyzed to assess the performance of the FE software. While observing second-order accuracy is reassuring, it may not be of great practical interest given that the code verification activities of section 4 have already concluded to the lack of significant implementation issue for the intended purpose. It is, however, a first step needed to support the quantification of solution uncertainty. What is more valuable to the practicing engineer is to select an appropriate mesh size to pursue the parameter studies of Reference 7.

Often, the strategy to select a mesh size is *"run as fine a mesh as computationally feasible."* This approach may lead to a waste of resources when the resolution employed is too fine. It is also unsatisfactory in the context of V&V because this rationale does not take into account the intended purpose of the numerical simulation, desired level of prediction accuracy, and overall reproducibility of experimental testing (whenever available). In this work, an alternative strategy is proposed based on the overall level of experimental variability. While challenging the conventional separation between verification and test-analysis correlation, our proposal offers the advantage of avoiding to select a mesh size in a "vaccum."

Our guiding principle is to use a mesh discretization that provides an overall level of numerical uncertainty comparable to the experimental variability. The rationale is that there is no

reason to provide significantly more prediction accuracy than the level with which the response can be measured when experimental testing is replicated.

Table 2.2: GCI for predictions of the three bending modes of interest.

Mesh Size, Δx	1st Mode GCI	3rd Mode GCI	4th Mode GCI	Mean GCI
5.0 cm	0.77%	0.61%	0.67%	0.68%
6.0 cm	1.11%	0.94%	1.16%	1.07%
7.0 cm	1.50%	1.29%	1.73%	1.51%
8.0 cm	*1.73%*	*1.50%*	*2.10%*	***1.78%***
9.0 cm	1.99%	1.73%	2.53%	2.08%
10.0 cm	2.30%	2.01%	3.06%	2.46%

Legend: These calculations are based on a constant safety factor, $F_S = 2$, see equation (8).

Table 2.2 lists the GCI of equation (8) obtained with a safety factor of $F_S = 2$. This choice is made, instead of $F_S = 3$ used in Figure 2.16, by analogy to the ±3σ bounds of experimental variability of section 5 that are two-sided. Our contention is to select a mesh size that leads to a numerical uncertainty similar to the 1.62% level of experimental variability. Another constraint imposed by the parameter studies is to minimize time-to-solution. The 7-cm mesh, while it satisfies the first criterion, does not provide modal solutions in fewer than 60 seconds on our PC computing platform (Intel single-core, 2-GHz processor, 4 GB memory, Windows 7 operating system). It is decided that the next level of mesh size provides the best **trade-off** between the two competing constraints. The solution uncertainty obtained at Δx = 8 cm is the 4th row highlighted in color ***red*** in Table 2.2. The 8-cm mesh calculates modal solutions in fewer than 60 seconds while yielding 1.78% solution uncertainty, on average, which meets the objective of comparing favorably to the ±3σ bound of 1.62% variability assessed from Table 2.1.

To pursue the parameter studies of Reference 7, the decision is made to "freeze" the resolution at Δx = 8 cm. It gives a FE model with 3,070 elements from which the resonant modes can be extracted in 60 seconds, approximately.

2.6.3 Mesh Sensitivity Introduced by the Pre-processing Software NuMAD

Through the course of the above analyses, several other variables are altered to explore their potential effects upon the truncation error. Notably, it is attempted to explore different meshes by overriding the default meshing method implemented by the pre-processor NuMAD and assign a coarser or finer mesh to the shear web than the resolution used for the other structural components of the CX-100 model. This study involves creating and running a separate post-processor to modify the output generated by the NuMAD software.

Figure 2.17 illustrates qualitative results for a bending stress analysis and a torsional shear stress analysis, using three different options of shear web meshing—a coarse, medium, and fine mesh (as compared to the other components of the model). The values of stress are depicted as a function of mesh size for the other, non-shear-web elements. Our hypothesis is that there is no reason to observe any significant cross-sensitivity between the mesh size used to discretize the shear web and the mesh size used to discretize the other components.

The results yield some surprising findings: in neither case is the effect of the mesh size of the shear web on the resulting stress monotonic. The predictions obtained with the medium mesh size for the shear web are, in each case, extreme, when they instead would be expected to lie between predictions obtained with the coarser and finer levels of resolutions. The calculations exhibit the expected behavior at any given level of shear web resolution, that is, moving along one of the datasets as $\Delta x \rightarrow 0$. What is unexpected is to observe the extent to which predictions are sensitive to the combination of mesh sizes for the shear web and other components.

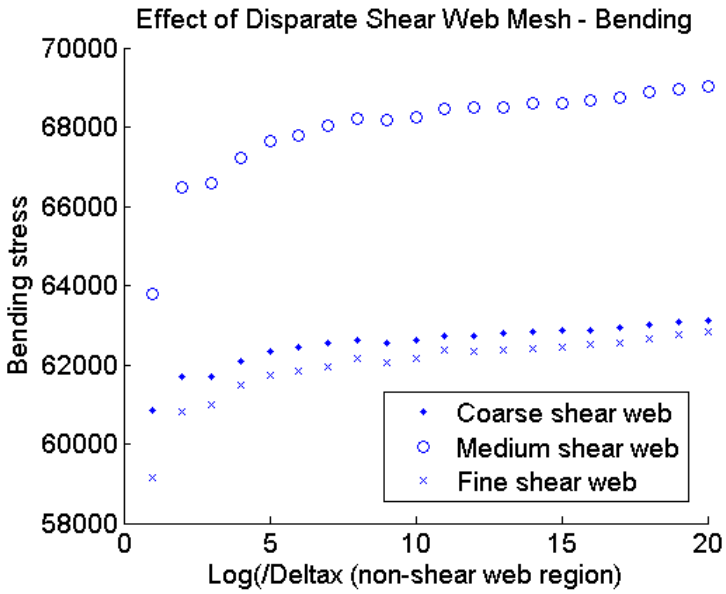

17-a) Stress-in-bending test problem.

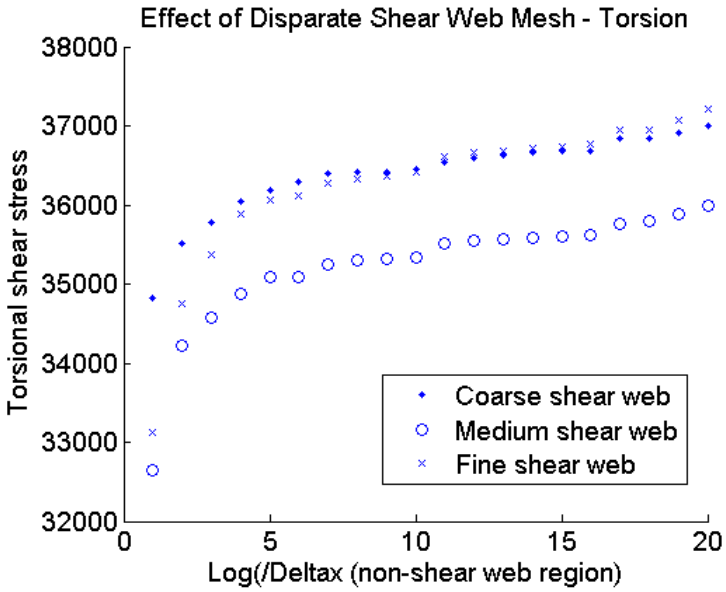

17-b) Stress-in-torsion (shear) test problem.

Figure 2.17: Stress values for different meshing options of the shear web.

No explanation for this effect is readily apparent. These observations are nevertheless made in the interest of full disclosure of the results obtained. For all results other than those

discussed in this section, FE models are generated from the default, homogeneous mesh option of the pre-processor. The mesh cross-sensitivity observed is therefore not believed to be detrimental to the quality of our numerical predictions.

2.7. Conclusion

This publication discusses the development of a finite element model for the CX-100 wind turbine blade and overviews some of the analysis procedures implemented to verify the code, quantify the overall level of solution uncertainty due to truncation error, and compare it to experimental variability. These are some of the activities typically deployed in a V&V study. Other activities that include sensitivity analysis, the propagation of parametric uncertainty from inputs of the model to its predictions, and the calibration of model parameters are addressed in a companion paper for the same application.[7]

To rigorously quantify numerical uncertainty in the absence of an exact solution to the equations of motion, or conservation laws, being solved, an upper bound of solution error is derived. An analogy is made with the well-known Grid Convergence Index when a specific value of its safety factor is implemented. Another novelty of this publication is to propose a criterion based, on one hand, on time-to-solution and, on the other hand, on a comparison to experimental variability to select an appropriate level of mesh resolution for the calculations.

Our investigation concludes that the analysis code is adequate to model the low-order bending and torsion dynamics of interest, based mainly on the shell-281 finite element of the ANSYS software. Comprehensive mesh refinement studies are performed to assess not only the regime of asymptotic convergence of predictions, but also to select a mesh size that yields a numerical uncertainty that is suitable based upon the experimental context. The experimental variability observed when performing modal tests of the CX-100 blade with different support setups is quantified and used to guide the selection of mesh resolution. Based on the findings

discussed in this paper, the finite element model is deemed verified and ready for further validation and uncertainty quantification studies discussed in Reference 7.

References

1. U.S. Department of Energy. 20% Wind Energy by 2030: Increasing Wind Energy's Contribution to U.S. Electricity Supply. *Report DOE/GO-102008-2567*, Washington, D.C., 2008.

2. Hahn B. Durstewitz M. Rohrig K. Reliability of Wind Turbines. Wind Energy: Proceedings of the Euromech Colloquium. Springer-Verlag, Berlin, 2007.

3. Walford CA. Wind Turbine Reliability: Understanding and Minimizing Wind Turbine Operation and Maintenance Costs. Sandia Report, SAND2006-1100, Sandia National Laboratories, Albuquerque, NM, 2006.

4. Ashwill TD. Blade Technology innovations for Utility-Scale Turbines. AWEA Global Windpower. Pittsburg, PA, 2006.

5. Ciang CC. Lee JR. Bang HJ. Structural Health Monitoring for a Wind Turbine System: a Review of Damage Detection Methods. *Measurement Science and Technology* 2008; **19**: 1-20.

6. Paquette JA. Veers PS. Increased Strength in Wind Turbine Blades through Innovative Structural Design. *European Wind Energy Conference Proceedings*, Milan, Italy, 2007.

7. Van Buren KL. Mollineaux MG. Hemez FM. Simulating the Dynamics of Wind Turbine Blades: Part II, Uncertainty Quantification and Model Validation. *13th AIAA Non-deterministic Approaches Conference*, Denver, CO, April 4-7, 2010. (Also, Los Alamos report LA-UR-10-5605.)

8. Laird DL. NuMAD User's Manual. Sandia Report, SAND2001-2375, Sandia National Laboratories, Albuquerque, NM, 2001.

9. Berry D. Design of 9-Meter Carbon-Fiberglass Prototype Blades: CX-100 and TX-100. Sandia Report, SAND2007-0201, Sandia National Laboratories, Albuquerque, NM, 2007.

10. Laird DL. Montoya FC. Malcolm D. Finite Element Modeling of Wind Turbine Blades. *43rd AIAA Aerospace Sciences Meeting and Exhibit*, 2005.

11. Hemez FM. Uncertainty Quantification and the Verification and Validation of Computational Models. *Damage Prognosis: for Aerospace, Civil and Mechanical Systems*. Ed. Inman DJ, John Wiley and Sons, West Sussex, England, 2005.

12. Roache PJ. *Verification and Validation in Computational Science and Engineering*. Hermosa Publishers: Albuquerque, NM, 1998.

13. Griffith DT. Carne TG. Paquette JA. Modal Testing for Validation of Blade Models. *Wind Engineering* 2008; **32**: 91-102.

14. Veers PS. Laird DL. Carne TG. Sagartz MJ. Estimation of Uncertain Material Parameters Using Modal Test Data. *ASME Wind Energy Symposium, 36th AIAA Aerospace Sciences Meeting*, Reno, NV, January 12-15,1998.

15. Griffith DT. Hunter PS. Kelton DW. Carne TG. Paquette JA. Boundary Condition Considerations for Validation of Wind Turbine Blade Structural Models. *Society for Experimental Mechanics Annual Conference & Exposition on Experimental and Applied Mechanics*, Albuquerque, NM, June 2009.

16. Griffith DT. Casias M. Smith G. Paquette J. Simmermacher TW. Experimental Uncertainty Quantification of a Class of Wind Turbine Blades. *24th International Modal Analysis Conference*, February 2006. (Also, Sandia report SAND2005-6624C.)

17. Griffith DT. Carne TG. Experimental Uncertainty Quantification of Modal Test Data. *25th International Modal Analysis Conference*, Orlando, FL, February 2007.

18. Roache PJ. Perspective: A Method for Uniform Reporting of Grid Refinement Studies. *ASME Journal of Fluids Engineering* 1994; **16**: 405-413.

19. Lax PD. Richtmyer RD. Survey of the Stability of Linear Finite Difference Equations *Communications in Pure and Applied Mathematics* 1956; **9**: 267-293.

20. Hirt CW. Heuristic Stability Theory for Finite Difference Equations *Journal of Computational Physics* 1968; **2**: 339-355.

21. Warming RF. Hyett BJ. The Modified Equation Approach to the Stability and Accuracy Analysis of Finite Difference Methods. *Journal of Computational Physics* 1974; **14**: 159-179.

22. Hemez FM. Functional Data Analysis of Solution Convergence. Los Alamos Report, LA-UR-07-5758, Los Alamos National Laboratory, Los Alamos, NM, August 2007.

23. Blevins DR. *Formulas for Natural Frequency and Mode Shapes.* Krieger Publishing Company: Malabar, FL, 1993.

24. Deines K. Marinone T. Schultz R. Farinholt K. Park G. Modal Analysis and SHM Investigation of CX-100 Wind Turbine Blade. *29th International Modal Analysis Conference*, Jacksonville, FL, 2011.

25. Askeland D. Fulay P. Wright W. *The Science and Engineering of Materials* CL-Engineering: Stamford, CT, 2010.

CHAPTER THREE

SIMULATING THE DYNAMICS OF WIND TURBINE BLADES: PART II, MODEL VALIDATION AND UNCERTAINTY QUANTIFICATION

3.1. Introduction

Wind energy research is being pursued in the United States as a viable alternative to provide a major amount of installed electrical power, as part of the "20% by 2030" initiative by the U.S. Department of Energy.[1] However, for wind energy to become a mainstay of energy needs, its cost must first be reduced drastically. The blades are responsible for only 10-15% of the cost of the wind turbine system,[2] however, damage to the blades can result in rotor instability that leads to damage of the entire wind turbine system.[3,4] To efficiently design for the next generation of wind turbines, it is crucial to understand the dynamics of wind turbine blades, that capture all of the kinetic energy transported by the surrounding flow of wind, and improve the reliability of power generation from wind plants.[5] Better understanding of the wind turbine blades is essential, since the blades carry most of the structural loads that get imparted on the entire wind turbine. Better models would make more accurate predictions of performance, which would mitigate the operation and maintenance expenses associated with wind energy. These expenses currently start as low as $5 per 10+6 Watt-hour (MWH), but climb to costs as high as $20 per MWH over a 20 year evolution of service.[6]

Modeling and Simulation (M&S) offers a quicker, safer, and more economical alternative to the conventional cycle of designing, prototyping, and testing to study wind turbine blade behavior.[7] The versatility of modeling can be used to predict the response to many complex load cases,[8] whereas only idealized loads can usually be implemented in full-scale experiments.[9] In addition, parametric studies of damage to wind turbine blades can be investigated in an

economical way through M&S, whereas the feasibility of such experimental campaigns would be limited due to the cost and safety implications.

Due to demands for faster turn-around times and the, sometimes, limited access to computing resources, there is a growing need to develop simplified, "engineering" models that can keep parametric and calibration studies to a manageable size.[10] It is also expensive, both in terms of memory management and time-to-solution, to couple a Computational Fluid Dynamics (CFD) code to flexible dynamics models of the blades and, potentially, models of structural damage, to develop credible simulations of entire wind plants.[11] One approach to reduce this computational burden is to simplify the flexible dynamics of the wind turbine blade to speed-up the calculations without, to the extent possible, sacrificing the prediction accuracy. The study presented in this manuscript, together with a companion publication, demonstrate the application of Verification and Validation (V&V) technology to achieve these goals.[12]

Our objective is to develop a structural model that, while simplified as much as possible, still captures the dynamics of interest. The V&V activities deployed in the companion manuscript (Reference 12) and this manuscript support essential steps of the model development process to guarantee that the simplifications introduced are justified for the intended purpose. V&V also serves the purpose of quantifying the experimental variability and numerical uncertainty (discussed in Reference 12), and the model parameter uncertainty (discussed in this manuscript).

As explained in Reference 12, the structure investigated is the nine-meter, all-composite CX-100 blade designed at the Sandia National Laboratories (SNL). The Finite Element (FE) software is ANSYS version 12.1. The simplified model is developed based on an as-accurate-as-possible description of the geometry obtained from design specifications. However, implementation of the materials relies on a strong assumption: the cross-sectional areas for the blade are modeled as smeared and isotropic material properties instead of modeling the multiple

composite layers embedded in the epoxy matrix. The overarching goal of this effort is to demonstrate the extent to which V&V can be integrated to the model development of a simplified yet validated FE model which delivers an acceptable level of predictive capability. Validated models that satisfy given time-to-solution requirements for the application of interest provide a competitive advantage.

Developing a predictive capability motivates the need to quantify the uncertainty introduced by assumptions imposed during the development of a FE model. Understanding the approximate behavior of a model renders it imperative to take into consideration *all* sources of uncertainty, as discussed in section 2. Section 3 provides a cursory overview of the FE model of the CX-100 blade. (See Reference 12 for an in-depth discussion.) Section 4 discusses three V&V activities: the propagation of uncertainty from input parameters of the FE model to output predictions, sensitivity analysis and effect screening, and model calibration. These investigations are applied to low-order resonant frequencies of the blade according to a two-step approach. The response of the free-free model is evaluated, followed by the fixed-free model, in an effort to decouple our understanding of material properties from that of model parameters that represent the boundary condition compliance. Section 5 presents an independent validation assessment based on the ability of the calibrated model to correlate predicted and measured mode shape deflections. The implications and limitations of this study are discussed in Section 6.

3.2. Review of Pertinent Literature

Assumptions and simplifications are regularly imposed in numerical models, which are emphasized to only be able to provide an approximation of reality. For example, beam property extraction methods have been developed, which require low computational cost and can be used for fast-running calculations.[13] However, one study attempting to model a wind turbine system found that neglecting the effect of damping produced predictions with low goodness-of-fit to the

experimental data.[14] This study, along with similar observations from other disciplines, suggest that not accounting for the uncertainty introduced by the simplifications and modeling assumptions can have a degrading effect on the quality of model predictions.

Another consideration is the relationship between goodness-of-fit to test data and the predictive capability of a model. It can be shown that fidelity-to-data, robustness to assumptions, and predictive capability are antagonistic attributes of any family of models.[15] This can be described using the case of over-fitting, which happens when a model produces accurate predictions for configurations to which it was calibrated. But this may come at the cost of reducing its predictive capability, that is, the accuracy of its predictions when attempting to simulate other, non-tested configurations. Understanding these trade-offs is important for the development of robust CFD and FE models because it is important that models are robust to sources of variability, such as the significant variability between wind turbine blades that will result in different levels of structural response.[16]

It is also important to account for the uncertainty associated with experimental procedures. The vibration testing of an article in a free-free configuration can often be affected by the positioning of the straps, mass loading of the accelerometers, and orientation of the test specimen.[16,17] The free-free boundary condition is, on the other hand, trivial to simulate numerically. When free-free is not an option, proper modeling of the boundary condition becomes necessary to ensure that the predictions of structural response can be compared to measurements. Modeling a fixed-free boundary condition is a possibility, as long as the non-ideal compliance of the attachment setup can be accounted for, if it is believed important to do so. An unknown, boundary compliance can also significantly influence what is observed during a vibration test. To mitigate the uncertainty associated with a fixed-boundary compliance, studies originating at SNL propose a new setup for the modal analysis of wind turbine blades, in which a

nine-meter blade is mounted vertically on a seismic mass and airbags system.[10,18] This type of boundary condition is designed so that its characteristics would be well-characterized and modeled accurately in the simulation of the structural model. The setup assures that the fixity of the blade to the seismic mass is rigid, and that there is a soft boundary condition when placed on the airbags, which can be characterized by stiffness properties. In a further investigation of boundary condition effects, the experimental modal analysis of a stationary wind turbine system is performed.[19] Blade and tower responses to impact hammer testing are characterized. The mode shapes identified during these vibration tests demonstrate that there is significant coupling between the different blades and tower, confirming that the tower of a wind turbine system does not behave as a rigid body.

Recently, the development of FE models has gained acceptance for routine use in the study of wind turbine blades. Another common practice is to perform calibration against experimental data as an integral part of model development. Reference 20 provides an early attempt to utilize FE modeling in the design and analysis of wind turbine blades using shell and solid elements. The study researched the optimal design of a two and a half-meter long blade, and experimental data from fabricated blades were analyzed to validate predictions of the FE model. Another early attempt used free-free modal data collected from a four-meter section of a blade to calibrate a FE model.[21] Accuracy was improved by collecting additional measurements of the geometry of the blade and increasing the resolution of the simulation (higher mesh density). It was found that, by using these approaches, the number of assumptions needed to model the blade section could be reduced. Other studies have since investigated the use of M&S to study the behavior of wind turbine blades, owing to the versatility of numerical models.[22,23] The current study builds on previous research efforts to model wind turbine blades, and places an emphasis on the use of V&V activities to establish the predictive capability of numerical simulations.

3.3. Development of the Simplified Finite Element Model

This section provides a cursory overview of the FE model of the CX-100 blade. The reader is referred to Reference 12 for details about the model development and quantification of solution (or numerical) uncertainty. The brief explanation provided below is useful to better understand the uncertainty quantification, sensitivity analysis, and calibration steps discussed in section 4.

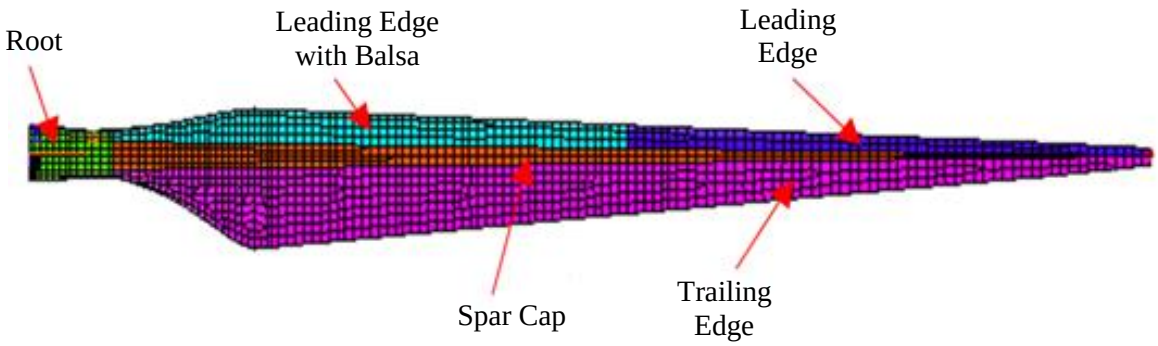

Figure 3.1: Illustration of the ANSYS model showing different sections of the blade.

The model of the CX-100 wind turbine blade is developed with the NuMAD pre-processor and imported into the ANSYS software. The blade is nine meters long and its geometry is imported from another, high-fidelity FE model with as few simplifications as possible. Solution verification is performed, that utilizes the results of a mesh refinement study, to quantify the overall level of numerical uncertainty due to mesh discretization. A discretization based on an element size of $\Delta x = 8$ cm is deemed appropriate because it provides an overall solution uncertainty of 1.78%. This is comparable to the maximum level of experimental variability obtained by replicating the modal tests, where the $\pm 3\sigma$ bounds of uncertainty are estimated to be 1.62%. The other criterion adopted to select the level of resolution is to be able to perform a modal extraction in less than 60 seconds on a PC-based computing platform (Intel single-core, 2-GHz processor, 4 GB memory, Windows 7 operating system), which is a constraint that needs to

be met in order to make parametric studies feasible. (See Reference 12 for details.) The mesh arrived at counts 3,070 elements and computes the modal solution in less than 60 seconds.

To simplify the parameterization of the model, only six independent sections are defined, compared to high-fidelity models that require hundreds of sections. Most of them are illustrated in Figure 3.1. They are the shear web, root, spar cap, trailing edge, leading edge with balsa, and leading edge without balsa. The shear web runs along most of the length of the blade and it is not shown in the figure because of its location on the inside. Within each one of these sections, an isotropic material is defined with smeared cross-sectional properties. The validity of this assumption is explored in section 4 to assess the credibility of the simulation.

Table 3.1: System identification of the CX-100 blade with free-free modal testing.

Type of Mode	Mean Statistic	Standard Deviation	Variability[(1)]
First flap-wise bending	7.617 Hertz	0.004 Hertz	0.06%
Second flap-wise bending	20.167 Hertz	0.055 Hertz	0.27%
Third flap-wise bending	32.256 Hertz	0.051 Hertz	0.16%

Legend: [(1)] The coefficient of variance in the last column is defined as the standard deviation (column-3) divided by the mean (column-2). It is based on 27 replicates for free-free vibration testing.

Table 3.2: System identification of the CX-100 blade with fixed-free modal testing.

Type of Mode	Mean Statistic	Standard Deviation	Variability[(1)]
First flap-wise bending	3.221 Hertz	0.008 Hertz	0.24%
Second flap-wise bending	8.824 Hertz	0.011 Hertz	0.12%
Third flap-wise bending	19.204 Hertz	0.020 Hertz	0.11%

Legend: [(1)] The coefficient of variance in the last column is defined as the standard deviation (column-3) divided by the mean (column-2). It is based on 27 replicates for fixed-free vibration testing.

Modal testing of the CX-100 wind turbine blade is carried out under free-free and fixed-free boundary conditions at the Los Alamos National Laboratory (LANL).[12,17] Roving impact hammer tests are performed to amass modal data at three locations with uniaxial accelerometers. A linear average is used with five repeats and a 150-Hertz sampling frequency. The acceleration response is measured for eleven seconds, during which the response of the blade is attenuated.

This procedure negates the use of a window function. The levels of experimental variability are quantified and listed in Tables 3.1 and 3.2 for the free-free and fixed-free boundary conditions. The observed variability is attributed to potential calibration errors, operator-to-operator variability, and the inability to identically repeat the experiments on the same test specimen of the CX-100 blade. The fact that it does not account for any specimen-to-specimen or test setup variability explains the overall low levels of uncertainty observed during this campaign of vibration testing.

3.4. Propagation of Uncertainty, Sensitivity Analysis, and Calibration

Section 4 presents results of the V&V study. The discussion starts by formulating questions about specific aspects of the predictive capability being developed. The main contribution of this publication is to demonstrate how V&V activities, such as mesh refinement or effect screening, can be integrated to model development to start answering these questions. Simulations are analyzed, first, for free-free vibrations of the CX-100 blade (sections 4.2 and 4.3). The fixed-free configuration is analyzed next to decouple the parameterization of the boundary condition from the description of homogenized material properties in the model (sections 4.4 and 4.5).

3.4.1 Specific Questions about the Predictive Capability

We would like to answer the following four questions regarding specific aspects of the predictive capability provided by the fast-running, "engineering" model of the CX-100 blade:

Question-A: what is an appropriate level of mesh resolution for the calculations?

Question-B: what are the mechanisms that most influence the variability of predictions?

Question-C: can measurements be used to reduce parametric uncertainty in the model?

Question-D: does the model provide accurate-enough predictions of mode shapes?

Question-A is answered in Reference 12 where it is shown how a mesh refinement study can be combined to an upper-bound estimate of solution uncertainty. It is found, as noted in section 3, that a discretization of $\Delta x = 8$ cm leads to an overall solution uncertainty of 1.78%. Running the modal analysis at this level of resolution provides a time-to-solution of 60 seconds, approximately, which is fast enough to enable parametric studies with thousands of runs.

Question-B promotes understanding of what controls the prediction variability. By learning which parameters are most influential to explain how the predictions change, one can control them in order to reduce the prediction uncertainty. It is equally important to learn which parameters do not control the prediction uncertainty because attempting to better control a non-influential effect would be both inefficient and a waste of important resources. The prediction variability observed from a design-of-experiments is decomposed into separate effects to answer Question-B.

Recall that the model is parameterized into only six sections and that each section is described by homogenized material properties. The resulting idealization is anything but high-fidelity since the real structure involves a multi-layered composite material. Our point-of-view is that there is no such thing as "true" values of these material properties. What becomes essential is to reduce as much as possible the initially large lack-of-knowledge of these fictitious parameters, which is the subject of Question-C. The vibration measurements are used to search for values that, while they remain uncertain, lead to predictions that better match the experimental data.

Finally, Question-D exemplifies the validation assessment. While the propagation of uncertainty, sensitivity analysis, and calibration are applied to frequency predictions, validity of the simplified model is assessed using mode shape predictions. The rationale is to investigate predictions that have not been exploited for calibration, hence, promoting the use of separate datasets between development and validation of the model. Another reason for this choice is that

accurate predictions of mode shape deflections are important to couple the structural dynamics and CFD-based simulation of flow around the turbine. It may, arguably, be even more important than predicting the resonant frequencies accurately. Question-D is answered through conventional test-analysis correlation.

3.4.2 Propagation of Uncertainty and Sensitivity Analysis of the Free-free Configuration

As noted above, it is important to assess what controls the prediction variability. Understanding which parameters, or groups of parameters, are most influential allows for the elimination of the insensitive ones. It promotes computational savings and a more efficient calibration.

After having studied mesh discretization in Reference 12, the next dominant lack-of-knowledge in the problem comes from the idealization of the composite material as uniform and isotropic. Material properties (modulus of elasticity, E, and density, ρ) are approximated using the rule of mixtures for composites, which provides ranges $[E_{Min}; E_{Max}]$ and $[\rho_{Min}; \rho_{Max}]$ for each parameter.[24] To simulate the free-free vibrations, the model is parameterized using a total of twelve parameters that are the modulus of elasticity (E) and density (ρ) for the six sections of the blade.

The first step of the analysis is to propagate uncertainty from the twelve parameters to resonant frequency predictions. A two-level, full-factorial Design-Of-Experiments (DOE) is used, whereby all combinations of lower and upper bounds for the twelve parameters are executed. The design results in a total of 2^{12} = 4,096 evaluations of the FE model. Figure 3.2 compares predictions from these 4,096 runs to the mean statistic of measured frequencies for the first mode. The fact that measurements fall within the range of frequencies predicted by the DOE is confirmation that the model captures the first flap-wise bending reasonably well. However, the

prediction uncertainty obtained by propagating the initial ranges of twelve parameters is quite significant relative to the experimental variability. (Recall, $\sigma = 0.004$ Hertz only from Table 3.1.)

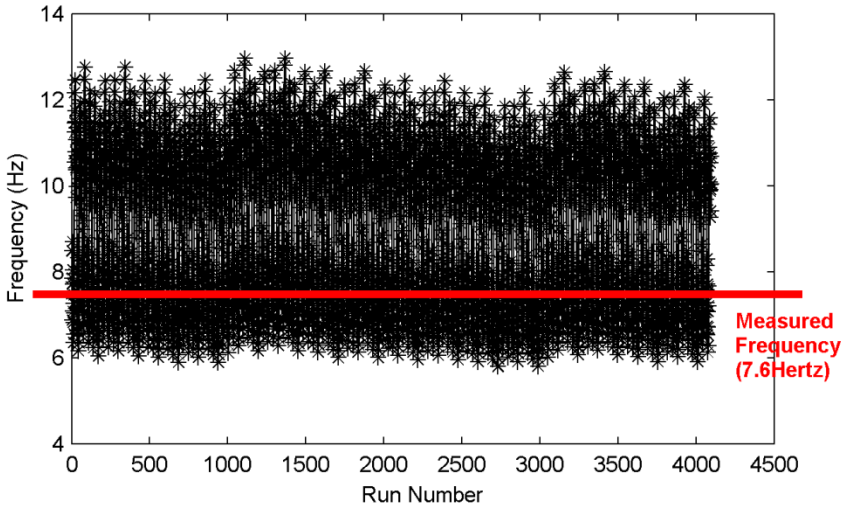

Figure 3.2: Comparison of first-mode simulation uncertainty and measured frequency.

The second step is to understand which parameters, or combinations of parameters cause the large uncertainty illustrated in Figure 3.2. Our hypothesis is that only a few parameters, out of the twelve considered, are statistically significant to explain how the predictions vary. Two additional DOE are analyzed to confirm, or refute, this hypothesis. A Latin Hypercube (LHS) sample with a 1,000 runs is analyzed first to identify the potentially non-significant parameters.[25] From an Analysis-of-Variance (ANOVA), the number of significant parameters is reduced from twelve to eight.[26] This first design is supplemented by the analysis of a two-level, full-factorial DOE that requires another $2^8 = 256$ runs, to further screen the significant parameters down to five only.

A tool that originated from high-consequence studies on nuclear reactor safety, known as the Phenomenon Identification and Ranking Table (PIRT), is used to screen the parameters.[27] The PIRT provided in Table 3.3 organizes results obtained with the two-level, full factorial design.

The average variability of frequency predictions for the first three flap-wise bending modes is analyzed using a main-effect ANOVA. "Main-effect" means that the study is restricted to the influence of varying one parameter at-a-time, without considering potential interactions or higher-order effects. Large values of the R^2 composite statistics listed in Table 3.3 identify the most significant main-effects.

Because the twelve parameters considered are unknown, the uncertainty column of the PIRT is omitted in Table 3.3. The lower and upper bounds listed indicate the ranges exercised in the full-factorial design. Values of the main-effect R^2 statistics are scaled to 100%. The PIRT indicates that five of the twelve parameters control nearly 95% of the main-effect variability of frequency predictions. These five parameters are kept for further study while the others are eliminated. The two DOE: (i) two-level, full-factorial design with twelve parameters, and (ii) LHS design with twelve parameters, then, two-level, full-factorial design with eight parameters, arrive at the same list of five most influential parameters. This comparison between two approaches provides evidence that the statistically most significant parameters are identified, and that this result is independent of how the screening is performed.

After screening the initial twelve parameters, an initial Test-Analysis Correlation (TAC) of mode shapes is performed to ensure that (i) the experimental and numerical mode shapes are paired appropriately and (ii) mode swapping does not occur as the material properties are perturbed. A two-level, full-factorial DOE is analyzed to exercise all combinations of lower and upper bounds for the five influential parameters identified in Table 3.3. The mode shape deflections are obtained for these $2^5 = 32$ combinations and plotted in Figure 3.3. While varying the model parameters between the lower and upper bounds generates significant mode shape variability, these shapes consistently correspond to the flapping deflection and mode swapping does not occur due to parameter variations.

Table 3.3: PIRT developed for main-effect screening of twelve FE model parameters.

Factor	Description	Lower Bound	Upper Bound	R^2 Values	Keep?
A	Shear web, ρ	650.46 kg·m^{-3}	1,084.10 kg·m^{-3}	0.29%	**No**
B	Root, ρ	2,071.56 kg·m^{-3}	3,452.60 kg·m^{-3}	0.37%	**No**
C	Lower-edge balsa, ρ	1,025.05 kg·m^{-3}	1,708.42 kg·m^{-3}	0.32%	**No**
D	Spar cap, ρ	1,900.44 kg·m^{-3}	3,167.40 kg·m^{-3}	1.11%	**No**
E	Trailing edge, ρ	659.04 kg·m^{-3}	1,098.40 kg·m^{-3}	9.35%	**Yes**
F	Leading edge, ρ	2,059.68 kg·m^{-3}	3,432.80 kg·m^{-3}	3.03%	**Yes**
G	Shear web, E	0.99 MPa	2.97 MPa	1.74%	**No**
H	Root, E	18.01 MPa	54.02 MPa	0.00%	**No**
I	Lower-edge balsa, E	4.36 MPa	13.08 MPa	1.74%	**No**
J	Spar cap, E	31.04 MPa	93.12 MPa	65.95%	**Yes**
K	Trailing edge, E	0.92 MPa	2.75 MPa	9.85%	**Yes**
L	Leading edge, E	10.30 MPa	30.91 MPa	6.25%	**Yes**

Legend: Column-5 lists composite R^2 statistics obtained for main-effect analysis by averaging individual R^2 for predictions of resonant frequencies of the first three flap-wise bending modes (modes 1, 3, and 4).

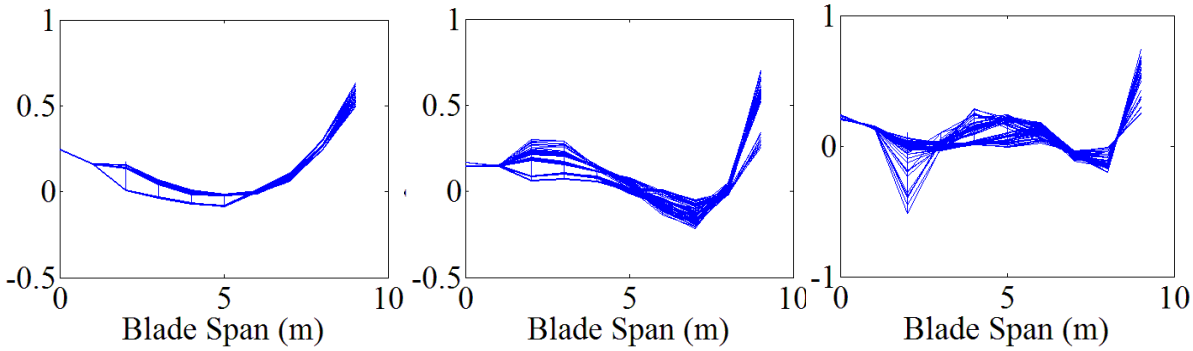

3.3-a) 1st bending (mode-1). 3.3-b) 2nd bending (mode-3). 3.3-c) 3rd bending (mode-4).

Figure 3.3: TAC of mode shape deflections used for the five-parameter study.

With confirmation that the modal pairing is unchanged within the ranges of variation of the five most influential parameters, a three-level, full factorial DOE is analyzed based on 3^5 = 243 runs. Each parameter is set to a lower bound, nominal value (mid-range), or upper bound as listed in Table 3.4. Three levels are used such that the main effects, linear interactions, and quadratic effects can all be captured without significant statistical aliasing. This last design

generates the training data needed to develop a fast-running, statistical emulator for each resonant frequency.

Table 3.4: R^2 statistics for total-effect analysis of five parameters of the FE model.

FE Model Parameter	Parameter Lower Bound	Parameter Upper Bound	R^2 Statistics of Total Effect		
			Mode-1	Mode-3	Mode-4
Trailing edge, ρ	659.04 kg·m^{-3}	1,098.40 kg·m^{-3}	3.46%	10.15%	15.95%
Leading edge, ρ	2,059.68 kg·m^{-3}	3,432.80 kg·m^{-3}	4.63%	9.68%	7.47%
Spar cap, E	31.04 MPa	93.12 MPa	28.57%	28.50%	42.44%
Trailing edge, E	0.92 MPa	2.75 MPa	0.08%	6.39%	2.18%
Leading edge, E	10.30 MPa	30.91 MPa	12.58%	32.69%	28.90%

A final sensitivity analysis is performed using the training data, with results given in Table 3.4. The table lists the total-influence ANOVA statistics for each bending frequency considered. The total effect includes the main effect and all higher-order interactions that involve a given parameter. This analysis confirms that all the parameters kept exercise some degree of influence on the first three flap-wise bending modes of the CX-100 blade model.

3.4.3 Inference Uncertainty Quantification of the Free-free Configuration

At this point, uncertainty has been propagated forward though the simulation of blade vibration and the important parameters that control the prediction variability have been learned. This answers Question-B of section 4.1. Even though the main sources of uncertainty have been reduced to five material properties, acceptable ranges for these parameters remain largely unknown. The next step addresses Question-C by attempting to reduce this lack-of-knowledge. Vibration measurements of the free-free configuration are used to explore settings of the homogenized material properties that lead to predictions that better match the experimental data.

This question could be formulated as a deterministic optimization that searches for the "best" combination of the five material properties. Instead of a deterministic calibration,

Question-C is addressed through **inference uncertainty quantification** that explores the posterior probability distribution of the five parameters. By definition, the posterior is the probability law that leads to predictions of resonant frequencies that are statistically consistent with the experimental data. The challenge is that the posterior function is unknown and must be explored using a Markov Chain Monte Carlo (MCMC) algorithm that turns out to be computationally expensive. Replacing the FE model by fast-running, statistical emulators developed with Gaussian Process Models (GPM) alleviates this difficulty. A GPM is simply a probability distribution whose hyper-parameters, such as mean value and correlation structure, have been trained using the 243 simulation runs of section 4.2. Predictions are then obtained by sampling the probability law instead of analyzing the computationally expensive FE model.

Table 3.5: Comparison of prior and posterior uncertainty of five FE model parameters.

Input Factor	FE Model Parameter	Prior Uncertainty			Posterior Uncertainty		
		Lower	Upper	Range	Mean	Std. Dev.	±2σ Range
E	Trailing edge, ρ ($kg \cdot m^{-3}$)	659	1,098	439	608	61.4	245.4
F	Leading edge, ρ ($kg \cdot m^{-3}$)	2,060	3,433	1,373	1704	246.0	984.1
J	Spar cap, E (MPa)	31	93	62	42	5.9	23.6
K	Trailing edge, E (MPa)	0.9	2.8	1.8	1.9	0.2	0.88
L	Leading edge, E (MPa)	10	31	21	20	5.8	23.0

In the absence of qualitative data about the material, a uniform prior distribution is assumed in the formulation of the GPM. The computational procedure exercised in this study relies on a methodology first proposed in a univariate formulation and later expanded into the multivariate formulation.[28,29]

Table 3.5 summarizes the inference results. Columns 2-to-4 summarize the prior uncertainty, that is, the ranges within which the five material properties are varied in the full-factorial design. This is prior to any comparison between numerical predictions and physical measurements. Columns 5-to-7 describe the posterior uncertainty, that is, the statistics inferred by

performing 100,000 trials of the MCMC search algorithm. Each trial consists in evaluating a new combination of the five parameters by comparing GPM predictions of the three frequencies to measurements. The model visited is retained only if its predictions pass a statistical test of goodness-of-fit with the experimental data and variability. After completing the MCMC iterations, the posterior probability law is inferred from the empirical distribution of the most-often-visited models. These models are those that predict resonant frequencies in acceptable agreement with the measurements. This is assessed using a goodness-of-fit metric that compares predictions and measurements. The MCMC sampling algorithm tends to gravitate around models that yield a better goodness-of-fit. Hence the higher-probability parameter values correspond to models whose predictions match, on average, the measurements with higher accuracy.

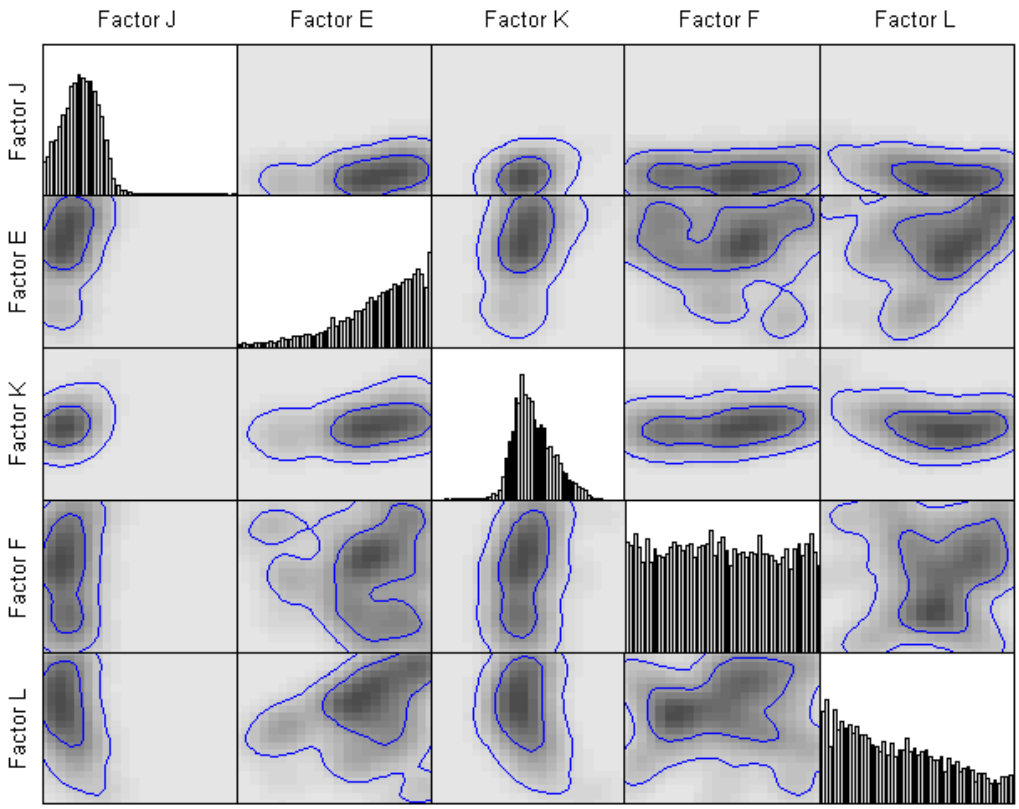

Figure 3.4: Marginal distribution and correlation functions corresponding to Table 3.5.

Figure 3.4 illustrates graphically the five-dimensional posterior probability function corresponding to Table 3.5. Each box on the main diagonal represents a marginal distribution for one of the five parameters. Each off-diagonal box depicts a probability contour for a pair of parameters.

The posterior bounds of ±2 standard deviations listed in Table 3.5 (column 7) can be compared to the prior ranges (column 4). This uncertainty is reduced by, at least, two folds for the moduli of elasticity of the spar cap (factor J) and trailing edge (factor K). This is confirmed graphically by the narrow marginal histograms of these two parameters in Figure 3.4. Knowledge of the two parameters of the leading edge (factors F and L) is not improved significantly likely due to the fact that, as shown in Table 3.3, they contribute only 3% and 6%, respectively, to the overall variability in the model. This is illustrated in Figure 3.4 by relatively "flat" histograms of sampled values that indicate non-informative, posterior marginal functions.

Another important observation from the off-diagonal contours of bivariate probability is that there is no significant correlation between the five model parameters. Observing a correlation would invalidate the development of a simplified, "engineering" model that is based on defining a small number of independent and uncorrelated sections of the blade. It would also generate trade-offs between parameter values that would make it difficult to calibrate the model. Results presented in Table 3.5 and Figure 3.4 answer Question-C by demonstrating that it is possible, at least for two of the five parameters, to reduce the parametric uncertainty in the model through the combination of sensitivity analysis and parameter inference.

Figure 3.5 compares the mean statistics of vibration measurements (with dashed, blue lines) to predictions obtained before and after inference uncertainty quantification. Samples from the prior ranges are shown with red dot symbols while those of the posterior $\pm 2\sigma$ bounds are shown with green star symbols. Each subplot corresponds to one of the frequencies of interest.

The figure indicates that, as expected, combinations of parameters sampled from the joint, posterior distribution yield models whose predictions tend to agree better with measurements. It confirms that the inference, while reducing the uncertainty of three of the most influential parameters (see Table 3.5), also contributes to better predictions of the flap-wise vibration modes of interest.

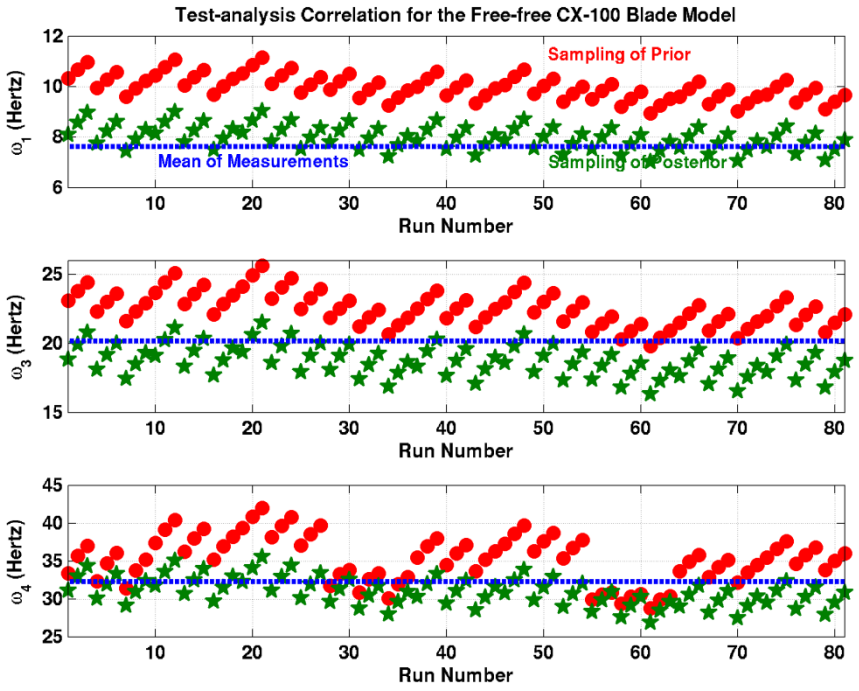

Figure 3.5: Prior and posterior predictions for the free-free configuration.

The fixed-free configuration of the CX-100 blade is investigated next. The simplified model is essentially the same, with the exception of adding springs to the base to represent the boundary condition compliance. In this second stage, the sensitivity analysis and inference are focused on reducing the uncertainty of material properties for the root section and boundary springs.

3.4.4 Propagation of Uncertainty and Sensitivity Analysis of the Fixed-free Configuration

The analysis proceeds with the numerical simulation of the fixed-free configuration of the blade where additional springs are added to represent the boundary condition compliance. Separating the free-free and fixed-free configurations decouples the homogenized properties investigated so far in sections 4.2 and 4.3 from those of the fictitious boundary springs.

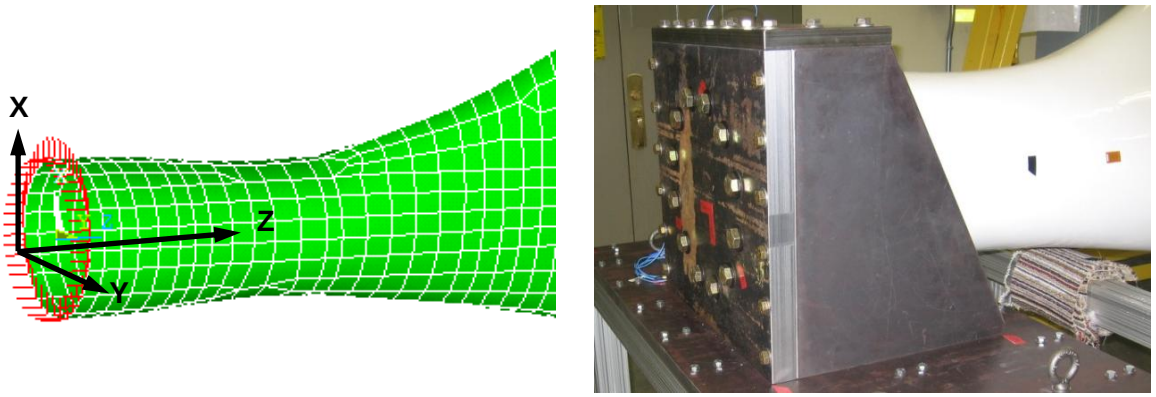

Figure 3.6: Close-up of the simulated springs (left) and close-up of the bookend (right).

Figure 3.6 shows that the fixed-free configuration is realized experimentally by attaching the CX-100 blade to a steel "bookend" fixture, weighing approximately 500 lbf (or 250 kg). Although this attachment is used to create a fixed boundary condition, there is an inherent uncertainty due to the difficulty in producing an infinitely rigid connection. Fictitious springs are implemented in the simplified FE model to account for this uncertainty and generate a boundary condition for which the support is neither completely "free" nor "fixed." It is also noted, through an effect screening study, that rotational springs at the base of the blade do not exercise any significant influence on the vibration characteristics. The fixture attachment is limited to translational springs that are added in the X, Y, and Z directions at forty locations around the diameter of the base of the root. Springs in the X and Y directions are assumed to be identical because they act in the same plane.

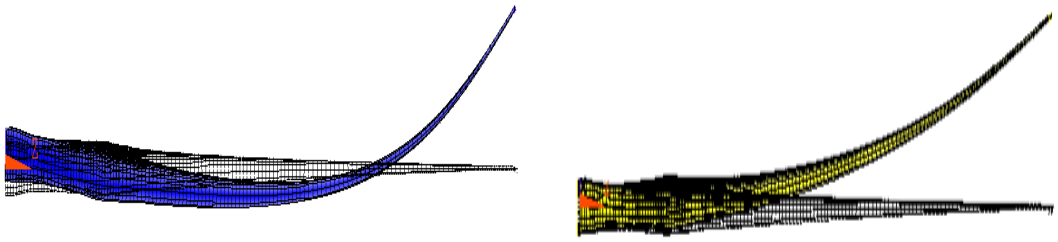

3.7-a) First flap-wise mode under free-free (left) and fixed-free (right) conditions.

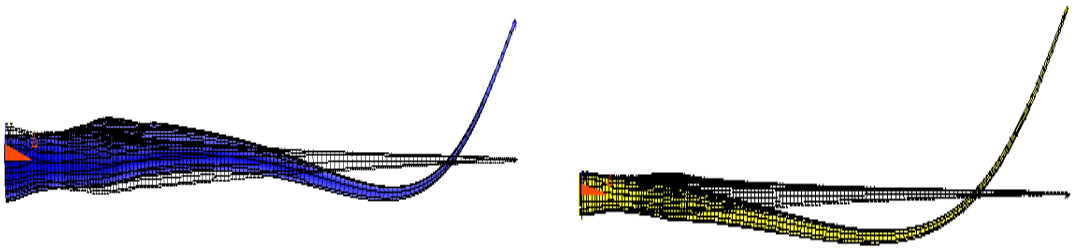

3.7-b) Second flap-wise mode under free-free (left) and fixed-free (right) conditions.

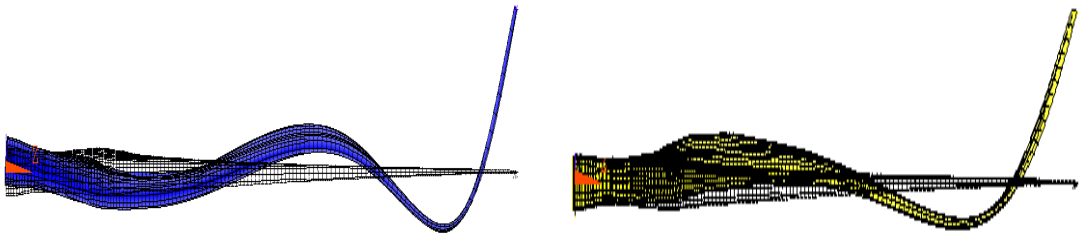

3.7-c) Third flap-wise mode under free-free (left) and fixed-free (right) conditions.

Figure 3.7: Comparison of the simulated free-free and fixed-free mode shape deflections.

A difficulty introduced by the addition of boundary springs is that parametric studies are prone to mode swapping as the spring stiffness coefficients are varied. As shown in Figure 3.7, a mismatch between the first modes of the simulated free-free and fixed-free configurations is observed. It is deduced from this comparison that the first flap-wise bending mode of the fixed-free setting is not obtained until the boundary springs are sufficiently stiff. A preliminary

parametric study is therefore devoted to learning ranges for the spring stiffness coefficients that, while they avoid mode swapping as much as possible, transition between the free-free and fixed-free conditions.

Simulations indicate that the vibration behavior converges asymptotically to the fixed-free blade when the boundary spring stiffness coefficients are sufficiently large. Likewise, decreasing the coefficients converges to the free-free behavior. This is illustrated in Figure 3.8. The first flap-wise mode of the free-free configuration occurs for spring stiffness coefficients smaller than 10^{+6} N/m, approximately. The vibration behavior approaches the fixed-free configuration for coefficients that exceed 10^{+8} N/m. These two values are, therefore, good candidates to define the lower and upper bounds of the subsequent parametric studies.

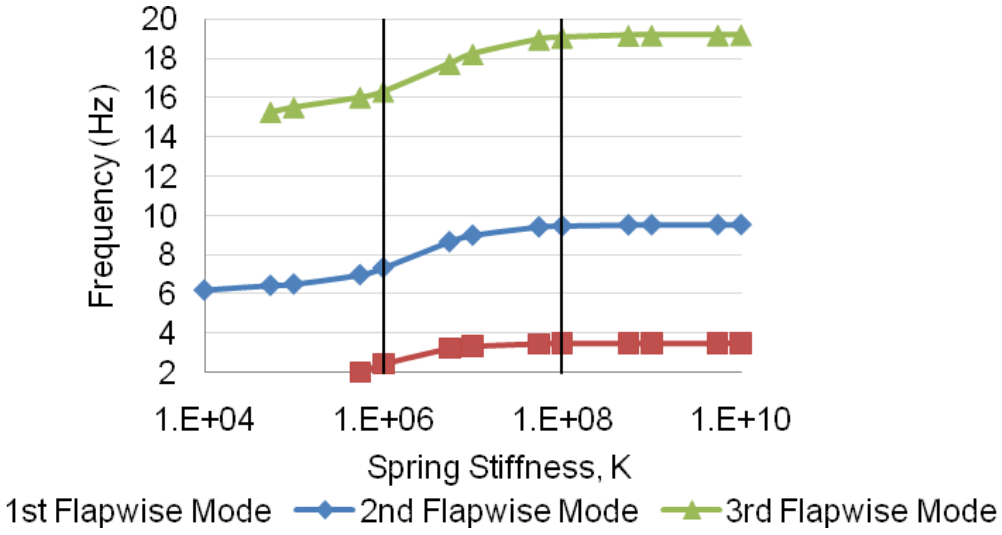

Figure 3.8: Effect of varying the boundary spring coefficients on bending frequencies.

The lower bound cannot be argued about because decreasing the boundary spring coefficient below 10^{+6} N/m suppresses the first free-free flap-wise bending mode, as indicated in Figure 3.8. To verify that the upper bound yields a stiff-enough attachment, a comparison is made with a simulation where the boundary springs are removed and, instead, nodes at the base of the

blade are fixed in all directions. Figure 3.9 compares the first three flap-wise bending deflections of this pinned connection to those obtained with boundary spring coefficients of 10^{+8} N/m. The figure indicates an excellent agreement between the two sets of shapes. In addition, frequency differences do not exceed 0.1%. Based on these observations, it is concluded that setting the upper bound at 10^{+8} N/m suffices to define the fixed-free boundary condition.

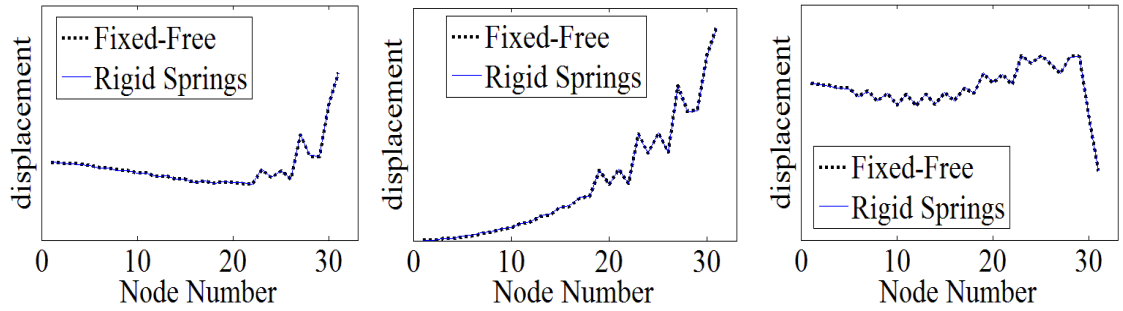

3.9-a) 1st bending (mode-1). **3.9-b) 2nd bending (mode-3).** **3.9-c) 3rd bending (mode-5).**

Figure 3.9: Shapes of a pinned boundary compared to those obtained with k = 10^{+8} N/m.

Sensitivities of the simplified model for the fixed-free boundary condition are investigated next. It is noted that a complete analysis is unnecessary because the simplified model has already been studied in the free-free configuration. Only the homogenized material properties that are anticipated to exercise a statistically significant effect need to be re-evaluated. They include parameters for the spar cap (factor J) and trailing edge (factors E and K), according to Table 3.3. In the free-free case, properties of the root were found to be insignificant contributors to the resonant frequency variability. In the fixed-free case, however, the strain energy is re-distributed and shifted towards the base of the blade. Therefore, the material parameters of the root section must be included in the study, together with the stiffness coefficients of boundary springs.

These considerations suggest a total of seven model parameters to investigate the variability of resonant frequencies and mode shape deflections. The seven parameters include one stiffness coefficient for boundary springs added in the Z-direction, and another stiffness coefficient for all springs parallel to either the X or Y axis. A two-level full-factorial DOE is utilized in an attempt to keep the parametric study to a manageable size with $2^7 = 128$ runs. A two-level design is deemed sufficient to screen the statistically significant effects.

Table 3.6: Total-effect R^2 statistics for seven parameters of the fixed-free configuration.

Input Factor	FE Model Parameter	Parameter Lower Bound	Parameter Upper Bound	Total-effect R^2 Statistics			Keep?
				Mode-1	Mode-3	Mode-5	
B	Root, ρ ($kg \cdot m^{-3}$)	2,072	3,453	0.00%	0.00%	0.00%	**No**
E	Trailing edge, ρ ($kg \cdot m^{-3}$)	484.4	729.8	1.59%	5.14%	12.47%	**Yes**
H	Root, E (MPa)	18.01	54.02	0.18%	0.58%	0.72%	**No**
J	Spar cap, E (MPa)	29.92	53.56	6.90%	27.30%	29.17%	**Yes**
K	Trailing edge, E (MPa)	1.48	2.35	0.07%	0.15%	5.17%	**No**
M	(X; Y) spring, k_1 ($N \cdot m^{-1}$)	10^{+6}	10^{+8}	0.00%	0.00%	0.03%	**No**
N	Z spring, k_2 ($N \cdot m^{-1}$)	10^{+6}	10^{+8}	39.44%	66.26%	50.14%	**Yes**

Table 3.6 summarizes the results of sensitivity analysis by listing the total-effect R^2 statistics from the decomposition of variability for the first three flap-wise bending frequencies. The material properties of the root section (factors B and H) are observed to have an insignificant effect on the vibration response of the model. It is possible that the more dominant parameters simply outweigh the contribution of these properties for the root section. It is also observed that only the translational springs in the Z-direction have a significant influence on the response. This is likely due to the fact that, the flap-wise bending behavior of the blade exercises the springs oriented in the Z-direction, which are parallel to the orientation of the spar cap (see Figure 3.6). This bending does not strain springs oriented in the (X; Y) plane as much, which explains the low influence of parameter k_1 in Table 3.6.

The sensitivity results are used to reduce the number of parameters from seven to three, as shown in Table 3.6. A four-level, full-factorial design, populated with $4^3 = 64$ runs, is analyzed next to generate the training data required for inference in section 4.5. The bounds within which each parameter is allowed to vary are those listed in Table 3.6. The objective of inference uncertainty quantification is to reduce this lack-of-knowledge as much as possible.

3.4.5 Inference Uncertainty Quantification of the Fixed-free Configuration

The results of inference uncertainty quantification are briefly summarized for simulations of the fixed-free configuration. The statistics of the MCMC exploration of the three-parameter space (factors E, J, and N of Table 3.6) are listed in Table 3.7, and posterior distributions illustrated in Figure 3.10. These statistics are obtained with 20,000 iterations for the MCMC exploration of the three-parameter space. This number of samples is sufficient to estimate the posterior probability distribution with reasonable accuracy. This is because common practice is to use no fewer than a hundred iterations per variable explored, which would require about 300 samples for our application. Using 20,000 iterations exceeds this minimum expectation to provide sufficiently converged statistics.

Table 3.7: Comparison of prior and posterior uncertainty of three FE model parameters.

Input Factor	FE Model Parameter	Prior Uncertainty			Posterior Uncertainty		
		Lower	Upper	Range	Mean	Std. Dev.	±2σ Range
E	Trailing edge, ρ ($kg \cdot m^{-3}$)	484.37	729.81	245.44	593.11	66.99	267.96
J	Spar cap, E (MPa)	29.92	53.56	23.64	40.66	2.76	11.04
N	Z spring, k_2 (x 10^{+6} $N \cdot m^{-1}$)	1.00	100.0	99.00	53.71	27.59	110.36

Again, the inference successfully reduces the lack-of-knowledge of the modulus of elasticity of the spar cap (factor J). This does not come as a surprise because this factor is the second most influential. The reduction of uncertainty is indicated by a narrow histogram in Figure 3.10. It is also apparent that the statistics of the modulus of elasticity obtained with inference of

the free-free configuration (E = 41.7 ± 5.9 MPa in Table 3.5) are consistent with those obtained with inference of the fixed-free configuration (E = 40.7 ± 2.8 MPa in Table 3.7).

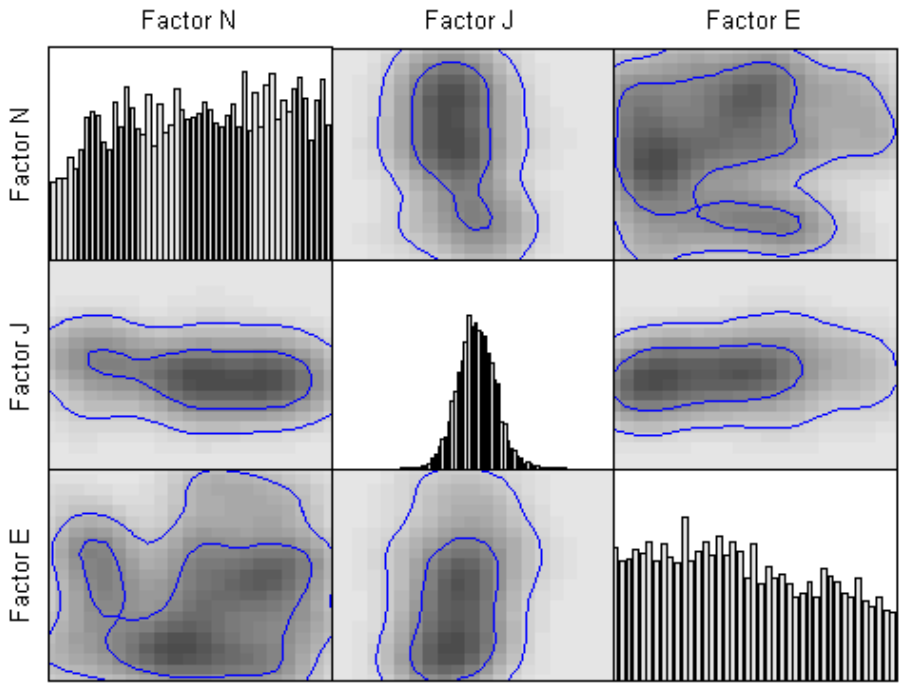

Figure 3.10: Marginal distribution and correlation functions corresponding to Table 3.7.

The inference is not able, on the other hand, to mitigate our ignorance of the boundary spring coefficient in the Z-direction (factor N). Table 3.6 shows that this failure cannot be attributed to a lack of sensitivity of resonant frequencies to the spring coefficient. A possible explanation is that the bookend attachment of the blade is not massive enough to facilitate the storage of a significant quantity of strain energy near the base. Consequently, the vibration measurements may be somewhat uninformative to constrain the value of the boundary spring stiffness. The inference is also unsuccessful for the density of the trailing edge (factor E). This could be due to a potential interaction between the density and the boundary spring during calibration. The contribution of the density to the overall variability of the model in both the free-

free and fixed-free cases is low relative to the other parameters, possibly resulting in poor inference results.

Figure 3.11 is the counterpart of Figure 3.5 and shows a comparison between the mean statistics of vibration measurements (with dashed, blue lines) and predictions of the simplified FE model obtained before and after inference. Samples from the prior ranges are shown with red dot symbols while those of the posterior ±2σ bounds are shown with green star symbols. Each subplot corresponds to one of the frequencies of interest. It can be observed that, even though the study is restricted to three parameters only, samples obtained from the posterior distribution tend to agree better with the physical measurements.

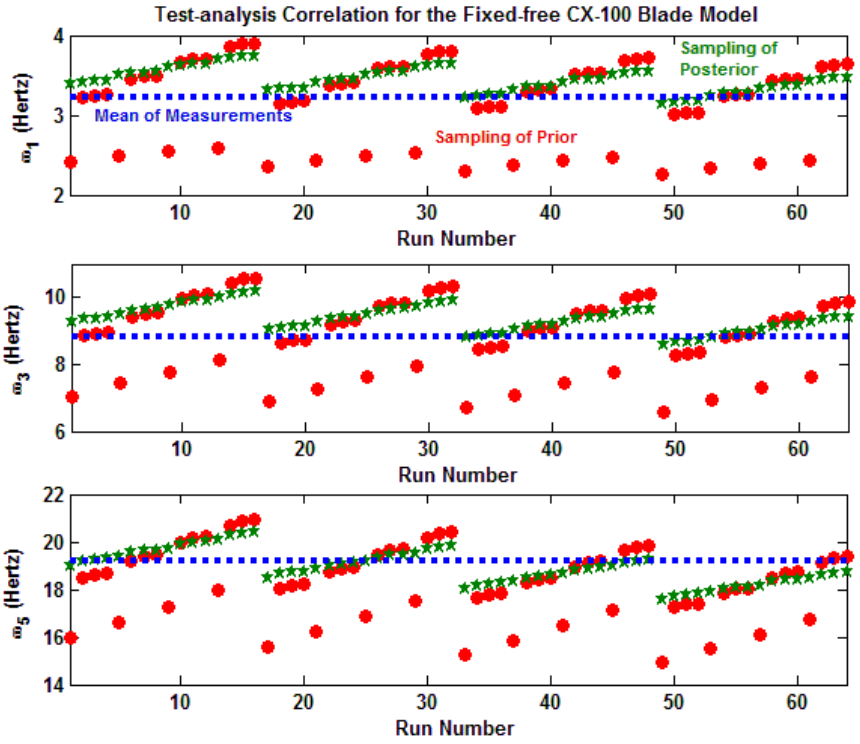

Figure 3.11: Prior and posterior predictions for the fixed-free configuration.

This application illustrates that the combination of statistical effect screening (sections 4.2 and 4.4) and inference uncertainty quantification (sections 4.3 and 4.5) is a powerful tool to

reduce the parametric uncertainty of the simplified model. The results obtained answer Question-C but prove nothing regarding the predictive power of the model. In section 5, TAC is applied to the mode shape deflections to assess the overall validity of the model.

3.5. Validation Assessment Using the Mode Shape Deflections

The predictive power of the simplified FE model is assessed through TAC of the mode shape deflections. The reason for this choice is two-fold. First, the mode shapes have not been used previously for sensitivity analysis or inference uncertainty quantification. These deflections provide a separate dataset for validation of the model. It is emphasized that using experimental data that were not considered during calibration is essential to validate the predictive capability of a model. One could argue, rightfully so, that the mode shape vectors used for validation are not truly independent from the resonant frequencies used for calibration. After all, they both originate from the same modal test. This is, however, the best that could be achieved given the unavailability of other datasets at the time the study was initiated. The second reason is that the simplified FE model of blade dynamics is developed for a future integration with the simulation of flow around the turbine. For credible fluid-structure interaction, it is important to establish that the model provides accurate predictions of the bending and torsion deflections.

Predictions of mode shapes are generated from multiple simulation runs obtained by sampling the posterior distributions of material properties and spring coefficients for the two boundary conditions considered (both free-free or fixed-free). These runs are used to establish that the simplified model is able to capture several aspects of the problem, such as predicting different attachment conditions or reproducing the overall experimental variability.

The TAC is illustrated graphically in Figure 3.12 for the free-free boundary condition and Figure 3.13 for the fixed-free configuration. In both figures, the experimentally identified mode shapes are plotted using solid, red lines. Variability from the simulation predictions is reported

with box plots (using blue symbols). The left sides of Figures 3.12 and 3.13 compare values of the measured and predicted displacements. The right sides compare the overall deflection shapes of the first three flap-wise bending modes.

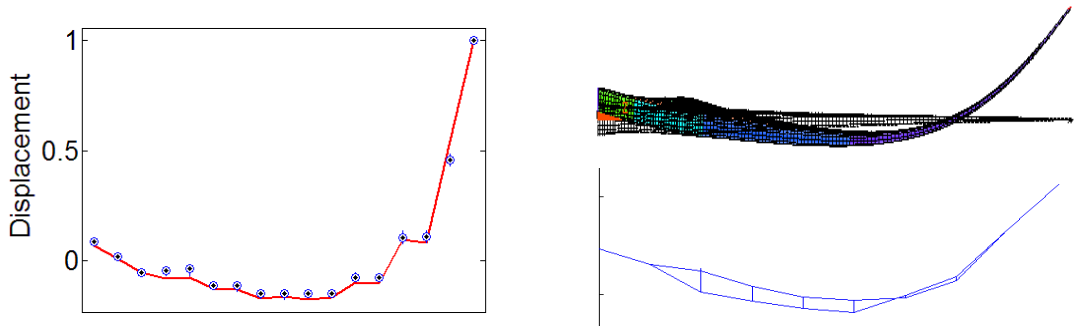

3.12-a) TAC (left), measured and simulated shapes (right) for the first bending mode.

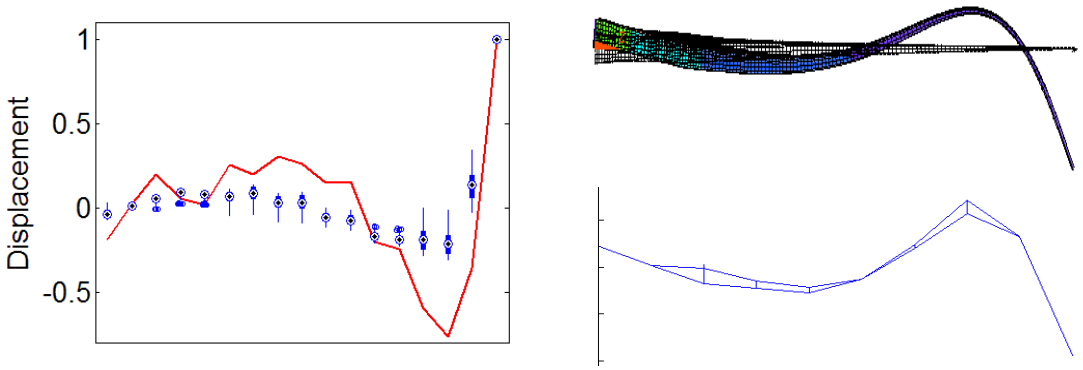

3.12-b) TAC (left), measured and simulated shapes (right) for the second bending mode.

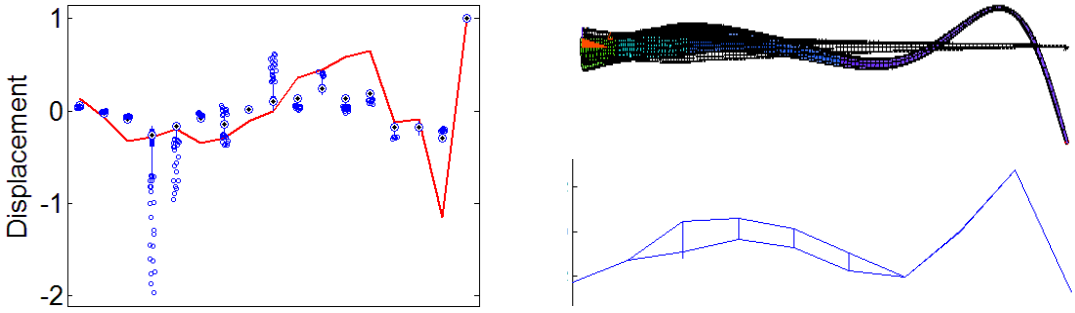

3.12-c) TAC (left), measured and simulated shapes (right) for the third bending mode.

Figure 3.12: Measured and simulated mode shapes for the free-free configuration.

An excellent degree of correlation is obtained for the first mode shape of the free-free boundary condition in Figure 3.12, however, the agreement breaks down with higher order modes. This may be explained by the fact that higher-order mode shapes are more difficult to excite and identify experimentally. On the modeling side, a higher-order deflection may be more sensitive than the first bending mode to the definition of a relatively small number of sections in the model (only six sections). Both effects would tend to deteriorate the correlation observed. The overall degree of TAC of the first three flap-wise bending modes is, nevertheless, deemed satisfactory based, not only, on these visual comparisons but also on the coefficients of correlation estimated next.

Figure 3.13 illustrates the mode shape correlation for the fixed-free configuration. A high degree of agreement is, again, obtained between the measured and predicted deflections. The higher-order modes tend to be better correlated to measurements than those obtained for the free-free boundary condition. This is a welcome observation because the simplified model will eventually be integrated to a coupled, structural-fluid simulation of the entire turbine, which implies a fixed attachment at the root of each blade. Less prediction variability is obtained for the fixed-free configuration due to the fact that only three parameters are varied, compared to the five material properties exercised in the analysis of the free-free boundary condition. The ability of the model to reproduce the experimental measurements, using parameters obtained from an inference based on resonant frequencies, establishes that the boundary springs utilized have the potential to produce reliable predictions of the blade behavior.

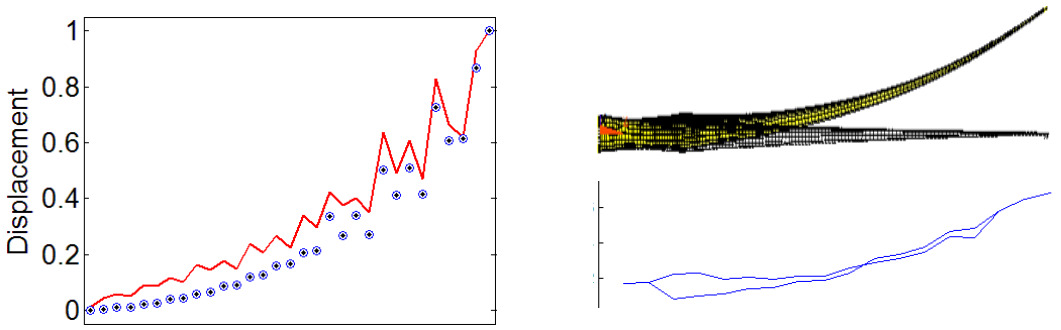

3.13-a) TAC (left), measured and simulated shapes (right) for the first bending mode.

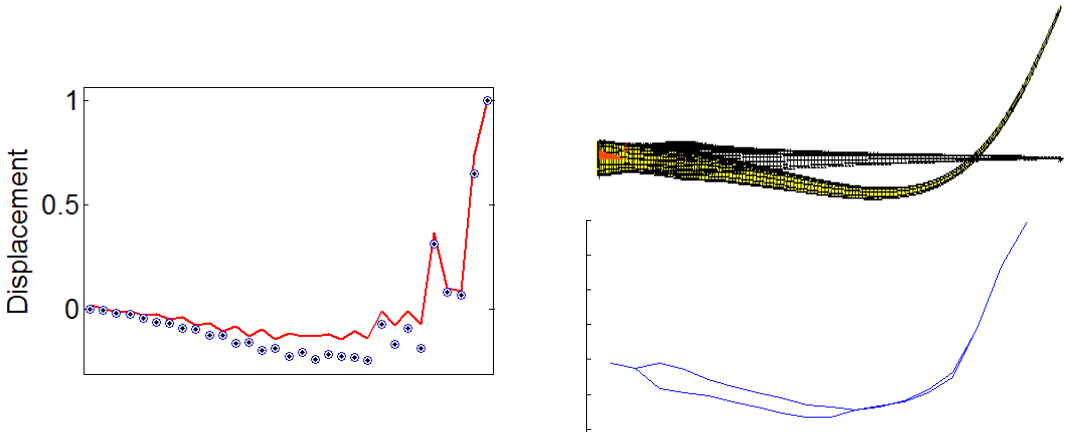

3.13-b) TAC (left), measured and simulated shapes (right) for the second bending mode.

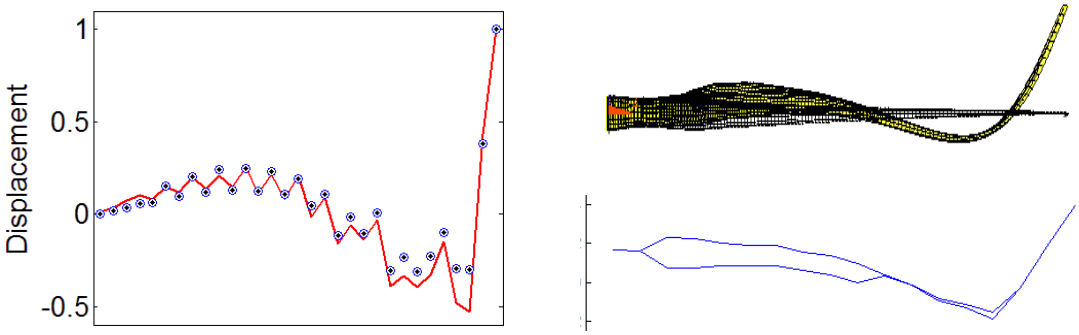

3.13-c) TAC (left), measured and simulated shapes (right) for the third bending mode.

Figure 3.13: Measured and simulated mode shapes for the fixed-free configuration.

The Modal Assurance Criterion (MAC) is calculated to quantify the correlation of mode shapes obtained for the experimental and simulation results. The MAC is a coefficient of correlation:

$$\mathrm{MAC}=\frac{\left(\Phi_{\mathrm{Test}}^{\mathrm{T}}\cdot\Phi_{\mathrm{Model}}\right)^{2}}{\left(\Phi_{\mathrm{Test}}^{\mathrm{T}}\cdot\Phi_{\mathrm{Test}}\right)\left(\Phi_{\mathrm{Model}}^{\mathrm{T}}\cdot\Phi_{\mathrm{Model}}\right)}, \tag{1}$$

where Φ_{Test} and Φ_{Model} are the measured and simulated mode shapes, respectively, expressed at the same degrees-of-freedom. The purpose of this analysis is to verify the extent to which the deflections are parallel for the same modes and orthogonal for different modes.

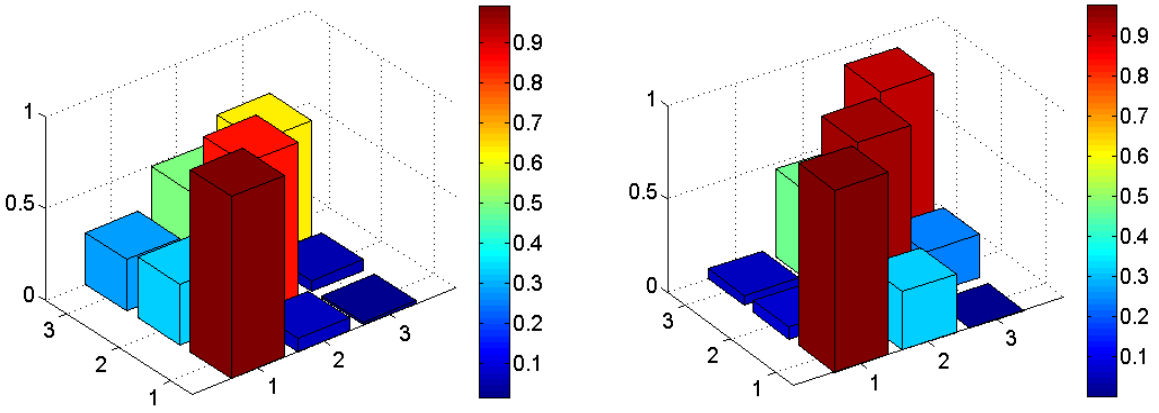

Figure 3.14: Mode shape MAC of the free-free (left) and fixed-free (right) configurations.

Figure 3.14 illustrates MAC values for the free-free and fixed-free configurations of the blade. The simulated deflections are predicted by the FE model using average parameter values estimated from the posterior distributions of Figure 3.4 (free-free) and Figure 3.10 (fixed-free). Large values on the main diagonal indicate strong correlations between similar modes. On average, the diagonal MAC values are 84% for the free-free boundary, and 94% for the fixed-free boundary. Likewise, small values of the off-diagonal suggest that dissimilar modes are orthogonal, as they should be. On average, the off-diagonal MAC values are 21% for the free-free boundary, and 19% for the fixed-free boundary. These observations validate the ability of the simplified model to predict mode shape deflections, hence, answering Question-D.

3.6. Conclusion

This second half of a two-part publication discusses the development of a simplified finite element model of a wind turbine blade. A particular effort is made to quantify all sources of uncertainty in the simulation, and assess their effects on predictions of the low-frequency vibration dynamics of the blade. Because it is exposed to the danger of over-fitting, conventional calibration is not performed to reconcile model predictions and physical measurements. Instead, Verification and Validation (V&V) activities are employed to assess the overall predictive capability of the model. The discussion illustrates what can be learned from specific V&V activities, and how these can be integrated to the model development process.

The objective of this work is to develop a fast-running, "engineering" model of blade vibrations for future integration with a fluid dynamics simulation for an entire wind turbine and, eventually, an entire wind plant composed of multiple turbines. It implies that the structural model must be fast-running while providing an accurate-enough representation of the low-order bending and torsion dynamics that will be coupled to the flow around the blade. Four questions are asked regarding specific aspects of the predictive capability being developed:

- **Question-A:** what is an appropriate level of mesh resolution for the calculations?
  Answer: Mesh refinement, combined to an upper bound of solution uncertainty, suggests that a mesh size of 8.0 cm provides accurate-enough predictions of resonant frequencies. The average solution uncertainty, due to truncation error, is estimated to be 1.78%, which is similar to the overall experimental variability (1.62%). This particular mesh, case-specific for our application, provides an extraction of resonant mode shapes and frequencies in less than 60 seconds. (See Reference 12.)
- **Question-B:** what are the parameters that most influence the variability of predictions?
  Answer: Designs-of-experiments are used in conjunction with variance decomposition to identify parameters of the model that control the variability of frequency predictions. The

top-three most influential parameters are the moduli of elasticity of the spar cap and leading edge section, and density of the trailing edge section. Boundary springs are also influential. Knowing these parameters allows for a more efficient reduction of the prediction variability.

- **Question-C:** can measurements be used to reduce the parametric uncertainty in the model?
  Answer: Measurements of the vibration response in two configurations, free-free and fixed-free, can be used to reduce the lack-of-knowledge of model parameters. This is achieved through inference uncertainty quantification, as opposed to deterministic calibration of the parameters. The ignorance of the most influential parameters is reduced by two folds, if not more. The average plus-or-minus one standard deviation statistics are: $E = 40.7 \pm 2.8$ MPa for the spar cap; $E = 19.5 \pm 5.8$ MPa for the leading edge section; $\rho = 607.1 \pm 61.4$ kg·m^{-3} for the trailing edge section; and $k_2 = 53.7 \pm 27.6$ (x 10^{+6}) N·m^{-1} for the boundary springs. Proceeding in two separate steps, first, with the free-free blade, then, with the fixed-free blade, enables a decoupling between the boundary springs and most other parameters.
- **Question-D:** does the model provide accurate-enough predictions of mode shapes?
  Answer: The ability of the simplified model to predict mode shape deflections is validated through test-analysis correlation. The degree of agreement observed is excellent considering the complexity of the structure, with 84% correlation for the free-free modes and 94% correlation for the fixed-free modes. Datasets used for validation (mode shapes) are kept separate from, and independent of, the data to which the sensitivity analysis and statistical inference are applied (resonant frequencies).

The panoply of V&V activities deployed for this application include verifying the implementation of the software; performing mesh refinements to estimate the solution uncertainty; developing a Phenomenon Identification and Ranking Table to define the important parameters; running designs-of-computer-experiments to, first, identify the most significant effects through sensitivity analysis and, second, develop fast-running Gaussian Process Model

emulators; propagating uncertainty from model parameters to frequency and mode shape predictions; and performing inference uncertainty quantification to reduce the lack-of-knowledge of material properties and boundary springs. The overall validation assessment is grounded in the test-analysis correlation of mode shape deflections, which are data that have not been used for the sensitivity analysis and uncertainty quantification.

The study concludes that our scientific hypothesis is confirmed: a simplified-but-credible model of the low-frequency, structural response can be developed for future integration with the flow dynamics simulation. This positive finding is an encouragement to pursue this work even further with the on-going development and V&V of a non-linear beam element capable to describe the large displacements and large deformations witnessed by blades during the normal operation of a wind turbine. Future work will involve integrating the simplified finite element model, one-dimensional beam element, and computational fluid dynamics software for the numerical simulation of performance of entire wind plants.

The development of future models will also take into account experimental data that further exercise the compliance of the fixed-free boundary condition. New vibration tests have been executed with another suspension system and the addition of masses that further stress the compliance of the fixed-free boundary condition. Future test-analysis correlation will promote a better understanding of the role that the boundary spring stiffness plays in model development.

References

1. U.S. Department of Energy. 20% Wind Energy by 2030: Increasing Wind Energy's Contribution to U.S. Electricity Supply. Report DOE/GO-102008-2567, Washington, D.C., 2008.

2. Veers PS. Ashwill TD. Sutherland HJ. Laird DL. Lobitz DW. Griffin DA. Mandell JF. Musial WD. Jackson K. Zuteck M. Miravete A. Tsai SW. Richmond JL. Trends in the Design, Manufacture, and Evaluation of Wind Turbine Blades. *Wind Energy*. 2003; **6**: 245-259.

3. Ciang CC. Lee JR. Bang HJ. Structural Health Monitoring for a Wind Turbine System: A Review of Damage Detection Methods. *Measurement Science and Technology* 2008; **19**: 1-20.

4. Liu W. Tang B. Jiang Y. Status and problems of wind turbine structural health monitoring techniques in China. *Renewable Energy* 2010; **35**: 1414-1418.

5. Larsen FM. Sorensen T. New Lightning Qualification Test Procedure for Large Wind Turbine Blades. *International Conference on Lightning and Static Electricity*, Blackpool, United Kingdom, 2003.

6. Walford CA. Wind Turbine Reliability: Understanding and Minimizing Wind Turbine Operation and Maintenance Costs. Sandia Report, SAND2006-1100, Sandia National Laboratories, Albuquerque, NM, 2006.

7. Resor B. Paquette J. Laird D. Griffith DT. An Evaluation of Wind Turbine Blade Cross Section Analysis Techniques. *52th AIAA/ ASME/ASCE/AHS/ASC Structures, Structural Dynamics, and Materials Conference*, Orlando, FL, 2010.

8. Jensen FM. Falzon BG. Ankersen J. Stang H. Structural Testing and Numerical Simulation of a 34-m Composite Wind Turbine Blade. *Composite Structures* 2006; **76**: 52-61.

9. Freebury G. Musial W. Determining Equivalent Damage Loading for Full-scale Wind Turbine Blade Fatigue Tests. *19th ASME Wind Energy Symposium*, Reno, NV, 2000.

10. Griffith DT. Paquette JA. Carne TG. Development of Validated Blade Structural Models. *46th AIAA Aerospace Sciences Meeting and Exhibit*, Reno, NV, January 2008.

11. Vermeer LJ. Sorensen JN. Crespo A. Wind Turbine Wake Aerodynamics. *Progress in Aerospace Sciences* 2003; **39**: 467-510.

12. Mollineaux MG. Van Buren KL. Hemez FM. Simulating the Dynamics of Wind Turbine Blades: Part I, Model Development and Verification. *13th AIAA Non-deterministic Approaches Conference*, Denver, CO, April 2010. (Also, Los Alamos report LA-UR-10-5604.)

13. Malcolm DJ. Laird DL. Extraction of Equivalent Beam Properties From Blade Models. *Wind Energy* 2006; **10**: 135-157.

14. Martins M. Perdana A. Ledsam P. Agneholm E. Carlson O. Validation of Fixed Speed Wind Turbine Dynamic Models With Measured Data. *Renewable Energy* 2007; **32**: 1301-1316

15. Hemez FM. Ben-Haim Y. The Good, the Bad, and the Ugly of Predictive Science. *4th International Conference on Sensitivity Analysis of Model Output*, Santa Fe, NM, March 2004.

16. Griffith DT. Carne TG. Paquette JA. Modal Testing for Validation of Blade Models. *Wind Engineering* 2008; **32**: 91-102.

17. Deines K. Marinone T. Schultz R. Farinholt K. Park G. Modal Analysis and Structural Health Monitoring Investigation of CX-100 Wind Turbine Blade. *29th International Modal Analysis Conference*, Jacksonville, FL, 2011.

18. Griffith DT. Hunter PS. Kelton DW. Carne TG. Paquette JA. Boundary Condition Considerations for Validation of Wind Turbine Blade Structural Models. *SEM Annual Conference and Exposition on Experimental and Applied Mechanics*, Albuquerque, NM, June 2009.

19. White JR. Adams DE. Rumsey MA. Modal Analysis of CX-100 Rotor Blade and Micon 65/13 Wind Turbine. *28th International Modal Analysis Conference*, Jacksonville, FL, February 2010.

20. Bechly ME. Clausen PD. Structural Design of a Composite Wind Turbine Blade Using Finite Element Analysis. *Computers and Structures* 1997; **63**: 639-646.

21. Veers PS. Laird DL. Carne TG. Sagartz MJ. Estimation of Uncertain Material Parameters Using Modal Test Data. *36th AIAA Aerospace Sciences Meeting*, Reno, NV, January 1998.

22. Kong C. Bang J. Sugiyama Y. Structural Investigation of Composite Wind Turbine Blade Considering Various Load Cases and Fatigue Life. *Energy* 2005; **30**: 2101-2114.

23. Shokrieh MM. Rafiee R. Simulation of Fatigue Failure in a Full Composite Wind Turbine Blade. *Composite Structures* 2006; **74**: 332-342.

24. Askeland D. Fulay P. Wright W. *The Science and Engineering of Materials*. CL-Engineering: Stamford, CT, 2010.

25. McKay MD. Beckman RJ. Conover WJ. A Comparison of Three Methods For Selecting Values of Input Variables in the Analysis of Output From a Computer Code. *Technometrics* 1979; **21**: 239-245.

26. Saltelli A. Chan K. Scott EM. *Sensitivity Analysis*. John Wiley and Sons: New York, NY, 2000.

27. Wilson GE. Boyack BE. The Role of the PIRT Process in Experiments, Code Development and Code Applications Associated With Reactor Safety Analysis. *Nuclear Engineering and Design* 1998; **186**: 23-37.

28. Kennedy M. O'Hagan A. Predicting the Output From a Complex Computer Code When Fast Approximations are Available. *Biometrika* 2000; **87**: 1-13.

29. Higdon D. Gattiker J. Williams B. Rightley M. Computer Model Calibration Using High-Dimensional Output. *Journal of the American Statistical Association* 2008; **103**: 570-583.

CHAPTER FOUR

MODEL SELECTION THROUGH ROBUSTNESS AND FIDELITY CRITERIA: MODELING THE DYNAMICS OF THE CX-100 WIND TURBINE BLADE

4.1 Introduction

The wind energy industry in the United States has consistently observed the design of larger wind turbines, with blades up to 61.5 meters in length in 2011. In anticipation of this continued trend, blades 100 meters in length are already being pursued for future wind turbine designs [1]. The behavior of wind turbines produced at this massive scale can be economically and efficiently studied through modeling and simulation techniques, which enable designers to consider both aerodynamic and structural concerns early in the design process [2], and mitigate the increasing costs of full-scale testing [3]. Finite element (FE) models calibrated against experimental data have gained acceptance for routine use in studying the static and dynamic responses of wind turbine blades, as demonstrated by the inclusion of FE analysis in wind turbine design standards [4]. Further, FE models are advantageous to study complex load cases that arise from in-service wind loading [5,6], as compared to the idealized loads that are implemented in full-scale experiments [7].

Assumptions and simplifications are routinely implemented in FE models to reduce the computational demands of the simulation. For instance, current computing resources and code capabilities prevent the simulation of plant performance based on full-physics, full-coupling, three-dimensional representations of the structural response and air flow. Accordingly, it has been proposed to simulate wind turbines using geometrically non-linear, one-dimensional beam elements when coupling FE models of the wind turbine structural response with computational fluid dynamics models of the surrounding airflow [8]. Here, the use of simplified, one-dimensional beam elements is selected according to expert judgment. The main concern that

arises is then the extent to which predictions of a numerical simulation can be trusted, given that the modeling strategy is selected according to subjective opinion of the expert.

Aside from lack-of-knowledge in the optimal modeling strategy, a lack-of-knowledge also exists in the optimal values for the input parameters that define the selected modeling strategy. In spite of this dual lack-of-knowledge, recent wind turbine studies continue to consider a model *good quality* when model predictions match physical experiments by calibrating the input parameters [5,9]. However, when the quality of numerical models is assessed solely by fidelity to experimental data, the modeling strategy preference may lean towards overly complex models [10]. Model complexity, as defined by the model form and the number of parameters used to define this model form, can affect the quality of model predictions [10,11]. Overly complex models run the risk of over-fitting experimental data and at the cost of a poor generalization to non-tested settings [10]. For this reason, it has been posited that numerical models should not only demonstrate fidelity to data, but also be robust to lack-of-knowledge such that model predictions remain consistent as uncertainties in the model are exercised. When considering lack-of-knowledge in the input parameters, robustness often favors less complex models that demonstrate lower variability in predictions as lack of knowledge is increased. However, more complex models are often capable of providing a better fit to experimental data. This paradigm in modeling and simulation has been formally recognized. It can be shown that fidelity-to-data and robustness to lack-of-knowledge are antagonistic attributes of any family of models [12]. Therefore, the predictive abilities of alternative modeling strategies must be compared considering not only fidelity of model predictions to experiments but also the robustness of model predictions to uncertainties in the corresponding input parameters.

This manuscript proposes a rigorous and quantitative model selection approach rooted in info-gap decision theory (IGDT) [13]. The approach proposed herein deviates from other model

selection methods (see Section 2), because it is non-probabilistic in nature, and is performed by assessing the trade-offs of fidelity and robustness. The basic premise behind the proposed approach is that a good-quality model should be able to reproduce the available measurements, but should also provide predictions that are as insensitive as possible to uncertainties.

This approach is demonstrated on the bending vibration of the CX-100 wind turbine blade developed at the Sandia National Laboratories (SNL). In two earlier studies, the FE model of the CX-100 blade has undergone rigorous **V**erification and **V**alidation (V&V) assessments to ensure the credibility of predictions using measurements conducted at Los Alamos National Laboratory (LANL) (see Mollineaux et al. [14] for model verification and Van Buren et al. [15] for the model validation). For completeness, these earlier studies are briefly summarized in Section 3. More recently, the CX-100 blade was dynamically tested at the National Renewable Energy Laboratory (NREL) with large masses used to load the blade in bending. The added masses are represented in two alternative configurations, using (i) point masses and stiffening springs or (ii) high-fidelity solid elements. The ability of these competing strategies to replicate the experimentally obtained natural frequencies is discussed in Section 4. In Section 5, the fundamental principles behind IGDT are presented, and the extent to which predictions of these two competing models are robust to uncertainties in the model input parameters is quantified.

The strategy that implements high-fidelity solid elements is found to be both more accurate and robust compared to the strategy that uses point masses. The practical implication of these findings is that predictions, and their accuracy, can be trusted even if model input parameters upon which the solid-element FE model relies upon are uncertain. The vibration analysis of the FE model with three-dimensional solid elements is however significantly more expensive than the model with point masses. Another objective of the investigation is then to

understand the extent to which the point-mass model is able to deliver a similar accuracy and robustness as the solid-mass model, at lower computational cost.

4.2 Related Literature

As lack-of-knowledge arises in identifying an appropriate modeling strategy in almost every engineering application, model selection has been a widely pursued research topic [16]. In the last decade, methods rooted in the Bayes theorem have been widely pursued to select a model from a family of available models with techniques such as Bayes factor, Bayesian model averaging, and Bayesian linear models. Bayes factor compares the likelihood of two models, using a zero-one loss function for model selection [17]. Consideration of the Bayes factor has led to the Akaike information criterion and Bayesian information criterion, which evaluate models based on their maximized likelihood function and number of parameters using different weights on the latter component, thus providing a subjective choice that can affect results [18]. Bayesian model averaging compares the weighted average of the posterior probabilities each model under consideration [19], but is often difficult to solve due to the evaluation of complicated integrals, and is computationally expensive when a large number of models are under consideration. To rectify computing demands associated with Bayesian model averaging, Occam's window algorithm can be used to eliminate models, or Markov chain Monte Carlo algorithm can provide an approximation of the posterior probability. Bayesian linear models are formulated in the frequentist approach to incorporate prior information to find one or a few "best" models [20]. Despite the convenient framework offered by Bayesian approaches, it has been shown that the formulation of defensible priors is often difficult and can influence the model selection outcome [21]. Further, Bayesian strategies are often infeasible due to computational demands.

Non-Bayesian methods that depend on frequentist approaches have also been proposed for model selection. For example, cross-validation tests are used to compare the quality of models

using hold-out experimental data [22], which can be computationally prohibitive and sensitive to the implemented data-splitting techniques. To efficiently determine the parameters to use in a model, the backward elimination and forward selection methods use the F statistic to determine whether eliminating or adding parameters to the model provides an improvement, however, these methods were originally developed for variable selection and are not guaranteed to select the optimal model [23]. Regression statistics are also useful to compare models, but is unable to promote a fair comparison between models of different sizes. The C_p statistic mitigates this problem by using the residual sum of squares for a model and the error variance based on the full model for model subset selection [24]. It is important to note, however, that calibrating the model chosen with the C_p statistic can result in selection bias. Myung [10] compares the performance of several model selection techniques; with the conclusion that model complexity must be taken into account to ensure that an overly complex model is not selected. Robustness is able to account for the complexity of a model, because the effect of parameter variation provides a measure of the model complexity by evaluating how much the model degrades as uncertainty is exercised.

4.3 Model Development and Experimental Campaign

This section reviews the FE model development for the CX-100 blade closely following the in-depth discussions provided by Mollineaux et al. [14] and Van Buren et al. [15].

4.3.1 Development of the FE Model of CX-100 Wind Turbine Blade without Added Masses

The geometric model of CX-100 blade is built in NuMAD preprocessor [25] according to the accurate description of the design specifications, and imported into ANSYS version 12.1 with Shell-281 elements. The mesh discretization is based on an element size of $\Delta x = 8$ cm, which produces an overall solution uncertainty of 1.78% for the prediction of first three flapwise bending modes of the blade. This mesh size is justified by the fact that the resulting numerical

uncertainty is comparable to a 3-σ experimental variability of 1.62%, estimated from free-free modal testing performed at the Los Alamos National Laboratory (LANL) [26].

Six independent sections are defined in the development of the FE model: shear web, root, spar cap, trailing edge, leading edge with balsa, and leading edge without balsa wood. With the exception of the shear web, which it is located inside the cross-section of the blade, these sections are illustrated in Figure 4.1. Isotropic materials with smeared cross-sectional properties are used to define the material for these sections.

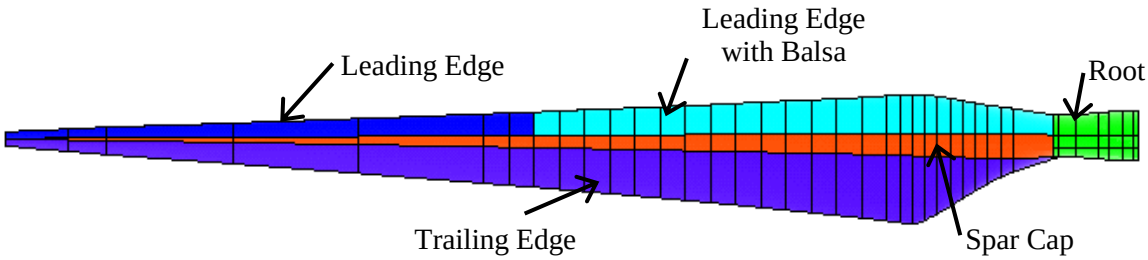

Figure 4.1: Illustration of the ANSYS model showing different sections of the blade.

Modal testing performed in two configurations at LANL is used for calibration and validation studies. These two configurations include free-free condition, where the blade is suspended with straps, and clamped-free condition, where a 250-kg steel bookend fixture is used to fix the base of the blade. The model parameters are calibrated to the free-free and clamped-free experimental natural frequencies in a two-step procedure [15]. To mitigate the uncertainty in the fixity at the base of the blade, fictitious springs are introduced and calibrated against the natural frequencies. The mode shape vectors are used to validate the FE model, in which the modal assurance criterion is estimated to quantify the agreement of simulation results to the experimental data. An overall correlation of 84% is observed for the free-free modes and 94% for the clamped-free modes.

4.3.2 NREL Modal Testing of the CX-100 Wind Turbine Blade

The CX-100 wind turbine blade is attached to a 6300 kg (7-ton) steel frame, effectively providing a fixed-free boundary condition. The boundary condition provided in the NREL testing is therefore different from that of the LANL testing discussed earlier in section 3.1 [15,26]. A 582-kg mass and 145-kg mass are added on the blade at the 1.60-meter and 6.75-meter locations, respectively. The significant mass loading in NREL testing supplies a different configuration of the CX-100 wind turbine blade.

Figure 4.2: Experimental fixed-free (left) configuration, mass-added (middle) configuration, and base fixture (right).

Modal testing is performed with a roving impact hammer test procedure under two different setups: first, in a fixed-free condition, and second, with large masses clamped to the blade. Four uni-axial accelerometers and one tri-axial accelerometer are used to collect data for hammer impacts at 65 locations: 47 in the flapwise directions, and 18 in the edgewise directions. Three test replicates are linearly averaged with 150 Hz sampling frequency. The acceleration response is collected with 4,096 sampling points without a window function due to the relatively

long sampling period of 11 seconds [27]. The experimental setups and base fixture are shown in Figure 4.2, and the first three flapwise frequencies are listed in Table 4.1.

Table 4.1: Results of the experimental modal analysis.

Mode	Fixed-Free Frequency (Hz)	Mass-Added Frequency (Hz)
1st Flap Bending	4.35	1.82
2nd Flap Bending	11.51	9.23
3rd Flap Bending	20.54	12.72

4.3.3 Fixed-free Model of the CX-100 Wind Turbine Blade

Calibration of the clamped-free model discussed earlier in section 3.1 is re-considered due to the more rigid structure used to support the blade in the NREL experiments. Five statistically significant parameters of the fixed-free FE model of the wind turbine blade are identified through sensitivity analysis. The influential parameters are: density of the trailing edge, the leading edge, and the spar cap, modulus of elasticity of the spar cap, translational springs used to model the boundary condition perpendicular to the base fixity.

An exploratory design-of-experiments reveal that for the FE model to envelope the experimental data, the uncertainty bounds of the density of the trailing edge, density of the leading edge, density of the spar cap are allowed to vary within ±50% bounds of the nominal value. When the densities are allowed to vary past these values, modes are observed to swap. The upper and lower uncertainty bounds chosen for the spar cap modulus reflect the posterior uncertainty obtained from previous free-free calibration [15]. The uncertainty bounds of boundary springs are determined from parametric studies of the fixed-free boundary condition.

Measured natural frequencies of the NREL testing are utilized to calibrate the FE model. Instead of performing calibration as an optimization of model parameters to best-fit the experimental data, inference uncertainty quantification is performed to explore the posterior

probability distribution of these three parameters. To efficiently perform the inference uncertainty quantification, a fast-running Gaussian Process Model (GPM) emulator is trained using three-level, full-factorial design-of-experiments [28]. A Metropolis-Hastings Markov Chain Monte Carlo (MCMC) algorithm [29,30] is used to explore the posterior distribution of parameters for the GPM emulator, retaining only parameters that provide frequency predictions that better replicate experiments. This methodology relies on the theory proposed by Kennedy and O'Hagan [31] and the computational framework developed by Higdon et al. [32].

Table 4.2: Comparison of prior and posterior uncertainty of the FE model parameters.

FE Model Parameter	Prior Uncertainty			Posterior Uncertainty		
	Lower	Upper	Range	Mean	Std. Dev.	±2σ Range
Trailing Edge, density	274.60	823.80	549.20	335.62	49.49	197.95
Leading Edge, density	858.20	2574.60	1716.40	1165.30	248.76	995.03
Spar, modulus	29.92	53.56	23.64	43.40	5.51	22.05
Z-spring	1.00	100.00	99.00	71.91	15.98	63.91
Spar, density	1267.00	3801.00	2534.00	1673.57	335.74	1342.94

The results of the inference are summarized in Table 4.2. Columns 2-4 summarize the prior uncertainty, which represents the range of values used in the full-factorial design to train the GPMs. Columns 5-7 provide the posterior uncertainty, which are the statistics inferred via the MCMC search algorithm. The inference is successful at updating the value of the parameters, as indicated by the reduction of the parameter uncertainty relative to the prior distributions.

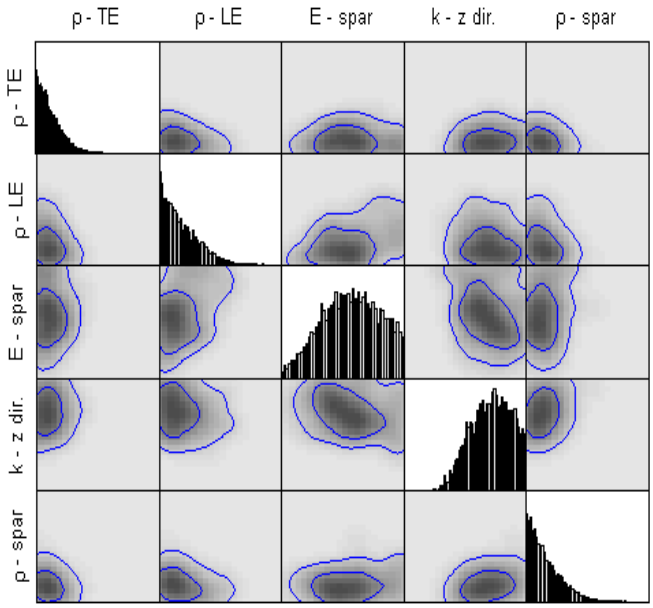

Figure 4.3: Marginal distributions and correlation functions corresponding to Table 4.2.

Table 4.3 compares the experimentally obtained natural frequencies to those predicted by the FE model with the parameters set to the mean values of the posterior distribution. The simulation consistently under-predicts the experimental results by 0.5-3.4%. Due to the relatively small error in the predictions of resonant frequencies, and the fact that the predicted mode shape deflections correlate well with those measured experimentally, the accuracy of the calibrated fixed-free model is deemed acceptable. The FE model with the mean values of the posterior distributions is used in the next section to explore the mass-added configuration.

Table 4.3: Comparison of experimental and simulated results for the fixed-free model.

Mode	Experimental (Hz)	Simulated (Hz)	Difference (%)
1st Flap	4.35	4.26	-2.1%
2nd Flap	11.51	11.45	-0.5%
3rd Flap	20.54	19.85	-3.4%

4.4 Development of the FE Model of CX-100 Wind Turbine Blade with Added Masses

The FE models of the CX-100 wind turbine blade with added masses are developed using the fixed-free model discussed in Section 3.3. The two models pursued in this section are developed with different assumptions and simplifications using (i) a system of fictitious point masses and stiffening springs, and (ii) three-dimensional solid elements that represent the geometry of the added masses with high fidelity.

4.4.1 Development of the Point Mass Model

A point mass is added to the centroid of the cross section of the shell model of the CX-100 wind turbine blade to approximate the added masses at the two locations using Mass-21 elements in ANSYS. The point masses are then connected by fictitious springs, using Combin-14 elements, to the nodes of the blade to reflect the interaction between the blade and added masses as shown in Figure 4.4. The use of spring is necessary as the point masses connected directly to the shell model introduce lower-order mode shapes with local deformations at the cross-sections. This modeling strategy therefore, offers a compromise between low computational times-to-solution and an approximate representation of the vibration mechanics. The parameterization of this simplified modeling strategy results in the use of only six new model parameters (Table 4.4).

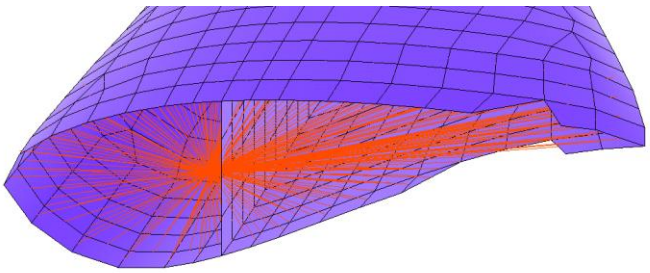

Figure 4.4: Illustration of the blade cross-section with added point masses and springs.

Table 4.4: Parameters used to develop the point mass representation.

Parameter	Description
(1; 2)	(Translation; rotation) springs at the 1.60-meter section
3	Point mass at 1.60-meter section
(4; 5)	(Translation; rotation) springs at 6.75-meter section
6	Point mass at 6.75-meter section

In this modeling strategy, the parameter values used for the point masses (parameters 3 and 6) correspond to the measured weights. However, the parameter values of the springs (parameters 1, 2, 4, and 5) are highly uncertain and thus, need to be calibrated. To determine the values to use for the spring stiffness constants, a parametric study is performed to evaluate the effect of the spring stiffness on frequency predictions.

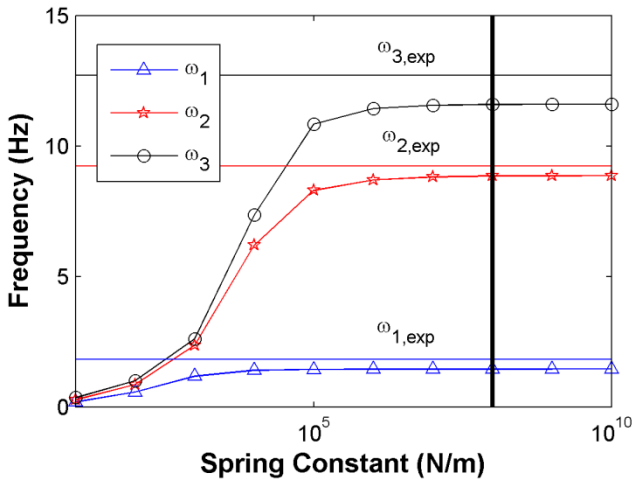

Figure 4.5: Effect of spring stiffness coefficients on the first three bending frequencies.

Figure 4.5 shows the frequency predictions as the spring stiffness values are varied from 10 to 10^{+10} N/m. As the spring stiffness is increased, the natural frequencies also increase, due to the change in interaction between the blade and point masses. Around a value of 10^{+6} N/m, the

natural frequencies begin to plateau to values that consistently under-predict the experimental natural frequencies, indicated by the solid horizontal lines in Figure 4.5. A calibration of the model parameters would therefore, converge to the upper bound of the spring stiffness values as the FE model with point masses is unable to form an envelope around the experimentally obtained natural frequencies (Figure 4.5). Therefore, the value of 10^{+8} N/m is chosen for the spring stiffness, indicated by the vertical black line in Figure 4.5.

Table 4.5: Comparison of experimental and simulated frequencies for the mass-added model.

Mode	Experimental (Hz)	Simulated (Hz)	Difference (%)
1st Flap	1.82	1.45	-20.3%
2nd Flap	9.23	8.85	-4.1%
3rd Flap	12.72	11.59	-8.9%

Table 4.5 compares the natural frequencies measured experimentally to those predicted by the mass-added FE model. Again, the frequencies are consistently under-predicted by the model, due to the minimal calibration activities performed after the model was modified to include the added masses.

4.4.2 Development of the Solid Mass Model

The second modeling strategy is to represent the added-mass configuration of the blade with a higher degree of geometrical fidelity. Three-dimensional, solid elements are utilized to represent the geometry of the experimental setup, implementing Solid-186 elements in ANSYS. Four sections are used to define the added masses. The sections are labeled as the 6.75-meter mass, 1.60-meter mass, and two 1.60-meter offset masses in Figure 4.6.

Four sections are used to model the added masses onto the blade, as shown in Figure 4.6: one section for the wooden form attached to the blade at the 1.60-meter station, two symmetric

sections for the hydraulic actuator system at the 1.60-meter station, and one section for the wooden form attached to the blade at the 6.75-meter station. The wooden forms are modeled using the geometry of the masses obtained from design specifications. The geometry of offset masses of the hydraulic actuator system at the 1.60-meter station is simplified into homogenous rectangular solids, thus providing a more accurate description of reality than the point mass model. A comparison of the experimental configuration and finite element modeling of the offset masses is provided in Figure 4.7.

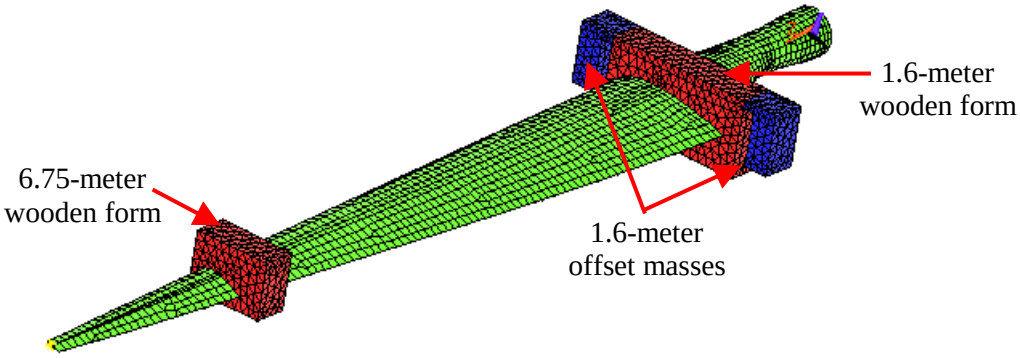

Figure 4.6: Second modeling strategy that includes solid elements to represent the added masses.

The parameters used to develop the solid-mass representation are listed in Table 4.6. The parameterization includes the geometry of the outset masses, represented by the center of gravity coordinates that define the masses, which influences the ability of the blade to bend in torsion. The imperfect knowledge of these parameters introduces parametric uncertainty in the prediction of vibration response. Moreover, the imperfect knowledge of the center of gravity coordinates also introduces numerical uncertainty as the mesh changes each time that a different location of

the center of gravity is implemented. The re-meshing step in the propagation of uncertainties significantly increases the computational cost of the analysis.

Table 4.6: Parameters used to develop the solid-mass representation.

Parameter	Description
(1; 2)	(Elastic modulus; density) of 1.60-meter section
(3; 4)	Center of gravity (X; Y) coordinates of 1.60-meter offset mass
5	Density of 1.60-meter offset section
(6; 7)	(Elastic modulus; density) of 6.75-meter section

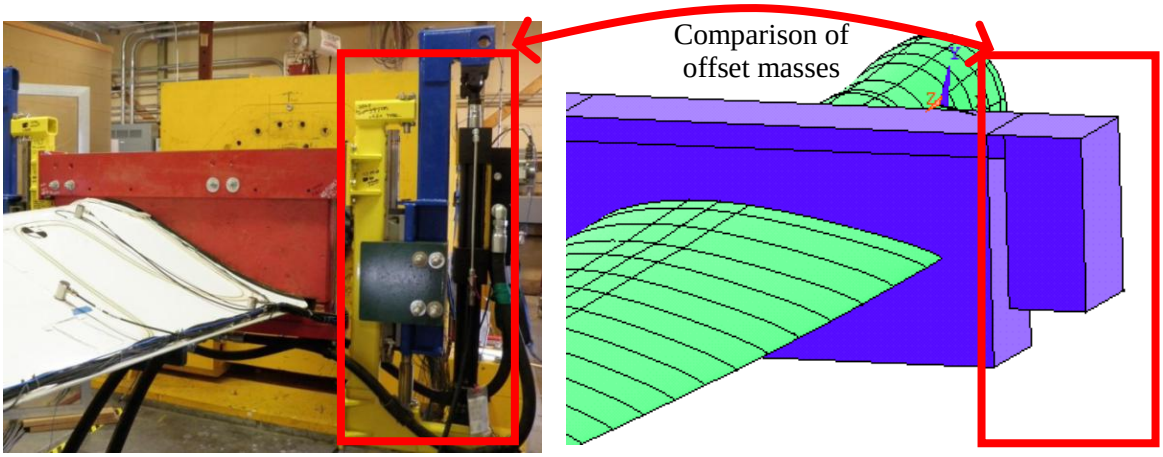

Figure 4.7: Close-up of the offset mass modeled at the 1.60-meter station.

With the masses represented using solid elements, the density is back-calculated such that the weights of masses implemented in the FE model correspond to the weights of masses obtained experimentally. The elastic modulus of the wooden forms is assumed based on the documented value for balsa wood. The agreement between predictions of the FE model and experimental measurements is listed in Table 4.7.

Table 4.7: Comparison of experimental and simulated frequencies for the solid-mass model.

Mode	Experimental Frequency (Hz)	Simulated Frequency (Hz)	Difference (%)
1st Flap	1.82	1.44	-20.9%
2nd Flap	9.23	9.29	0.7%
3rd Flap	12.72	13.22	3.9%

4.5 Analysis of Robustness to Uncertainty Applied to Models of the CX-100 Wind Turbine Blade

This section discusses the conceptual framework and implementation of IGDT to evaluate the robustness to uncertainty of model predictions. By establishing robustness, we demonstrate the extent to which the predictions remain *sufficiently* accurate, even if modeling assumptions and parameter values used in the simulation are incorrect. On the other hand, lack-of-robustness indicates that the expected level of accuracy obtained, for example, through calibration, may not be maintained if the assumptions and parameter values happen to be incorrect. Ensuring the robustness of the FE model does not necessarily translate into a reduction of prediction uncertainty. Instead, robustness analysis aims to identify a potentially alarming situation whereby the predictions, and their accuracy, are sensitive to aspects of the modeling that may be unknown and/or uncontrolled.

4.5.1 Conceptual Demonstration of Robustness Analysis

For the info-gap analysis presented, the allowable range of variation of model parameters is controlled using an uncertainty parameter, α. For simplicity, the definition of α is kept unit-less, therefore the same level of uncertainty, α, can be applied simultaneously to multiple parameters of the two modeling strategies. The second attribute of the info-gap analysis is the performance metric of the model, herein quantified by the fidelity-to-data using the root mean squared difference between simulation predictions and experimental observations. In the following

paragraphs, a conceptual illustration is provided with a unit-less α and fidelity based performance metric to describe the evaluation of the robustness of the competing FE models to the uncertainty in their corresponding model input parameters.

Consider a model defined using two uncertain parameters, u_1 and u_2. Figure 4.8-a describes the nominal performance of the model, where u_1 and u_2 are defined using initial, best guesses or nominal values. As uncertainty, α, is increased, the parameters are allowed to vary within a range of permissible values (see Section 4.2 for how the bounds are chosen for the parameters in our application). As a result, parameters are varied from their nominal settings to become $\tilde{u}_1$ and $\tilde{u}_2$. Herein, the allowable range of variation of $\tilde{u}_1$ and $\tilde{u}_2$ is referred to as the uncertainty space. It is represented as a two-dimensional rectangle of size $(\alpha_1)^2$ in Figures 4.8-b and 4.8-c. With such changes in input parameters, the model performance either improves or degrades. IGDT, therefore, explores the best and worst achievable performances as $\tilde{u}_1$ and $\tilde{u}_2$ are allowed to venture away from their nominal values but remain within the uncertainty space defined by the parameter α_1. The improvement of the performance obtained from the model is described as the opportuneness, and the degradation of performance is the robustness. At any level of uncertainty α, the opportuneness and robustness points are obtained by solving two global optimization problems that search for the best and worst performances, respectively within the space of allowable values for $\tilde{u}_1$ and $\tilde{u}_2$. Figures 4.8-b and 4.8-c illustrate the development of the robustness and opportuneness functions.

4.8-a. Analysis of nominal performance.

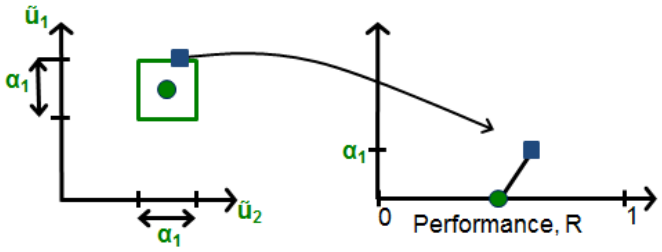

4.8-b. Development of the robustness function.

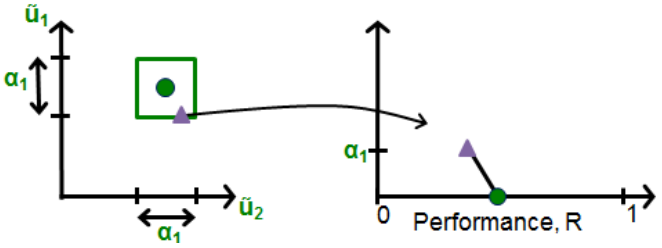

4.8-c. Development of the opportuneness function.

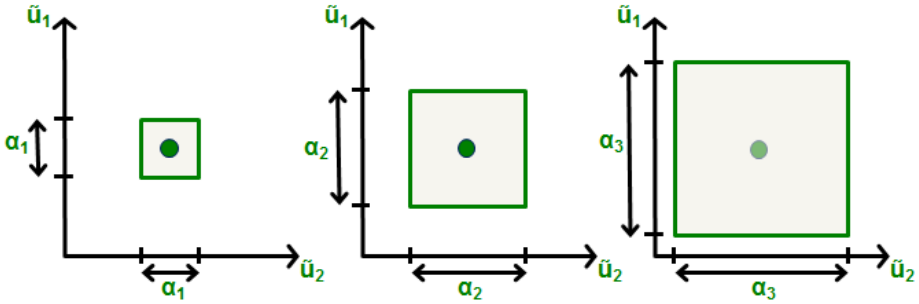

4.8-d. Increased uncertainty space for $\alpha_3 \geq \alpha_2 \geq \alpha_1$.

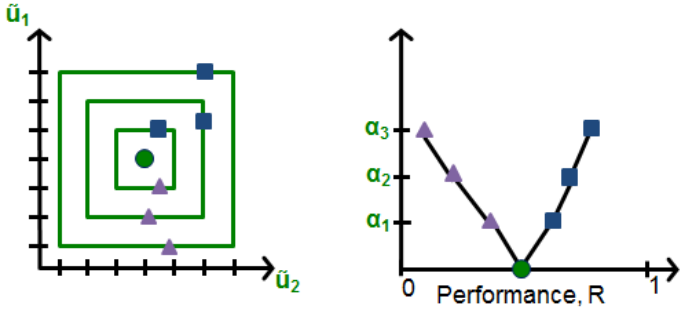

4.8-e. Robustness and opportuneness curves.

Figure 4.8: Illustration of the successive steps of an info-gap analysis of robustness.

If the uncertainty space is defined to have nested intervals for increasing values of α, as suggested in Figure 4.8-d, then the opportuneness and robustness curves will be monotonic functions since the global optimizations are performed within ever-growing spaces. Figure 4.8-e

then shows the resulting opportuneness and robustness curves, developed from the evaluation of best and worst performances at three levels of uncertainty. A particular focus is placed on the robustness curve, and its slope "$\Delta\alpha/\Delta R$", which is useful to evaluate the worst-case performance of the model under increasing uncertainty bounds. A "steep" robustness curve indicates that as the uncertainty is allowed to increase, "$\Delta\alpha$," the accompanying model predictions remain consistent, resulting in a small change in model performance, "ΔR." Such an observation would be welcome as it would reinforce our conviction that the model can be applied with confidence even if the model parameters used for its development are questionable. On the other hand, a robustness curve with small slope, which denotes a small increase in uncertainty "$\Delta\alpha$" relative to a change in performance "ΔR," indicates that the model predictions are sensitive to the values of $\tilde{u}_1$ and $\tilde{u}_2$ used in the simulation. Such a lack of robustness would decrease the level of trust placed in the model input values upon which the model relies.

4.5.2 Rationale for the Definition of Uncertainty

The input parameters are varied in such a way that the effect on bending frequency predictions of the maximum parameter variation is consistent with the difference between the competing models at their nominal setting. Doing so ensures that the effect on predictions of the allowable range of parameter variation is consistent with the effect on predictions of varying the model forms of the competing modeling strategies. Herein, model selection is only concerned with the way in which the masses are modeled onto the existing shell representation thus; the info-gap analysis is restricted to the model parameters used to define the added masses.

The two models at their nominal configuration exhibit a 20% average percent variation in the first three flapwise frequencies. Only the common parameters between the two models, i.e. weights of the masses, are considered in order to demonstrate how each model is affected by varying the *same* modeling component. The models are held at their nominal configuration while

the masses are allowed to vary using the mass parameter for the point mass model, and the density parameter for the solid mass model.

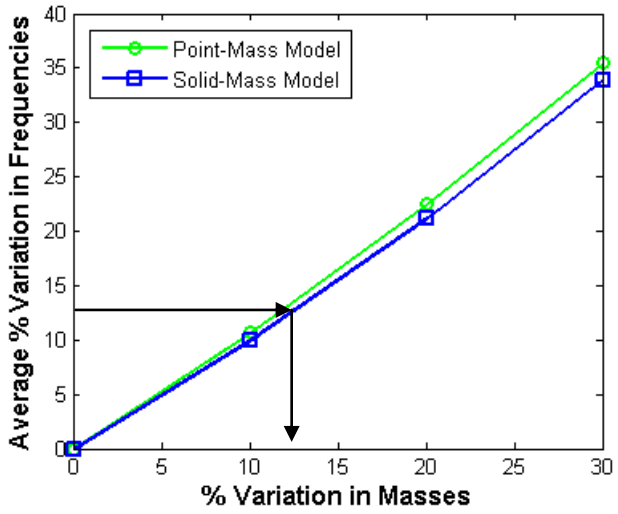

Figure 4.9: Comparison of frequency prediction variation due to mass-only variation.

The average percent variations of predictions obtained by varying the masses are plotted in Figure 4.9. The observed difference between behaviors of the two curves can be attributed to the combined effect of parameter variation and model form on frequency predictions. Figure 4.9 demonstrates that an approximately 20% variation in masses is necessary to achieve the 20% variation observed between the two models at nominal configuration. Thus, the lower and upper bounds of the variation corresponding to $\alpha = 1$ are defined to allow the mass parameters to vary up to ± 20%. Similar prescriptions for the bounds of uncertainty are applied to the remaining parameters, such that each level of alpha corresponds to a uniform level of parameter uncertainty. Having defined the parameter variations corresponding to any value of α, the info-gap analysis can be used to address the question of model selection.

4.5.3 Selection of the Mass Added Models

In the info-gap analysis, the uncertainty space is a hyper-cube defined from the lower and upper bounds for the vector of parameters $\tilde{u}$. The parameters considered in the info gap analysis are the unit masses and stiffening springs for the point mass model, and the material properties and x,y coordinates of the offset masses for the solid mass model (see Tables 4.4 and 4.6). The size of the uncertainty space increases monotonically depending on the level of uncertainty considered, α:

$$\tilde{u}(\alpha) = (1 \pm 0.2 \times \alpha)\, u. \tag{1}$$

The robustness and opportuneness functions are evaluated in increments of α = 0.5 according to Equation 1. Note that α is multiplied by 0.2, to accommodate a 20% variation in parameters when α=1. For each level of uncertainty evaluated, the fmincon optimization solver of Matlab™ is used to search for the set of parameters that produces the worst-case and best-case performance within the family of all possible models, for robustness or opportuneness, respectively. A two-level full-factorial design of experiments is evaluated before initiating the optimization routine. The optimization is then initiated using the combination of model parameters that yields the maximum or minimum performance of the full-factorial design. Doing so increases confidence that the optimization is initiated close to the global solution, such that the fmincon algorithm can avoid getting trapped in a local maxima or minima.

A new input deck, that includes re-meshing in the case of the solid element model, is generated and submitted to ANSYS each time that a combination of model parameters is evaluated during the optimization. Results of the ANSYS analysis are then be uploaded in Matlab™ memory. This strategy requires significant computational resources, but avoids the development of statistical emulators that may introduce unwanted approximations.

Model performance is defined as the root mean squared error of natural frequencies for the first three flapwise bending modes:

$$R = \sqrt{\sum_{i=1}^{3}\left(\omega_{sim,i} - \omega_{\exp,i}\right)^2}, \qquad (2)$$

where R denotes the model performance metric, ω_{sim} and ω_{exp} are the numerical prediction and experimental measurement of natural frequencies.

Table 4.8: Range of variation for the parameters used in the point-mass model.

Parameter	Description	Nominal Value	± Variation
1	Translation springs at 1.60-meter section	10^{+8}	$10^{+6.4} – 10^{+9.6}$
2	Rotation springs at 1.60-meter section	10^{+8}	$10^{+6.4} – 10^{+9.6}$
3	Point mass at 1.60-meter section	582.46	465.97 – 698.95
4	Translation springs at 6.75-meter section	10^{+8}	$10^{+6.4} – 10^{+9.6}$
5	Rotation springs at 6.75-meter section	10^{+8}	$10^{+6.4} – 10^{+9.6}$
6	Point mass at 6.75-meter section	144.7	115.76 – 173.64

Tables 4.8 and 4.9 define the parameters associated with the competing models, along with the ranges of variation specified for the info-gap analysis at the level of uncertainty of $\alpha = 1$. Note that the center of gravity parameter in Table 4.10 affects the mesh definition in the solid mass representation. Thus, in the FE model with solid masses, the uncertainty parameter, α, influences both the material behavior (density, elastic modulus) and numerical uncertainty of FE predictions.

Table 4.9: Range of variation for the parameters used in the solid-mass model.

Parameter	Description	Nominal Value	± Variation
1	Elastic modulus of 1.60-meter section	$8\times10^{+9}$	$6.4\times10^{+9} – 9.6\times10^{+9}$
2	Density of 1.60-meter section	636.1	508.88 – 763.32
3	Center of gravity X coord. of 1.60-meter offset mass	0.224	0.179 – 0.269
4	Center of gravity Y coord. of 1.60-meter offset mass	0.480	0.384 – 0.576
5	Density of 1.60-meter offset section.	229.0	183.2 – 274.8
6	Elastic modulus of 6.75-meter section	$8\times10^{+9}$	$6.4\times10^{+9} – 9.6\times10^{+9}$
7	Density of 6.75-meter section	1644.5	1315.6 – 1973.4

Figure 4.10 presents the results of the info-gap analysis performed on the competing FE models. The nominal performance, associated with a level of uncertainty of $\alpha = 0$, clearly demonstrates that the solid mass model better reproduces the experimental data compared to the point mass model. Further, as the uncertainty parameter increases, the solid mass model remains the preferable modeling strategy. It can be stated that the solid mass model provides a higher degree of accuracy at any level of modeling uncertainty, α. In fact, the robustness slopes of the competing models are comparable despite the different representations of reality. The result of this analysis demonstrates unambiguously that the solid mass model is the preferable modeling strategy to utilize, despite the lack-of-knowledge associated with the modeling assumptions and parameters used in the simulation.

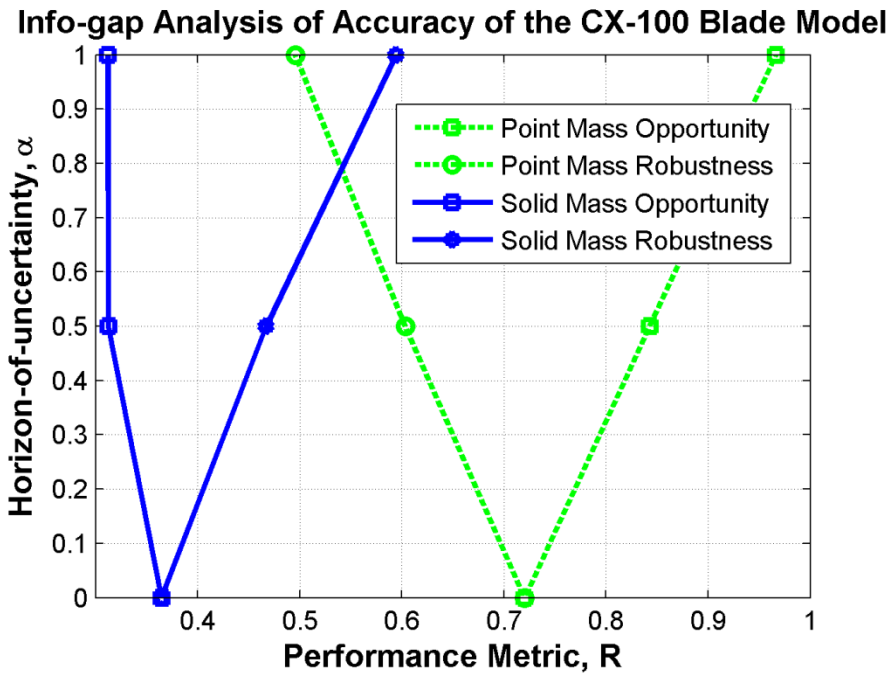

Figure 4.10: Info-gap robustness and opportuneness curves of the two modeling strategies.

Figure 4.11 combines the results in Figure 4.10 to provide the range of predictions that are obtained at each level of uncertainty. The difference in behavior of the two curves is due to both the varied parameter values, and the model forms that are employed by the competing modeling strategies. The solid mass model is able to provide a smaller range of predictions as uncertainty, α, is increased. Again, the solid mass model is superior to the point mass model, due to the fact that the predictions for the solid mass model deviate less than the point mass model as uncertainty is accounted for.

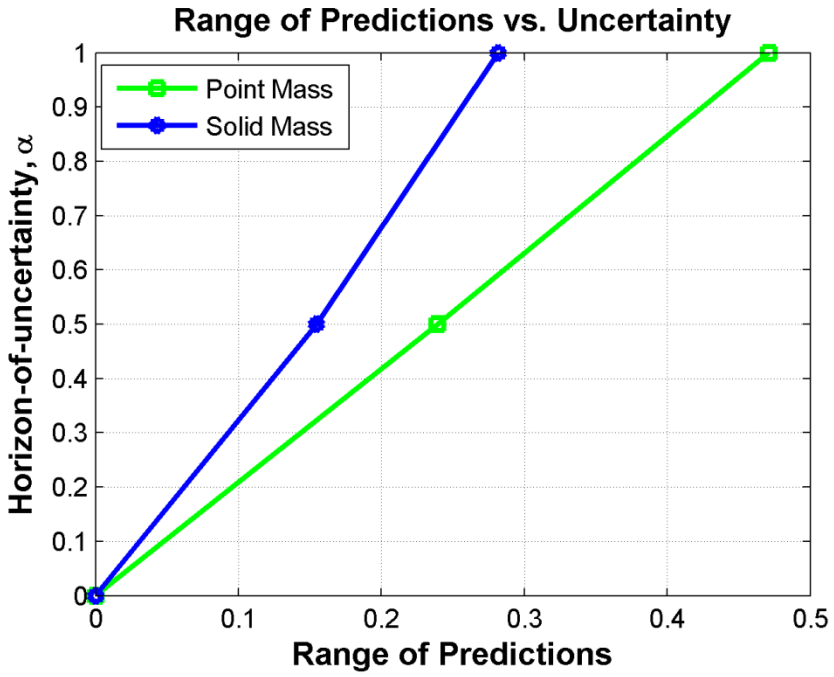

Figure 4.11: Range of predictions of the two modeling strategies.

4.6 Conclusion

This manuscript discusses a decision analysis methodology for model selection that considers the trade-offs in the ability of a numerical simulation to, first, replicate the experimental data and, second, provide predictions that are robust to the uncertainties in model input parameters. Understanding the trade-offs between fidelity and robustness is important for the

development of numerical models because it is the very mechanism through which the trustworthiness of predictions can be established.

Modeling assumptions are typically formulated when developing numerical simulations, such as the use of fictitious boundary springs or implementing smeared properties for composite materials instead of attempting to define the individual layers. Although such assumptions have become commonplace, their effect on model predictions often remains unknown. Another common practice is to consider that a model achieves sufficient "predictability" as long as its predictions reproduce the experimental measurements. Our contention is that assessing models based only on their fidelity-to-data while ignoring the effect that the modeling assumptions may exercise on predictions is not a sound strategy for model selection.

The methodology discussed in this study is applied to competing models used to simulate an experimental configuration of the CX-100 wind turbine blade in which masses are added to the blade. Experimental data obtained from a fixed-free modal analysis performed at the National Renewable Energy Laboratory, with and without added masses, are utilized. The wind turbine blade is bolted to a 6300-kg steel frame to define the fixed-free configuration. Masses are added at the 1.60-meter and 6.75-meter sections to define the mass added configuration that enhances the flapwise bending vibrations. The FE model of the blade, developed from a previous verification and validation study, is first calibrated to measurements of the fixed-free configuration. Calibration results show that the FE model is able to replicate the experimental frequencies within an average 2% error. Two modeling strategies are then considered for implementing the masses onto the existing FE model, using (i) point masses and stiffening springs and (ii) high-fidelity solid elements. To examine the predictive capability of the mass-added FE models, limited calibration exercises are performed past the initial calibration to the fixed-free configuration. At their nominal configurations, the point mass model reproduces the

experimental data to within 11.1% average error, and the solid mass model is within 8.5% average error for the first three flapwise bending natural frequencies.

An info-gap analysis is performed to address the question of model selection. An advantage of info-gap is that the formulation of prior probability distributions can be avoided because the analysis substitutes numerical optimization to statistical sampling. Further, the robustness to our lack-of-knowledge about the modeling assumptions and parameter values is accounted for when evaluating the model performance. The info-gap analysis is performed through parameter variation, where the maximum range of variation is chosen such that the change in model predictions is consistent with the change induced by the differing modeling strategies. It is observed that the solid mass model is not only more accurate, but also provides better behavior in robustness to modeling assumptions and unknown parameter values. Even though the solid mass model is a more complex representation of reality, and comes with higher computational cost, the analysis concludes unambiguously that it is the preferable modeling strategy for this application.

References

[1] D.T. Griffith, T.D. Ashwill, The Sandia 100-meter all-glass baseline wind turbine blade: SNL100-00, Sandia Technical Report SAND2011-3779, Sandia National Laboratories, Albuquerque, NM, 2011.

[2] D.C. Quarton, The evolution of wind turbine design analysis: A twenty year progress review, Wind Energy, 1 (1998) 5-24.

[3] P.S. Veers, D.L. Laird, T.G. Carne, M.J. Sagartz, Estimation of uncertain material parameters using modal test data, 36th AIAA Aerospace Sciences Meeting, 1998.

[4] Det Norske Veritas, Design and Manufacture of Wind Turbine Blades, Offshore and Onshore Wind Turbines, October 2010.

[5] F.M Jensen, B.G. Falzon, J. Ankersen, H. Stang, Structural testing and numerical simulation of a 34-m composite wind turbine blade, Composite Structures, 76 (2006) 52-61.

[6] J.G. Leishman, Challenges in modeling the unsteady aerodynamics of wind turbines, Wind Energy, 5 (2002) 85-132.

[7] G. Freebury, W. Musial, Determining equivalent damage loading for full-scale wind turbine blade fatigue tests, 19th ASME Wind Energy Symposium, 2000.

[8] S. Dalton, L. Monahan, I. Stevenson, D.J. Luscher, G. Park, K. Farinholt, Towards the Experimental Assessment of NLBeam for Modeling Large Deformation Structural Dynamics, in: R. Mayes, D. Rixen, D.T. Griffith, D. DeKlerk, S. Chauhan, S.N. Voormeeren, M.S. Allen (Eds.), Topics in Experimental Dynamics Substructuring and Wind Turbine Dynamics, Volume 2, Springer, New York, NY, 2012, pp. 177-192.

[9] M. Martins, A. Perdana, P. Ledesma, E. Agneholm, O. Carlson, Validation of fixed speed wind turbine dynamic models with measured data, Renewable Energy, 32 (2007) 1301-1316.

[10] J. Myung, The importance of complexity in model selection, Journal of Mathematical Psychology, 44 (2000) 190-204.

[11] S. Atamturktur, J. Hegenderfer, B. Williams, M. Egeberg, C. Unal, A resource allocation framework for experiment-based validation of numerical models, Journal of Mechanics of Advanced Materials and Structures, (2012) conditionally accepted.

[12] Y. Ben-Haim, F.M. Hemez, Robustness, fidelity and prediction-looseness of models, Proceedings of the Royal Society A 468 (2012) 227-244.

[13] Y. Ben-Haim, Info-Gap Decision Theory: Decisions Under Severe Uncertainty, second ed., Oxford, 2006.

[14] M.G. Mollineaux, K.L. Van Buren, F.M. Hemez, S. Atamturktur, Simulating the dynamics of wind turbine blades: Part I, model development and verification, Wind Energy, 2012. (DOI: 10.1002/we.1521.)

[15] K.L. Van Buren, M.G. Mollineaux, F.M. Hemez, S. Atamturktur, Simulating the dynamics of wind turbine blades: Part II, model validation and uncertainty quantification, Wind Energy, 2012. (DOI: 10.100/we1522.)

[16] D. Draper, Assesment and propagation of model uncertainty, Journal of the Royal Statistical Society, Series B, 57 (1995) 45-97.

[17] J.B. Kadane, J.M. Dickey, Bayesian Decision Theory and the Simplification of Models, in: J. Kmenta , J. Ramsey (Eds.) Evaluation of Econometric Models, Academic Press, New York, NY, 1980, pp. 245-268.

[18] H. Bozdogan, Akaike information criterion and recent developments in information complexity, Journal of Mathematical Psychology, 44 (2000) 62-91.

[19] L. Wasserman, Bayesian model selection and model averaging, Journal of Mathematical Psychology, 44 (2000) 92-107.

[20] J.O. Berger, L.R. Pericchi, Objective Bayesian Methods for Model Selection: Introduction and Comparison (with discussion), in: P. Lahiri (Ed.), Model Selection, IMS, Beachwood, OH, 2001, pp. 135-207.

[21] J.B. Kadane, N.A. Lazar, Methods and criteria for model selection, Journal of the American Statistical Association, 99 (2004) 279-290.

[22] S. Arlot, A. Celisse, A survey of cross-validation procedures for model selection, Statistics Survey, 4 (2010) 40-79.

[23] S. Derksen, H.J. Keselman, Backward, forward and stepwise automated subset selection algorithms: frequency of obtaining authentic and noise variables, British Journal of Mathematical and Statistical Psychology, 45 (1992) 265-282.

[24] C.L. Mallows, Some comments on C_p, Technometrics, 15 (1973) 661-675.

[25] D.L. Laird, NuMAD User's Manual, SAND2001-2375, Sandia National Laboratories, Albuquerque, NM, 2001.

[26] K. Deines, T. Marinone, R. Schultz, K. Farinholt, G. Park, Modal Analysis and Structural Health Monitoring Investigation of CX-100 Wind Turbine Blade, in: T. Proulx (Ed.), Rotating Machinery, Structural Health Monitoring, Shock and Vibration, Volume 5, Springer, New York, NY, 2011, pp. 413-438.

[27] K. Farinholt, S.G. Taylor, G. Park, C.M. Ammerman, Full-scale fatigue tests of CX-100 wind turbine blades: Part I – testing, SPIE Proceedings, 2012.

[28] L.S. Bastos, A. O'Hagan, Diagnostics for gaussian process emulators, Technometrics, 51 (2009) 425-438.

[29] N. Metropolis, A. Rosenbluth, A. Teller, E. Teller, Equations of state calculations by fast computing machines, Journal of Computing Physics, 21 (1953) 1087-1093.

[30] W.K. Hastings, Monte Carlo sampling methods using Markov chains and their applications, Biometrika, 57 (1970) 97-109.

[31] M. Kennedy, A. O'Hagan, Predicting the output from a complex computer code when fast approximations are available, Bimetrika, 87 (2000) 1-13.

[32] D. Higdon, J. Gattiker, B. Williams, M. Rightley, Computer model calibration using high-dimensional output, Journal of the American Statistical Association, 103 (2008) 570-583.

CHAPTER FIVE

ASSESSING THE TRADE-OFFS OF FIDELITY, ROBUSTNESS, AND SELF-CONSISTENCY FOR MODEL PARAMETER IDENTIFICATION

5.1 Introduction

Wind energy is being pursued as a viable source of energy in the U.S., due to its potential to supply 20% of the nation's energy needs by 2030 [1]. To meet these demands, wind turbine production in the U.S. has expanded from rotors with a diameter of 18 meters in 1985 to 120 meters in 2007 [2]. To better understand the performance of wind turbines produced at this massive scale, modeling and simulation (M&S) techniques are being implemented at an increasing rate. M&S has been demonstrated to be a useful tool to economically study the performance of individual wind turbine blades, such as the tip deflection [3], failure [4, 5], and interaction with wind loading [6]. However, to facilitate the expansion of wind turbine plants [7], optimize power output [8], and minimize fatigue failure [9], it is necessary to study the performance of wind turbines at the plant scale. Plant scale simulations can be achieved by coupling structural dynamics models of wind turbines with computational fluid dynamics (CFD) models of the surrounding airflow. Such coupled simulations are severely challenged by computational demands, which can be alleviated by the use of one-dimensional (1-D) structural finite element (FE) models. *NLBeam*, one such 1-D nonlinear beam code, offers the capability to simulate the structural dynamics response of wind turbines at low computational cost [10]. Figure 5.1 shows the usefulness of NLBeam in incorporating a realistic representation of wind turbine elastodynamics with *WindBlade*, CFD model of atmospheric hydrodynamics at the plant scale [11].

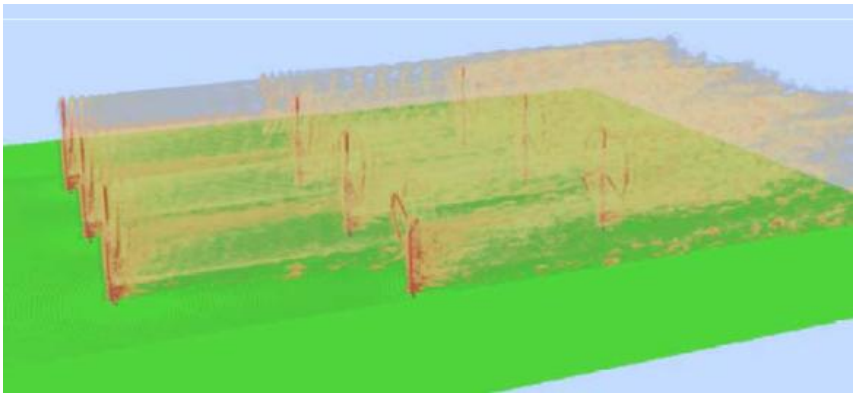

Figure 5.1: WindBlade model of a hypothetical wind plant [11].

The limitation of numerical modeling to analyze the performance of wind plants must be emphasized: only through rigorous verification, calibration and validation exercises can models be used defensibly in a predictive capacity. This is important for numerical models of wind turbine blades, where experimental modal analysis has been heavily pursued to provide evidence for calibration of models that are used to predict in-service performance [12]. Figure 5.2 depicts this paradigm, where a model is used to predict the response of configuration[2] "A," which is

[2] Here, "configuration" and "response" describe the general development and output of a finite element model. Configuration is used to describe the boundary conditions, loading conditions, material properties, and mesh continuity. Here, the material properties and mesh continuity can change from configuration "A" to "C" to reflect changes in temperature, or to model the onset of damage. Response is used to describe the output of the model used to quantify the performance of the model.

costly or impossible to experimentally measure (such as in-service performance of wind turbines). Here, experimental data is only available for response at configuration "B," which can be used to calibrate the model (such as experimental modal data). While calibration allows the models to provide a better test-analysis correlation, it may also provide a false sense of confidence in predictions, since the ability of the model to predict at other configurations remains unknown [13]. Therefore, it is important to validate the predictive ability of the model after calibration. Once the model has been calibrated to replicate experiments for configuration "B," it can be executed to predict the performance for an independent experiment, i.e. configuration "C." If the model is capable of predicting the response at configuration "C" with sufficient accuracy without further calibration, then the model is commonly considered validated. The validated model is used in a *predictive capacity*, for the response at untested configuration "A," as shown in Figure 5.2. Note that the experimental response at configuration "A" is unavailable, providing a nearly impossible platform to definitively confirm the accuracy of predictions at configuration "A."

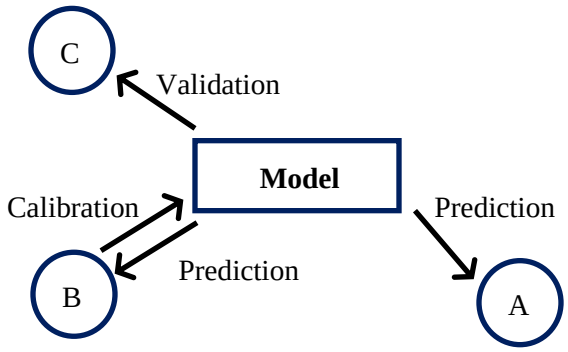

Figure 5.2: FE Model Calibration Process

The model calibration process discussed above can lead to non-uniqueness issues, where different combinations of calibration parameters can reproduce experimental data. This non-uniqueness constitutes an uncertainty in determining which combination of calibration parameters

should be used to define the model. Recent studies have proposed calibration methods to develop models that exhibit *robust fidelity* by considering the trade-offs in the fidelity to data and robustness to uncertainty of model parameters [14, 15, 16, 17]. Models that exhibit robustness to uncertainty contain solutions that remain consistent when variations are exercised to express uncertainty in the calibration parameters of the model. Due to the difficulty in developing reliable probability models of input parameters, non-probabilistic methods are preferable to study robustness. Info-gap decision theory (IGDT) has been introduced as a convenient non-probabilistic method to study robustness of model predictions against uncertainty [18]. IGDT has proven useful to study robustness to uncertainty in structural design [19], and industrial applications [20].

Though the ability of numerical models to re-create experimental data has been addressed in the published literature, the central question that remains unanswered is whether these models are able to function, *with confidence*, in a predictive capacity. The development of credible numerical models *must* consider not only fidelity to data and robustness to uncertainty, but also self-consistency of predictions, which has only recently been recognized [21]. Similar to robustness to uncertainty when replicating experimental data, self-consistency is important because model predictions at untested settings should remain consistent even when uncertainty is accounted for. Thus, confidence in a numerical model is increased when the model and the assumptions upon which it relies are able to fulfill these three attributes. This manuscript discusses the development of a 1-D beam model of the nine-meter CX-100 wind turbine blade developed at Sandia National Laboratories, taking into account fidelity to data, robustness to uncertainty, and self-consistency of model predictions during model development. The beam model is compatible with NLBeam, FE nonlinear beam code that has been developed for integration with the CFD code WindBlade, to model wind turbines at the plant scale.

This manuscript first provides an overview of Info-Gap Decision Theory in Section 2. Figure 5.3 illustrates the steps followed in the analysis of the blade model. Section 3 provides a description of the experimental data utilized in this study, and steps taken to derive equivalent 1-D parameters from a 3-dimensional (3-D) FE model. In Section 4, the 1-D model is then calibrated to experimental data via genetic algorithm optimization using experimental modal data considering both the fidelity to data and robustness to uncertainty. Section 5 extends the discussion to NLBeam, where the self-consistency of deflection predictions to an untested loading scenario is considered.

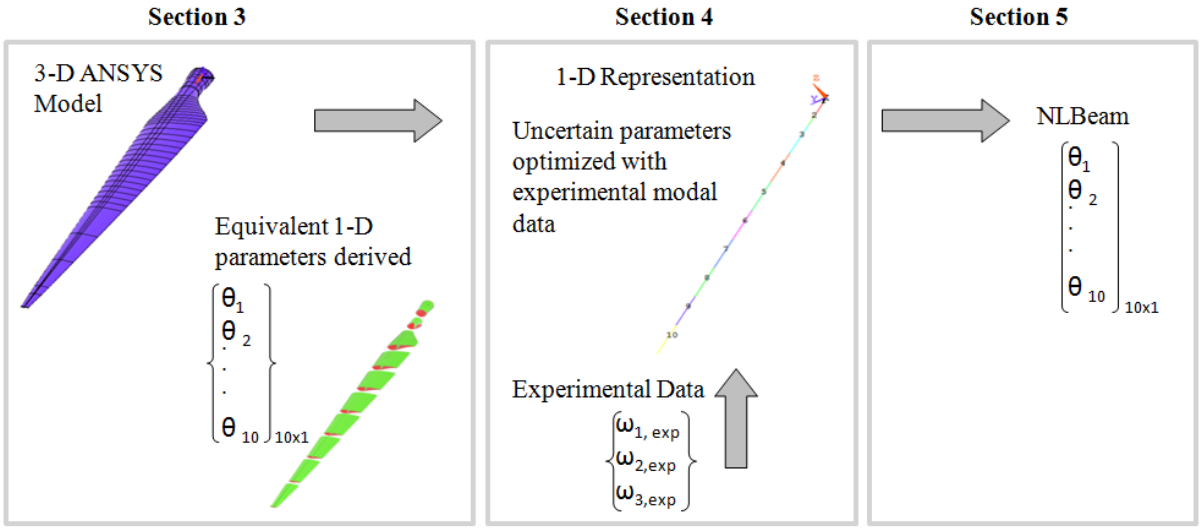

Figure 5.3: Flowchart for Identification of Model Parameters.

5.2 Overview of Info-Gap Decision Theory

Info-Gap Decision Theory (IGDT) provides a useful non-probabilistic method to quantify the effect of uncertainty on any system with an input/output relationship. The formulation of IGDT acknowledges that uncertainty can have both an undesirable and desirable effect on a system's performance. In IGDT, an info-gap uncertainty model is formulated to quantify the allowable range of uncertainty for inputs to the system, and immunity functions are used to

quantify the degradation or improvement of the performance due to uncertainty. These immunity functions are the robustness and opportuneness functions, and provide the basic tools for decision making in IGDT.

Let's assume a numerical model, M, represents the relationship between the input parameters, u, and output, y.

$$y = M(u) \tag{1}$$

Herein, the uncertainty of concern is the non-uniqueness of the numerical model that originates during the model calibration process, when different combinations of parameters provide the same output.

The quality, or performance, of the model can be defined with a user-defined norm of the test-analysis correlation of simulation predictions, y, to experiments, y_{exp} (recall configuration B in Figure 5.1). The performance is acceptable when a critical performance level, R_C, is fulfilled.

$$R(u) = \|y - y_{exp}\| \leq R_C \tag{2}$$

Similarly, when experimental data is unavailable (as it was the case for predicting configuration A in Figure 5.1), the performance of the model can be defined by the self-consistency of predictions. In this case, the performance of the model can be defined with a user-defined norm of the simulation predictions, y, to the predictions obtained at the nominal configuration of the model, y_{nom}, defined using initial, best guesses for the input parameters.

$$R(u) = \|y - y_{nom}\| \leq R_C \tag{3}$$

An info-gap uncertainty model, U, describes how the performance of the system varies around the nominal model with respect to the horizon of uncertainty, α. When $\alpha = 0$, the uncertain input parameters remain at their nominal setting, u. As the horizon of uncertainty increases, the range in which the uncertain input parameters are allowed to vary increases, represented with $\tilde{u}$. Within this range we explore all possible combinations of uncertain input parameters that fulfill a critical

performance, R_C. The info-gap uncertainty model is used to define the uncertainty space, or allowable range of variation for $\tilde{u}$, given a specified horizon of uncertainty. In *uniform-bound* info-gap uncertainty model, the uncertainty space is defined using an absolute difference between the parameters of the nominal model and the uncertain model:

$$U(\alpha;\tilde{u}) = \{u : |u - \tilde{u}| \le \alpha\}, \alpha \ge 0 \tag{4}$$

Here, the horizon of uncertainty assumes the same units as the uncertain input parameters. Other examples of info-gap models, available in [22], utilize percentage differences between the nominal model and uncertain model such that the horizon of uncertainty is unitless. The key point of the info-gap model is that the uncertain system outputs are described for increasing levels of horizon of uncertainty, which requires less information than what would be needed to formulate a probability distribution.

The robustness function quantifies the degradation of performance, while the opportuneness function quantifies the improvement of performance at different levels of horizon of uncertainty, α. The formulation of both equations are similar, however, robustness attempts to find the maximum horizon of uncertainty and opportuneness finds the minimum horizon of uncertainty, at which the critical performance, R_C is achieved.

$$\begin{aligned} \text{robustness, } \hat{\alpha} &= \max\{\alpha\text{: minimum requirement always satisfied}\} \\ \text{opportuneness, } \hat{\beta} &= \min\{\alpha\text{: sweeping success is possible}\} \end{aligned} \tag{5}$$

Conceptually, the robustness, $\hat{\alpha}$ is the greatest value of the horizon of uncertainty, α, for which the performance requirement is satisfied, and the opportuneness, $\hat{\beta}$ is the smallest deviation from the nominal value that will provide windfall success. Here, a ‘large’ or ‘small’ value of uncertainty is relative; however the general aspiration is for the robustness to be bigger

and the opportuneness to be smaller. In practical terms, the robustness describes the worst-case scenario for uncertainty, and the opportuneness describes the best-case scenario. Practically, the best case performance remains disregarded, while the worst case scenario is used for design constraints. For this reason, the remainder of the discussion is confined to robustness.

Equation 6 presents the equation for robustness using mathematical terms. Note that when evaluating the maximum performance, the parameter values, *u*, are confined to those that satisfy the info-gap uncertainty model, *U(u;α)*, at each given level of horizon of uncertainty.

$$\hat{\alpha} = max\left\{\alpha : \max_{u \in U(u;\alpha)} R(u) \le R_C\right\}, \alpha \ge 0 \qquad (6)$$

In Equation 6, critical performance level, R_C, is not determined beforehand such that the model performance can be evaluated for a range of critical performance levels to aid in the decision making process.

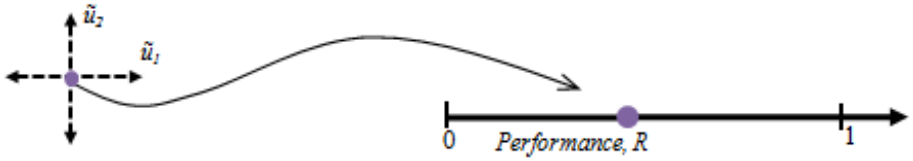

5.4-a. Performance at α=0.

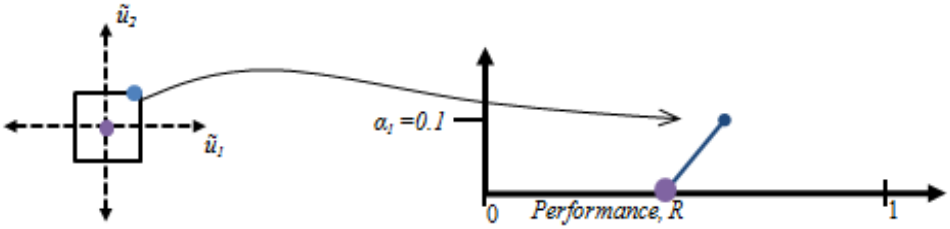

5.4-b. Development of Robustness Curve.

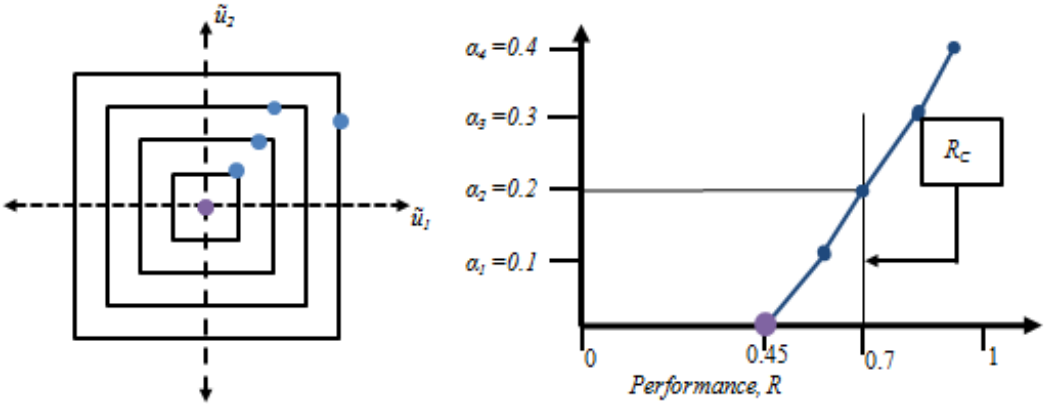

5.4-c. Info-gap Robustness.

Figure 5.4: Illustration of a Hypothetical Info-Gap Robustness.

Figure 5.4 demonstrates the evaluation of robustness for a hypothetical model with two uncertain parameters, u_1 and u_2. Let's assume that R = 0 represents the desired performance of the system. Figure 5.4-a shows the evaluation of parameters at their nominal setting, i.e., when $\alpha = 0$. As the horizon of uncertainty, α, increases, the permissible ranges of u_1 and u_2 increase, resulting in the possibility that the performance will deviate from the nominal condition. Figure 5.4-b demonstrates the development of the resulting robustness curve, and how the performance degrades with larger horizon of uncertainty, α. From a practical standpoint, quantifying info gap robustness, $\hat{\alpha}$ requires an analysis wherein the uncertainty space is searched to determine the maximum degradation in performance, R.

Figure 5.4-c is the resulting info-gap robustness curve for four levels of uncertainty. As α increases, the performance degrades. Here, assume that the horizon of uncertainty is evaluated in increments of 10% uncertainty in parameters (i.e. $\alpha_1 = 0.1$, $\alpha_2 = 0.2$, $\alpha_3 = 0.3$, and $\alpha_4 = 0.4$). To obtain a performance of 0.45 from the system in Figure 5.4, parameters u_1 and u_2 must be known with zero uncertainty, as indicated by the x-axis in Figure 5.4-c. However, suppose the critical performance requirement, R_C, is 0.7, as indicated by the vertical line in Figure 4-c. To guarantee the performance of the system is 0.7 or less, 20% uncertainty in the input parameters can be

tolerated. Only by relaxing the performance requirement will the range of permissible variation in the parameters increase, which demonstrates the trade-off of fidelity and robustness.

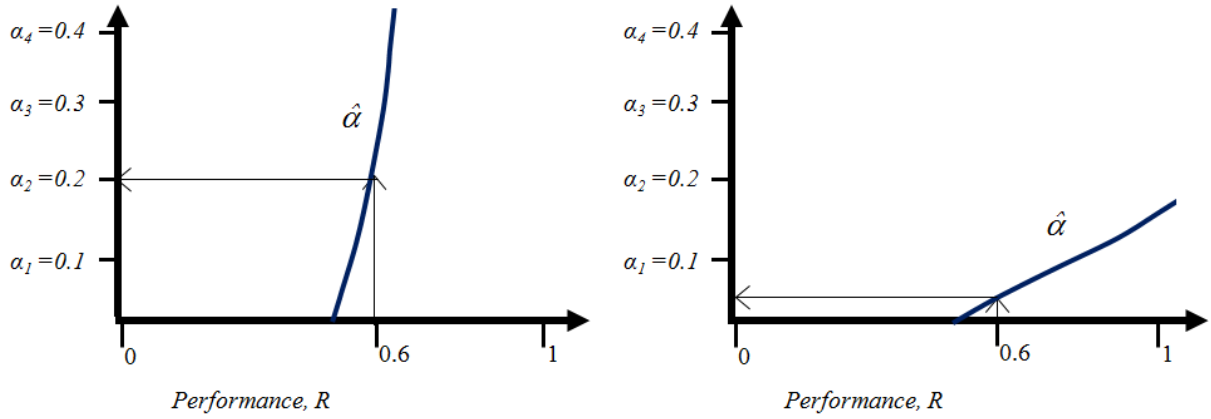

5.5-a. Large Robustness **5.5-b. Small Robustness**

Figure 5.5: Conceptual Representation of Robustness

A comparison of small and large robustness is provided in Figure 5.5. The system analyzed in Figure 5.5 assumes a desired performance of R = 0. Obtaining a robustness curve with large slope, "$\Delta\alpha/\Delta R$," as indicated in Figure 5.5-a indicates that the model predictions are insensitive to increasing levels of uncertainty, α. When the performance of the model can be no worse than R = 0.6, the amount that the parameters are allowed to vary corresponds to a horizon of uncertainty of $\alpha = 0.2$. On the contrary, Figure 5.5-b demonstrates small robustness, which indicates that the predictions of the model are sensitive to the values of *u*. Here, when the performance is R = 0.6, the allowable uncertainty is only $\alpha = 0.05$. Clearly, a nearly steep or vertical slope as shown in Figure 5.5-a is desirable as it demonstrates that the parameter values, *u*, are robust to uncertainty and thus, to our assumptions applied in the model calibration process.

5.3 Development of Simplified 1-D Model

Fixed-free experimental modal analysis of the CX-100 wind turbine blade is conducted at the National Renewable Energy Laboratory [23]. Figure 5.6 shows the set-up and base-fixity of

the experimental configuration, where the blade is mounted to a 7-ton steel frame. Modal testing is performed using a roving impact hammer test with four uni-axial accelerometers and one tri-axial accelerometer. Response measurements are obtained for 65 impact locations: 47 in the flapwise directions, and 18 in the edgewise directions. Three test repeats are performed with a linear average and 150 Hz sampling frequency. The acceleration response is collected with 4096 sampling points in 11 seconds. A window function is not used as the blade response is abated within measurement time window. The natural frequencies obtained from the experiments are provided in Table 5.1.

Table 5.1: Results of the Experimental Modal Analysis.

Mode	Frequency (Hz)	Description
1	4.35	1st Flap Bending
3	11.51	2nd Flap Bending
4	20.54	3rd Flap Bending

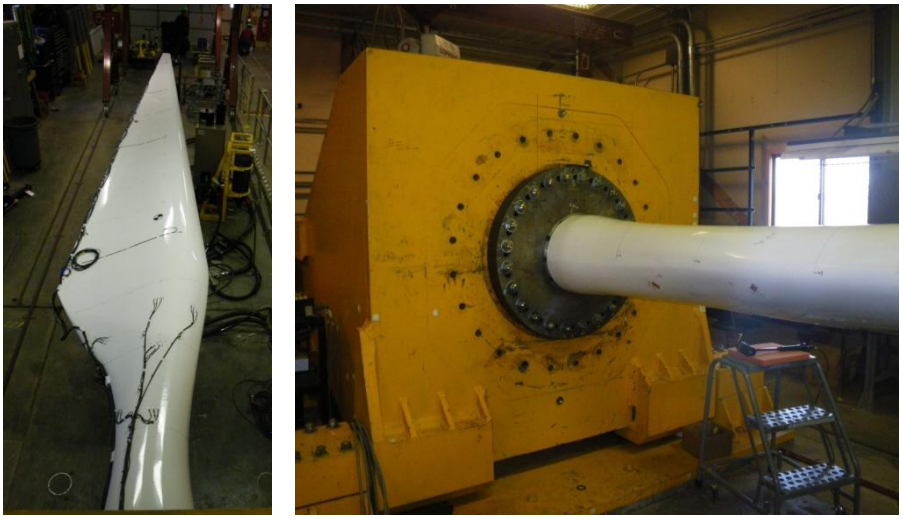

Figure 5.6: Experimental set-up (left) and base fixity (right).

The 3-D FE model developed in [23] is used to derive initial model parameters of the 1-D beam model. In [26], the 3-D FE model is built using NuMAD, pre-processing software developed at Sandia National Laboratory and imported to ANSYS v. 12, FE analysis software with Shell281 elements. The 3-D FE model is developed using the accurate geometry of the CX-100 wind turbine blade obtained from design specifications. The geometric model is divided into six sections defined by linear, isotropic material properties with the cross section homogenized through the use of the rule of mixtures. Sensitivity analysis of a two-level, full factorial design of experiments is performed to identify the parameters that influence 95% of the variability in the model. Measurements of the natural frequencies obtained from modal testing at Los Alamos National Laboratory are utilized to calibrate the FE model in two configurations: free-free, where the blade is suspended by straps, and fixed-free, where the blade is attached to a steel bookend fixture. Instead of performing calibration as an optimization of model parameters to best-fit the experimental data, inference uncertainty quantification is performed to explore the posterior probability distribution of the uncertain parameters. The mode shape vectors used for validation are kept separate from, and independent of, the natural frequencies that were used for sensitivity analysis and calibration exercises. The ability of the 3-D model to predict mode shape deflections is validated through modal assurance criterion. An excellent agreement is observed with 84% correlation for the free–free modes and 94% correlation for the fixed–free modes, suggesting that the mass and stiffness of the blade is properly represented. This earlier validation study allows the 3-D model to be a defensible source to supply initial values of the material properties for the 1-D beam model.

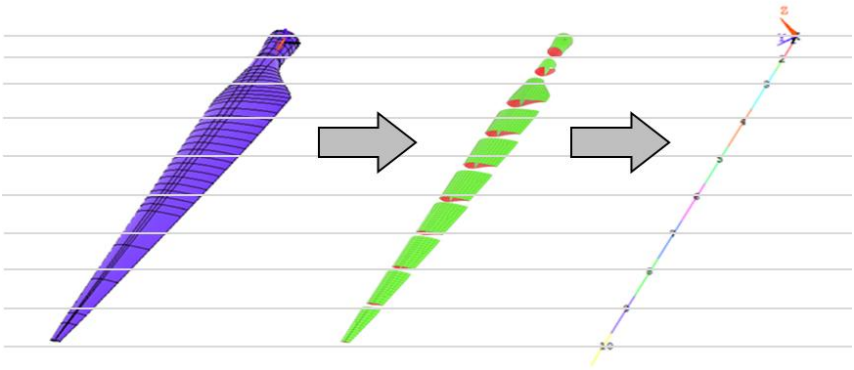

Figure 5.7: Deriving equivalent beam model properties of the CX-100.

As shown in Figure 5.7, the 3-D model of the wind turbine blade is discretized into equivalent 1-meter elements with an additional node placed at the 0.675 meter station to capture the effects of the tapering root section. These 1-D sections are modeled using Beam189 elements in ANSYS. These sections are analyzed individually to provide approximations of the model parameters. The mass contribution of each section is identified, providing an estimate for the equivalent density of the 1-D model. The cross sectional area, effective Young's modulus, and area moments of inertia are approximated for each section by averaging the values measured at the beginning and end of each section. The cross sectional area is calculated by multiplying the total cross-sectional element lengths by the material thickness of each element. The Young's modulus is calculated using an area proportional weighting. Lastly, the area moments of inertia are derived by individually calculating and summing the area moment of inertias for all elements in the cross section. Table 5.2 lists the initial estimates that are determined for the equivalent beam properties.

Table 5.2: Initial Estimates of the Equivalent Beam Properties.

Section	Area (m^2)	Mass (kg)	Density (kg/m^3)	I_{xx} (m^4)	I_{yy} (m^4)	I_{xy} (m^4)	E (GPa)
1	0.0321	55.99	2584.1	0.00052	0.00051	3.22E-06	36.01
2	0.0133	8.35	1929.3	0.00020	0.00015	3.40E-05	24.33
3	0.0177	19.45	1097.2	0.00111	0.00023	0.00030	22.19
4	0.0199	18.88	949.0	0.00161	0.00022	0.00040	13.34
5	0.0169	16.37	967.5	0.00104	0.00010	0.00019	6.29
6	0.0129	12.69	981.0	0.00061	4.58E-05	8.11E-05	8.19
7	0.0093	7.36	794.8	0.00031	1.66E-05	3.00E-05	10.04
8	0.0073	5.38	736.5	0.00014	6.01E-06	8.89E-06	10.51
9	0.0051	3.75	739.2	5.05E-05	1.76E-06	1.52E-06	10.07
10	0.0028	2.08	754.1	1.31E-05	3.73E-07	4.00E-07	8.61

Table 5.3 provides a comparison of the first three flapwise frequencies from experimental results and the 1-D FE model defined with the properties listed in Table 5.2. The comparison demonstrates that the simulation is able to replicate the experimental data within 10.3% error. This level of agreement demonstrates the usefulness of the 3-D model in providing initial estimates of material properties. However, further calibration is necessary to improve the ability of the model to better reproduce the experimental data.

Table 5.3: Comparison of Frequencies.

Mode	Experimental Frequency (Hz)	Simulated Frequency (Hz)	% Difference
1st Flap Bending	4.35	3.90	10.3
2nd Flap Bending	11.51	9.78	5.4
3rd Flap Bending	20.54	12.13	1.3

5.4 Calibration with Genetic Algorithm

In this study, genetic algorithm is utilized to optimize correction factors that are applied to the moment of inertia parameters of the 1-D beam model. Genetic algorithm is a stochastic

optimization, rooted in providing randomness by mimicking biological behaviors to implement the survival of the fittest principle [25]. To perform a genetic algorithm optimization, lower and upper bounds of each parameter are specified, creating a range of values for each parameter that is being optimized. The algorithm then creates an initial population with a user-defined number of random parameter sets. An objective function is utilized to score and rank each parameter set. A new population is then formulated using three main criteria: (i) elite individuals, (ii) mutations, and (iii) crossovers. The elite individuals of the population are simply those with the highest rank. The remaining individuals are used as parents to develop mutations and crossovers. Mutations occur when parameters are randomly changed, and crossovers are developed by randomly combining parameter sets. The algorithm then iterates over a number of populations until a stopping criteria is met. The stopping criteria can be defined as a maximum number of generations, a minimum fitness level to be met, the length of time that the genetic algorithm can operate, or a minimum weighted average change in the fitness function.

In our study, a maximum of 100 generations are created, with a total of 20 individuals per generation. To keep the optimization to a manageable size, the moment of inertia parameters (I_{xx}, I_{yy}, I_{xy}) for each section are grouped, requiring only ten correction factors. The FE model is replaced with an emulator to further reduce computation demands for efficient evaluation of the natural frequencies. A cubic polynomial emulator is trained using a hybrid of full factorial and central composite design of experiments of the ten uncertain correction factors. The goodness of fit of the polynomial emulator adapted for this study is demonstrated in Figure 5.8.

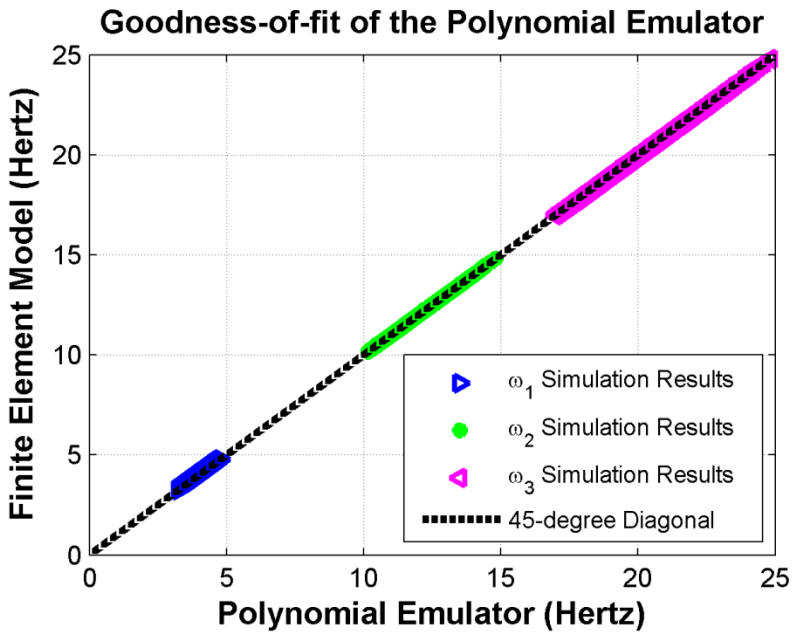

Figure 5.8: Goodness of fit of the Polynomial Emulator.

Calibration of the correction factors is performed by considering the fidelity of the FE model to experimental data. The model performance, R, is computed using a root mean square difference of the first three flapwise frequencies to experimental data, which assumes units of Hertz (Hz) as shown in Equation 7:

$$R = \sqrt{\sum_{i=1}^{3} \left(\omega_{sim,i} - \omega_{\exp,i} \right)^2} \ . \tag{7}$$

Defining the objective function of the genetic algorithm using the relationship provided in Equation 7 creates a *fidelity optimal* model. A fidelity optimal model would be able to re-create experimental data without accounting for uncertainties present due to our assumptions and lack of knowledge in the model development process. An info-gap analysis, as discussed in Section 2, is used to investigate the trade-off between the fidelity to data and the robustness to uncertainty of model output. Here, the performance is quantified using the relationship provided in Equation 7.

The info-gap uncertainty model is represented using a uniform-bound uncertainty model as given in Equation 8. Note that the horizon of uncertainty is dimensionless because it is applied to dimensionless correction factors.

$$U(\alpha;\tilde{u}) = \{u : |u - \tilde{u}| \le \alpha\}, \alpha \ge 0 \tag{8}$$

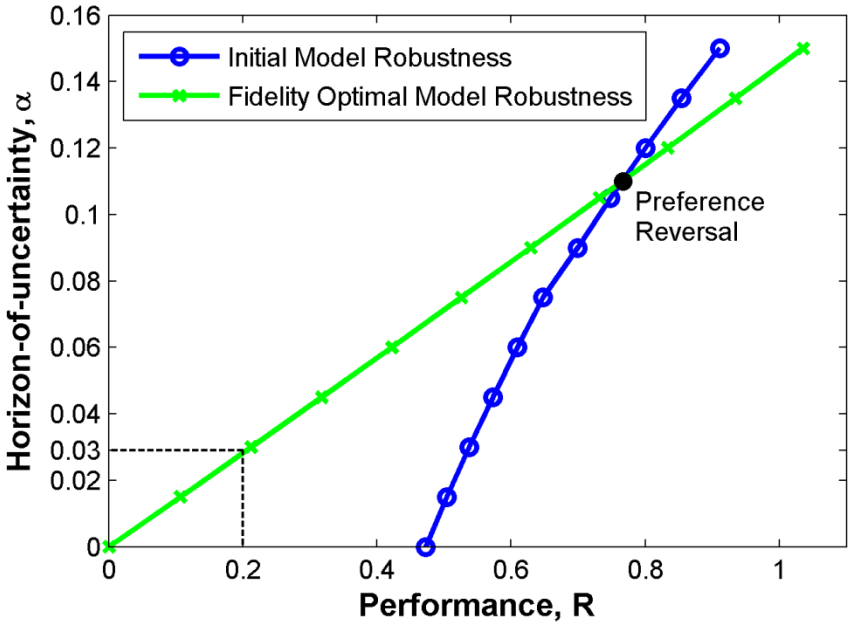

Figure 5.9: Info-Gap Robustness of Fidelity-Optimal Model compared to Nominal Model.

Figure 5.9 compares the robustness of the model developed with the initial parameter estimates in Table 5.2 and the fidelity-optimal model developed with the parameters optimized by genetic algorithm. Figure 5.9 is convenient for comparing both the fidelity to data and robustness to uncertainty of the FE model before and after calibration of the correction factors. Several observations can be garnered from Figure 5.9. First, the fidelity optimal model is capable of achieving a performance of R = 0, however, the model possess zero robustness in order to achieve this performance. As the performance requirement is relaxed, more uncertainty in the model parameters is allowed. For example, if the performance requirement of the model is 0.2

Hz, then the allowable horizon of uncertainty increases to 0.03 for the fidelity optimal model, as indicated by the dashed lines in the figure. In addition, an intersection of robustness curves is demonstrated in Figure 5.9. This represents an important phenomenon in IGDT, known as *preference reversal*. When the performance requirement is less than 0.77 Hz, the fidelity optimal model is preferred, when greater than 0.77 Hz, the initial model prior to optimization is preferred.

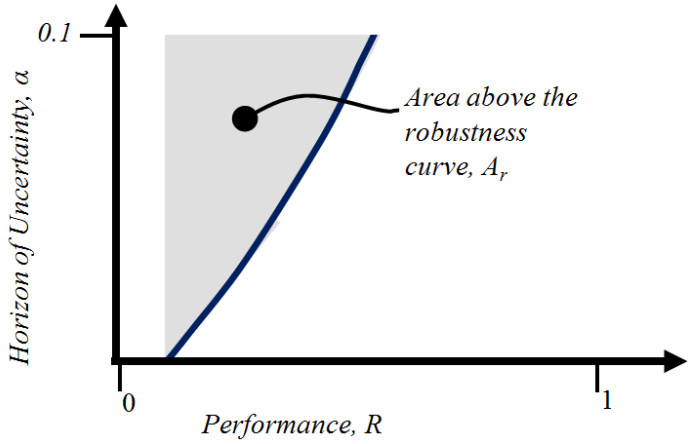

Figure 5.10: Quantification of Robustness for the Objective Function.

Another important observation in Figure 5.9 is that when calibration is performed to optimize fidelity, the slope of the robustness curve, "Δα/ΔR," decreases from the slope of the robustness curve for the initial model. This indicates that the fidelity optimal model is more sensitive to uncertainty than the initial model. However, as previously discussed [14, 15, 16, 21], robustness is desired so that assumptions applied during the model parameter identification process is of low significance on model predictions. To obtain a *robust and fidelity optimal* model, the objective function provided in Equation 6 is modified to include the robustness to uncertainty of model predictions during model calibration. Previous studies have proposed metrics to quantify robustness during calibration, such as max/min performance [16], evaluating noisy objective functions [15], and non-gradient based parameter sensitivity [14]. The robustness metric utilized in this study is formulated in the context of IGDT as demonstrated in Figure 5.10,

using the area above the robustness curve, A_r. The area, A_r, assumes units of Hz because the area is taken as a multiplication of the performance, R, which assumes units of Hz, and the horizon of uncertainty, α, which is unitless. This process assumes that the maximum allowable variation in the correction factors is known. For this application, due to the confidence by which the parameters were derived, an upper bound of 10% variability from the nominal values of the parameters is considered. This quantification of robustness captures the behavior of the robustness curve, where a smaller area describes a system with larger robustness, and a larger area describes a system with smaller robustness.

Weighting functions, w_1 and w_2 are used to sum the competing metrics of the objective function:

$$objective = w_1 \times R + w_2 \times A_r \tag{9}$$

where the sum of w_1 and w_2 is one, R is the performance of the model and A_r is the area above the robustness curve. To execute the genetic algorithm with this objective function, a robustness curve is generated for each candidate solution explored by the genetic algorithm, and then the area above the robustness curve is calculated. Practically, this requires a nested optimization: the outer genetic algorithm optimization searches for candidate solution based on the objective function, while the inner optimization performs the info-gap analysis and calculates the area above the robustness curve for each candidate solution.

Weighting factors, as given in Equation (9) can be generally ambiguous because of the sensitivity of solutions to changes in the weighting factors [26]. For this reason, five combinations of weighting factors are considered, varying from the full weight assigned to w_1 to zero weight assigned to w_1. When $w_1 = 1$ and $w_2 = 0$, 100% of the weighting is applied to the fidelity, thus producing a *fidelity optimal* model. When $w_1 = 0$ and $w_2 = 1$, 100% of the weighting is applied to the robustness, thus producing a *robust optimal* model.

Figure 5.11 provides a visual comparison of the models produced from the five combinations of weighting functions. This visual comparison of models provides a clear demonstration that the model produced with the fidelity weighting, $w_1 = 0.75$ and the robustness weighting, $w_2 = 0.25$ provides the best trade-off of robustness to uncertainty and fidelity to data. When $w_1 = 0.75$, $w_2 = 0.25$, the fidelity to data decreases from 0.0005 Hz in the fidelity optimal model ($w_1 = 1$, $w_2 = 0$) to 0.007 Hz (1300% increase in performance error), which is an error that is comparable to numerical error. However, the area above the robustness curve is cut in half, from 0.0346 Hz to 0.0163 Hz (53% reduction in area), demonstrating that weighting only 25% of the objective function to robustness is sufficient to produce a model with improved robustness while maintaining fidelity to data.

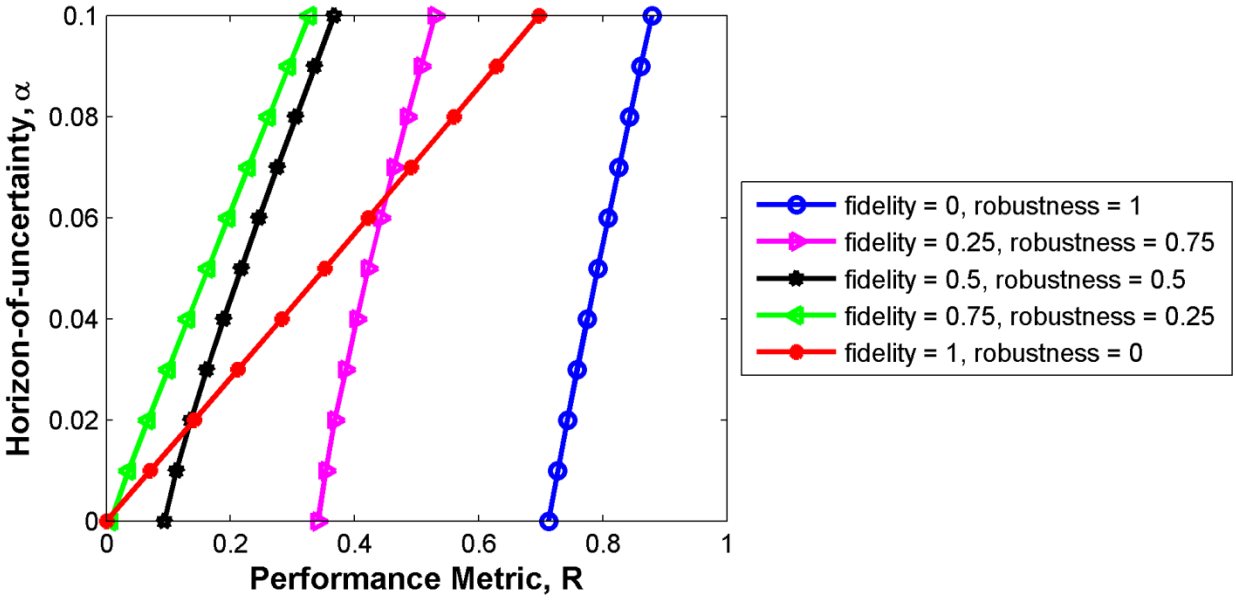

Figure 5.11: Info-Gap Analysis Comparing the Weighting Functions.

Figure 5.12 demonstrates the trade-offs associated with providing more weight for robustness, i.e. w_2. Clearly, when $w_2 = 0$, the smallest fidelity and largest robustness is achieved. The steep slope of the robustness line in the shaded area of the graph demonstrates that as w_2 is

reduced from 1 to 0.75, the area above the robustness curve decreases, achieving large gains in the robustness performance of the model. Further, the flat slope of the fidelity line demonstrates that a minimal amount of fidelity is compromised to achieve this reduction in the area above the robustness curve. The area above the robustness curve continues to decrease as w_2 decreases, demonstrated by the decreasing values for the robustness line from 0.75 to 0, however with diminishing returns.

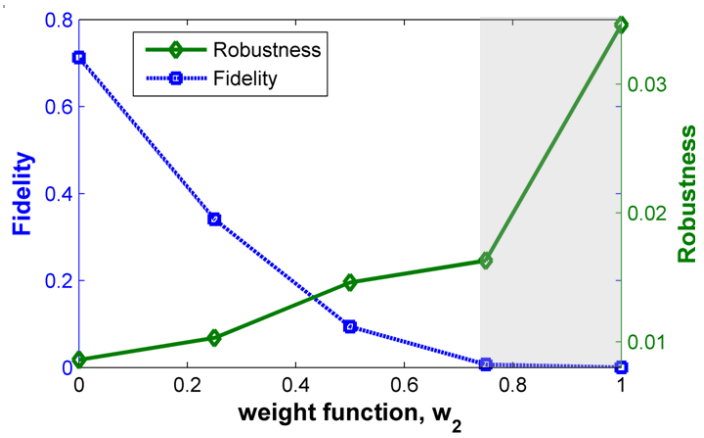

Figure 5.12: Visual Comparison of Weighting Functions.

5.5 NLBeam and Self-Consistency of Predictions

The ultimate goal herein is to integrate the 1-D FE model developed in this study into *NLBeam*, a FE based code developed at Los Alamos National Laboratory [10]. NLBeam is developed to couple realistic wind turbine elastodynamics into *WindBlade* to simulate the performance of wind plants without adding significant computational costs to the numerical simulation. The NLBeam code models wind turbine blade dynamics using the geometrically exact beam theory and is an improvement over many alternative methods because of its ability to handle geometric nonlinearities [10]. Therefore, NLBeam is particularly well-suited in modeling wind turbine blades, which routinely experience large deformations and strains. The question handled in this section, is whether the 1-D model developed in Section 4 through calibration to

natural frequencies of the wind turbine blade is also capable of producing predictions of static deflection that are self-consistent.

In the formulation of NLBeam, sectional strains and curvatures are computed along the position of a beam accounting for local coordinate rotations. Sectional strains are calculated from the derivative of the beam's position in space with respect to the undeformed distance along the beam and rotating it to local coordinates. This gives the axial force and transverse shear strains, as seen in Equation 10, where Λ^T is the rotational matrix, r_n' is the position derivative, and b_1 is the direction of the cross-sectional normal:

$$\gamma_n = \Lambda^T r_n^{'} - b_1. \tag{10}$$

Sectional curvatures are calculated from the derivative of the rotation tensor with respect to the position along the undeformed beam, giving the torsional rate of twist and bending curvature. The sectional curvatures in local coordinates are shown in Equation 11 where Λ^T is the rotational matrix and Λ_n' is the rotation tensor:

$$\kappa_n = \Lambda^T \Lambda_n^{'}. \tag{11}$$

Using the strain energy equation as a basis and differentiating with respect to section strains and curvature, sectional forces and moments can be calculated. The local strain energy is related to the cross-sectional properties of the beam at a given point as well as the section strains and curvature. In Equation 12, the matrix [C] represents a matrix of cross-sectional properties expanded in Equation 13. For isotropic, homogeneous materials, this matrix assumes a diagonal shape:

$$U = \frac{1}{2}\begin{Bmatrix}\gamma\\ \kappa\end{Bmatrix}^T [C] \begin{Bmatrix}\gamma\\ \kappa\end{Bmatrix}, \tag{12}$$

and:

$$\begin{Bmatrix} F_{Na} \\ F_{Nv2} \\ F_{Nv3} \\ F_{Mt} \\ F_{Mb2} \\ F_{Mb3} \end{Bmatrix} = \begin{bmatrix} EA_1 & & & & & \\ & GA_2 & & & 0 & \\ & & GA_3 & & & \\ & & & GJ & & \\ & 0 & & & EI_2 & \\ & & & & & EI_3 \end{bmatrix} \begin{Bmatrix} \gamma_1 \\ \gamma_2 \\ \gamma_3 \\ \kappa_1 \\ \kappa_2 \\ \kappa_3 \end{Bmatrix}. \tag{13}$$

The result of this formalism is a linear force to strain relationship in the moving beam coordinate frame. However, the relationship between generalized strains and generalized coordinates involves the rotation tensor, which is inherently nonlinear.

For the remainder of this study, the five sets of parameters developed using varying combinations of weighting functions in Section 4 are transferred to NLBeam to assess the self-consistency of predictions of static deflection under both linear and non-linear loadings. The static deflection of the beam is considered with a load of 20 N for the linear case and 8000 N for the non-linear case applied to the free end.

An info-gap analysis is re-considered to evaluate the consistency of predictions at increasing levels of uncertainty for each parameter set developed from different combinations of weighting functions. As discussed in Section 2, with Equation 3, the self-consistency analysis is performed by comparing the predictions of the model with increasing levels of uncertainty to the predictions of the model with nominal parameters. To evaluate self-consistency, the tip deflection is normalized with respect to the nominal setting:

$$R(u) = \left\| \frac{\delta - \delta_{nom}}{\delta_{nom}} \right\| \leq R_C \tag{14}$$

This representation of self-consistency considers the percentage change in the predictions. Similar to the analysis provided in Section 4, the info-gap uncertainty model is represented using a uniform-bound uncertainty model, provided in Equation 15.

$$U(\alpha;\tilde{u}) = \{u : |u - \tilde{u}| \le \alpha\}, \alpha \ge 0 \quad (15)$$

The resulting info-gap analysis for self-consistency is shown in Figure 5.13. The model produced with $w_1 = 0.5$ and $w_2 = 0.5$ is able to provide the most consistent predictions of tip deflection. This observation differs from the trends observed in the robustness to uncertainty analysis of Section 4, where the model produced with $w_1 = 0$ and $w_2 = 1$ provided the model with highest robustness to uncertainty. However, the fidelity optimal model, which provided the lowest robustness to uncertainty, remains the model with the lowest self-consistency of predictions. This result suggests that model parameters selected considering only the fidelity to data are also most susceptible to assumptions upon which the model relies.

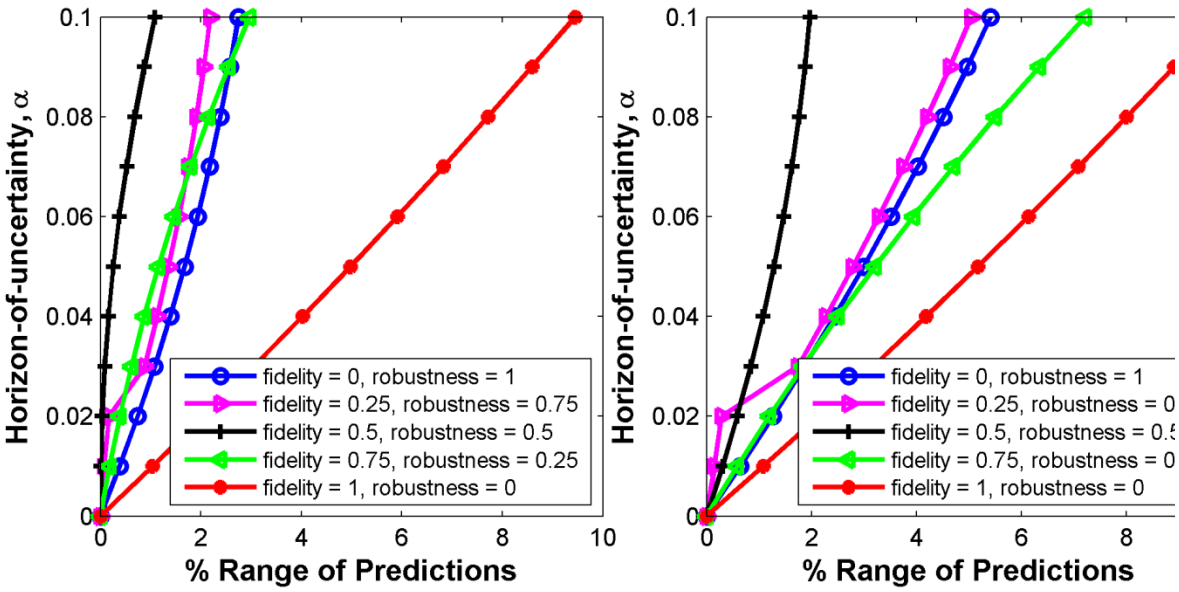

5.13-a. Linear **5.13-b. Nonlinear**

Figure 5.13: Self-consistency of Predictions in NLBeam

Table 5.4: Comparison of Weighting Function Combinations.

Weighting Functions		Fidelity and Robustness Metrics		Self-Consistency	
Fidelity, w_1	Robustness, w_2	Fidelity, R (Hz)	Robustness, A_r (Hz)	Linear	Non-Linear
0	1	0.713	**0.009**	0.520	0.266
0.25	0.75	0.341	0.010	0.485	0.212
0.5	0.5	0.094	0.015	**0.192**	**0.098**
0.75	0.25	0.007	0.016	0.678	0.276
1	0	**0.0005**	0.035	0.936	0.902

Table 5.4 provides a comparison between the five models developed with different combinations of weighting functions. The self-consistency results are taken as the area above self-consistency curve, similar to the quantification of robustness. Recall that the fidelity and robustness metrics are formulated such that smaller values result in better performance for each category. It is emphasized that most studies only consider the fidelity to data of model predictions, given with the weighting combination $w_1 = 1$ and $w_2 = 0$. However, as observed in Table 5.4, the combination of weighting functions that produces the best performance for each criterion is not guaranteed to provide the best performance for the other two criteria. This is indicated by the bolded values in Table 5.4, which show that the optimal model for each column is different. The overall results demonstrate that model development should consider a *trade-off* between fidelity to data, robustness to uncertainty, and self-consistency of predictions.

5.6 Conclusions

This paper discusses the development of a simplified 1-D beam model of the CX-100 wind turbine blade. Although providing a simplified representation of reality, 1-D models are useful to couple with computational fluid dynamics (CFD) models for the simulation of wind turbines at the plant scale. Successful integration of such models offers the potential to effectively study the in-service performance of wind turbines, thusly increasing the reliability of wind

turbines and maximizing power output. To pursue the model developed herein, the 1-D model is first calibrated to natural frequencies in ANSYS v. 12.1 using Beam189 elements, and then transferred to NLBeam for evaluation of self-consistency. Calibration is performed by simultaneously considering the fidelity to data and robustness to uncertainty of model predictions. The analysis goes a step further to evaluate self-consistency of predictions from static deflection of an applied load. The emphasis is placed in evaluating the *trade-offs* of fidelity to data, robustness to uncertainty, and self-consistency of predictions, because these attributes are often antagonistic. This concept is demonstrated in calibration of the beam model, where the fidelity to data was improved but at the cost of reducing the robustness to uncertainty of model predictions.

The beam model is developed in the context of Info-Gap Decision Theory (IGDT) to pursue a finite element model that exhibits both fidelity to data and robustness to uncertainty. It is posited by the authors that this method increases the credibility of model predictions, rather than performing calibration by which only the fidelity to data is considered. Through genetic algorithm optimization, it is demonstrated that different model parameter sets can be established when calibrating to the same experimental data. First, a *fidelity optimal* model is pursued, in which the model parameters are calibrated to best replicate the experimental data. Through use of an info-gap analysis, it is demonstrated that while the fidelity of the calibrated model is improved, the robustness of the model when compared to the initial model is significantly reduced.

The genetic algorithm optimization is then modified to incorporate robustness, to provide a *fidelity robust* model. The inclusion of robustness to uncertainty in model calibration allows for the uncertainties introduced by non-uniqueness of model parameters to be of low influence on predictions. The robustness is incorporated by considering the area above the robustness curve for the candidate solutions explored by the genetic algorithm. Weighting functions are utilized for the fidelity and robustness metrics. To explore the effect of weighting functions on the genetic

algorithm optimization, various combinations of weighting functions are evaluated to explore the trade-off to develop models that are both robust and fidelity optimal. It is shown that weighing only 25% of the objective function towards robustness is capable of providing large gains in robustness.

The self-consistency of model predictions is evaluated to further explore the ability of the model to predict with confidence. A hypothetical loading is applied to the five alternative beam models, and the tip deflection of the model is observed. An info-gap analysis is repeated for all five beam models to observe the resulting range of predictions. It is observed that the fidelity optimal model remains the least robust and self-consistent. This suggests that models developed only considering the fidelity to experimental data are the most susceptible to assumptions made in the model development process. It is emphasized, however, that a more powerful exploration of self-consistency relies on loading scenarios that will be applied when coupled with the *WindBlade* CFD code.

References

[1] U.S. Department of Energy, 20% Wind Energy by 2030: Increasing Wind Energy's Contribution to U.S. Electricity Suppy, Report DOE/GO-102008-2567, Washington, D.C, 2008.

[2] T. Ashwill, Materials and innovations for large blade structures: research opportunities in wind energy technology, in: 50th AIAA Structures, Structural Dynamics, & Materials Conference, Palm Springs, CA, U.S., May, 2009.

[3] M.E. Bechly, P.D. Clausen, Structural design of a composite wind turbine blade using finite element analysis, Computers & Structures. 63 (1997) 639-646.

[4] M.M. Shokrieh, R. Rafiee, Simulation of fatigue failure in a full composite wind turbine blade, Composite Structure. 74 (2006) 332-342.

[5] J.C. Marín, A. Barroso, F. París, J. Cañas, Study of fatigue damage in wind turbine blades, Engineering Failure Analysis. 16 (2009) 656-668.

[6] Y. Brazilevs, M.C. Hsu, I. Akkerman, S. Wright, K. Takizawa, B. Henicke, T. Spielman, T.E. Tezduyar, 3D simulation of wind turbine rotors at full scale, Part I: Geometry modeling

and aerodynamics, International Journal for Numerical Methods in Fluids. 65 (2011) 207-235.

[7] M.A. Sprague, P.J. Moriarty, M.J. Churchfield, K. Gruchalla, S. Lee, J.K. Lundquist, J. Michalakes, A. Purkayastha, Computational modeling of wind-plant aerodynamics, in: Scientific Discovery through Advanced Computing Program 2011 Conference, Denver, CO, U.S., July 2011. (also, NREL Report No. CP-2C00-52445).

[8] B. Sanderse, S.P. van der Pijl, B. Koren, Review of computational fluid dynamics for wind turbine wake aerodynamics, Wind Energy. 14 (2011) 799-819.

[9] L.J. Vermeer, J.N. Sorensen, A. Crespo, Wind turbine wake aerodynamics, Progress in Aerospace Sciences. 39 (2003) 467-510.

[10] S. Dalton, L. Monahan, I. Stevenson, D.J. Luscher, G. Park, K. Farinholt, Towards the Experimental assessment of NLBeam for modeling large deformation structural dynamics, in: R. Mayes, D. Rixen, D.T. Griffith, D. DeKlerk, S. Chauhan, S.N. Voormeeren, M.S. Allen (Eds.), Topics in Experimetnal Dynamics Substructuring and Wind Turbine Dynamics, Volume 2, Springer New York, New York, 2012, pp. 177-192.

[11] R. Linn, E. Koo, WindBlade: Coupled Turbine/Atmosphere Modeling, in: Modeling Turbine-Turbine interactions with Experimental Validation, Los Alamos Annual Workshop, 2011.

[12] T.D. Griffith, T.G. Carne, J.A. Paquette, Modal testing for validation of blade models, Wind Engineering. 32 (2008) 91-102.

[13] F.M. Hemez, C.J. Stull, On the legitimacy of model calibration in structural dynamics, in: T. Simmermacher, S. Cogan, L.G. Horta, R. Barthorpe (Eds), Topics in Model Validation and Uncertainty Quantification, Volume 4, Springer New York, New York, 2012, pp. 95-108.

[14] M. Li, S. Azarm, V. Aute, A Multi-objective genetic algorithm for robust design optimization, in: Proceedings of the 2005 Conference on Genetic and Evolutionary Computation, Washington, D.C., U.S., June 2005.

[15] S. Tsutsui, A. Ghosh, Genetic algorithms with a robust solution searching scheme, IEEE Transactions on Evolutionary Computation. 1 (1997) 201-208.

[16] Y.S. Ong, P.B. Nair, K.Y. Lum, Min-Max surrogate assisted evolutionary algorithm for robust aerodynamics design, IEEE Transactions on Evolutionary Compuation. 10 (2006) 392-404.

[17] Z. Kang, Y. Luo, Reliability-based structural optimization with probability and convex set hybrid models, Structural Multidisciplinary Optimization. 42 (2010) 89-102.

[18] F.M. Hemez, Y. Ben-Haim, Info-gap robustness for the correlation of tests and simulations of a non-linear transient, Mechanical Systems and Signal Processing, 18 (2004) 1443-1467.

[19] I. Takewaki, Y. Ben-Haim, Info-gap robust design with load and model uncertainties, Journal of Sound and Vibration. 288 (2005) 551-570.

[20] P. Vinot, S. Cogan, Y. Ben-Haim, Reliability of structural dynamic models based on info-gap models, in: 20th International Modal Analysis Conference, Los Angeles, CA, U.S., Feb. 2012.

[21] Y. Ben-Haim, F.M. Hemez, Robustness, fidelity and prediction-looseness of models, Proceedings of the Royal Society, A. 468 (2012) 227-244.

[22] Y. Ben-Haim, Info-Gap Decision Theory: Decisions Under Sever Uncertainty, second ed., Oxford, 2006.

[23] K.M. Farinholt, S.G. Taylor, G. Park, C.M. Ammerman, Full-scale fatigue tests of CX-100 wind turbine blades. Part I – testing, in: Proceedings of SPIE, 2012.

[24] K.L. Van Buren, M.G. Mollineaux, F.M. Hemez, S. Atamturktur, Simulating the dynamics of wind turbine blades, part II, model validation and uncertainty quantification, Wind Energy. doi: 10.1002/we1522

[25] M. Mitchell, An Introduction to Genetic Algorithms, third ed., Cambridge, MA, 1998.

[26] T.J. Richardson, M.R. Palmer, G. Liepins, M. Hilliard, Some guidelines for genetic algorithms with penalty functions, in: Proceedings of the Third International Conference on Genetic Algorithms, 191-197, 1989.

CHAPTER SIX

CONCLUDING REMARKS

6.1 Summary of Research Program

This dissertation discusses the trade-offs of ***fidelity-to-data*** and ***robustness-to-uncertainty*** in the development of FE models. First, the development of a three dimensional FE model of the CX-100 wind turbine blade utilizing **V&V** activities to account for sources of uncertainty stemming from the numerical discretization, experimental variability, and parametric uncertainty is discussed. The three dimensional model is then utilized in the development of a one dimensional model by minimizing the differences in model predictions through optimization. The one dimensional representation, which produces a highly idealized description, is necessary to reduce computational demands such that the structural dynamic simulations can later be coupled with computational fluid dynamics simulations to account for realistic wind loading due to atmospheric and topographic effects.

Although fidelity to data is an important attribute of numerical models, this dissertation demonstrates that it is also important for model predictions to remain consistent, or robust, as uncertainties in input parameter values are considered. Such robustness is affected by the model complexity, where overly complex models may run the risk of over-fitting to experimental data during calibration exercises at the cost of poor generalization to other, non-tested settings. Robustness to uncertainty is utilized in an info-gap analysis of blades used to simulate the CX-100 in a configuration where large masses are used to load the blade in bending. Here, a systematic and rigorous method for model selection utilizing IGDT is proposed to study the effect of model complexity on model predictions.

A further drawback in modeling and simulation is non-uniqueness issues that arise during calibration exercises, where different sets of model parameters may be capable of providing a

similar trade-off in fidelity to data and robustness to uncertainty. This issue is addressed in the calibration of the one-dimensional beam model used to simulate the CX-100 wind turbine blade, simultaneously considering the fidelity to data, robustness to uncertainties, and self-consistency of predictions. The fidelity optimal model remains both the least robust and least self consistent, thus demonstrating the importance of performing calibration as a trade off of conflicting attributes.

The research presented herein contributes to the current state of the art of modeling and simulation of wind turbine blades by first identifying and quantifying sources that degrade the predictive capabilities in numerical models. Next, this dissertation utilizes Info-Gap Decision Theory to expand on the widespread use of test-analysis correlation techniques by assessing the robustness-to-uncertainty in the development of credible numerical models. Understanding the behavior of model output by studying the trade-offs of fidelity-to-data and robustness-to-uncertainty can help to facilitate the development of credible models for use in future studies of wind turbine blades, thus contributing to the future development of the wind energy industry. Credible models, in both three- and one-dimensional representations of wind turbine blades can result in designs, which better account for the actual loading and load transfer on the structure. Furthermore, the ability to couple these models with CFD models at the plant scale will result in turbines with increased design and operational life that can efficiently capture energy.

6.2 Major Findings of the Presented Research

The previously summarized research campaign has resulted in the following findings and observations:

Findings from the integrated Verification and Validation study (Chapters 2 and 3):

- Closed form solutions for the bending stress, shear stress, and natural frequencies of a hollow cylinder demonstrate that the Shell-281 elements implemented in ANSYS v. 12.1 demonstrate agreement with the expected second order convergence to the solutions.
- Linearity and reciprocity tests obtained from experiments of the wind turbine blade conducted at Los Alamos National Laboratory demonstrate that the linearity assumptions necessary for modal analysis are fulfilled.
- A simplified finite element model of the CX-100 wind turbine obtained by defining six sections with independent sectional and material properties yield credible model output. Similarly, the use of rule of mixtures of composites can be applied to simplify the definition of the composite layers embedded in an epoxy matrix to isotropic material properties while maintaining sufficient accuracy to experiments.
- A mesh refinement study of the FE model must be performed to examine the solution error and assess asymptotic convergence utilizing Richardson's Extrapolation. A novel choice in mesh size should be based on providing numerical uncertainty that is comparable to test-to-test variability.
- It is necessary to eliminate insensitive parameter from model calibration exercises, which can be identified through designs of computer experiments combined with global sensitivity analysis..
- Fictitious springs can be added to the base of the blade to represent the poorly known semi-flexible boundary conditions.
- Calibrating input parameters in a fully probabilistic manner in the context of Bayesian Inference allows considering experimental uncertainty in the inference of the joint posterior distribution of model parameters. Joint posterior distributions can be evaluated to ensure there is not hidden dependency or correlation between calibration parameters.

- As calibration of a numerical model conditions the model predictions to an experimental dataset, an independent dataset must utilized for the validation of the calibrated model to demonstrate the predictive capability of the numerical model.

Findings and observations from the model selection study (Chapter 4):

- The experimental configuration of the CX-100 wind turbine blade, where masses are added to load the blade in bending, is utilized to provide a separate configuration to evaluate the predictive capability of the model. Two alternative approaches are considered to incorporate the added masses into the simulation, established with different assumptions in development of the model form.
- Parametric studies of the stiffening springs implemented in the numerical model utilizing point masses are performed to study the effect of boundary spring stiffness on model predictions.
- IGDT is utilized to provide a full integration of model form uncertainty and parameter uncertainty in the robustness analysis. Through the development of a fully automated calibration algorithm, the need for fast-running emulators is eliminated by avoiding unwanted approximations introduced by statistical emulators.
- The usefulness of IGDT to address the question of model selection is illustrated. Through IGDT, it is found that the model utilizing solid elements provides predictions that are both higher fidelity and more robust than the model utilizing point masses and stiffening springs.

Findings and observations from the model parameter selection study (Chapter 5):

- Material properties for an equivalent one-dimensional beam model can be approximated from a previously calibrated and validated three-dimensional FE model.
- A novel quantification of robustness, in which the area above the robustness curve of the info-gap analysis, is utilized to implement the robustness to uncertainty in the genetic algorithm optimization to calibrate the one-dimensional beam model to fixed-free experimental modal data from tests performed at the National Renewable Energy Laboratory.
- Different combinations of weighting functions used in the objective function are assessed to demonstrate the trade-offs of fidelity to data and robustness to uncertainty in model calibration.
- It is emphasized that while model calibration is performed considering experimental modal data, one dimensional beam models are commonly used to incorporate flexible body dynamics in coupled simulations of wind turbine blades. Thus, self-consistency of model predictions must be assessed using for instance, the tip deflection due to a fictitious load.
- It is found that the fidelity optimal model remains the least robust and the least self consistent, thus emphasizing the importance of considering robustness to uncertainty and self consistency of predictions in the development of numerical models.

6.3 Limitations, Remaining Issues, and Recommendations for Future Work

Limitations/Assumptions:

Some assumptions exist herein that must be mentioned. While the analyses developed are applied to the CX-100 wind turbine blade, which is a research blade only 9-meters in length, it is emphasized that current wind turbine blades manufactured today are developed with spans of 50

meters and longer. Thus, while the assumption of linear behavior is applicable in the studies provided herein, application of numerical studies to larger blades need to consider the possible development of geometric nonlinear behavior, due to the likelihood of larger angle rotations as blades are produced at larger scales. Further, the use of polynomial emulators to replace the finite element model to perform the info-gap analysis of Chapter 5 rests on the assumption that the response surface can be simplified to a third order polynomial. While this assumption is necessary to provide computational efficiency to the numerical analysis pursued, it is emphasized that emulators can provide approximations to the physics-based models. Lastly, while the case-study applications of robustness provided herein confirm the trade-off of fidelity to data and robustness to uncertainty, further studies are necessary to extend a more general description for robustness to uncertainty in other sources of uncertainty in the numerical models, such as the effect of model form.

Suggestions for Future Work:

Future studies can build on the work presented herein, where IGDT is integrated to demonstrate the robustness to uncertainty in numerical models. For example, single objective optimization seeks to find the optimal solution, however, the trade-offs of fidelity to data and robustness to uncertainty have demonstrated that it would be more appropriate to search for the family of plausible models that fulfill the observed trade off. The use of multi-objective optimization in future studies can provide a more complete description of the trade-offs of fidelity to data, robustness to uncertainty and self-consistency by obtaining the family of solutions and further address non-uniqueness concerns. Herein, IGDT was exercised mainly on the model parameters to study the effect of uncertainties. Future studies, however, can also extend IGDT to study the model form error that is the fundamental inability of the model to represent reality even at the best (but unknown) input parameter values. Model form error arises from the inexactness of

numerical models. Application of IGDT for model inexactness however necessitates parameterization of the model form (such as linear versus quadratic form to define the constitutive behavior). Furthermore, the IGDT can also be applied to study the inevitable scarcity of experimental data available for calibration and validation exercises.

The application of V&V and IGDT studies utilized herein were confined to the response of a single wind turbine blade, however, they naturally be extended to the components of the entire wind turbine system, including the simulation of the gearbox, wind turbine tower, and surrounding airflow. Focusing on the full integration of the coupled system in future work can be used to gain a more complete understanding of the behavior of wind turbines at the plant scale.

Furthermore, the simplified yet credible FE model developed herein can allow efficient coupling of structural dynamics with fluid dynamic models. V&V studies must be deployed on the coupled system considering the propagation of uncertainties and errors between the two coupled domains. V&V in the context of multi-scale and multi-physics models is an active research topic that warrants further work.